Stony Brook University

Crystallization and Structure Relationship of Polyolefin-based Polymers under Static and Flow Conditions

A Dissertation Presented

by

Xiaowei Li

to

The Graduate School

in Partial Fulfillment of the

Requirements

for the Degree of

Doctor of Philosophy

in

Chemistry

Stony Brook University

August 2013

Stony Brook University

The Graduate School

Xiaowei Li

We, the dissertation committee for the above candidate for the
Doctor of Philosophy degree, hereby recommend
acceptance of this dissertation.

Benjamin S. Hsiao – Dissertation Advisor
Professor, Department of Chemistry

Benjamin Chu – Dissertation Advisor
Distinguished Professor, Department of Chemistry

Robert B. Grubbs – Chairperson of Defense
Professor, Department of Chemistry

Stanislaus S. Wong—Third Committee Member of Defense
Professor, Chemistry Department

Andy H. Tsou—Outside Committee Member of Defense
Section Head, "Structure and Performance of Organic Materials", Chemical Sciences,
Corporate Strategic Research, ExxonMobil Research and Engineering Company, Clinton,
New Jersey.

This dissertation is accepted by the Graduate School

Charles Taber
Interim Dean of the Graduate School

Abstract of the Dissertation

Crystallization and Structure Relationship of Polyolefin-based Polymers under Static and

Flow Conditions

by

Xiaowei Li

Doctor of Philosophy

in

Chemistry

Stony Brook University

August 2013

Polyolefins have played an important role in human society, partially due to wide applications, such as their extensive use in packaging films, cables, wires, bags, containers, and appliances. Therefore, it becomes a worthwhile undertaking to investigate and to improve their properties, which can reduce cost and decrease pollution to the environment. Polyethylene (PE) and Polypropylene (PP) take a large role in polyolefin products. They occupy more than half of the thermoplastic market. They are semi-crystalline polymers with a relatively high degree of crystallinity. The crystal structure is an important factor that should be considered as they are closely related to the material performance. Both the characteritics of the starting material and the processing steps have significant effects on the crystal structure and subsquent materials properties.

In this thesis, the crystallization and structure relationship of polyethylene- and polypropylene-based materials, including pure polymer, blend and copolymer, were studied. *In-situ* Wide angle X-ray Diffraction (WAXD) and Small angle X-ray Scattering (SAXS) were performed during different processing steps, i.e., under static and flow conditions. A single cell heating stage was used for studying the static crystallization behavior of polyolefin-based materials under different thermal conditions. Isothermal crystallization of high-density polyethylene/silica (HDPE-SiO$_2$) at different SiO$_2$ loadings showed that SiO$_2$ behaved as crystal nucleus in the blend samples. Different instruments were used to study the structural changes during different processing steps. A specially designed cross-slot flow cell device was applied to generate extension-dominant flow and its influence on the crystallization behavior of isotactic polypropylene (iPP). A modified tensile stretching machine that allowed symmetrical stretching of the film was used to investigate the structural change during stretching and their relationship with mechanical performance. Ionic liquid (IL) and ultra-high molecular weight polyethylene (UHMWPE) blend prepared by solution mixing showed a significant increase in the elongation-to-break ratio. For propylene-1-octene random copolymers with higher octene content, the elastic modulus and the yield stress were decreased. Then, they behaved more like elastomers.

Table of Contents

List of Figures

List of Tables

Acknowledgments

First of all, I would like to express my heartfelt gratitude to my advisors Professor Benjamin S. Hsiao and Professor Benjamin Chu for their helpful advice, generous support and encouragement during my Ph.D studies. These research experiences are invaluable to me on both academic and personal levels, for which I am extremely grateful. I would also like to thank my committee members: Professor Robert B. Grubbs, Professor David M. Hanson and Professor Stanislaus S. Wong for their valuable comments and suggestions. Thank Dr. Andy H. Tsou from ExxonMobil Research and Engineering Company for representing as an outside member and also great help during my research work.

Thanks to Drs. Lixia Rong and Jie Zhu for their continuous help during my experiments at Brookhaven National Lab. Thank Drs. Christian Burger, Dufei Fang and Shigeyuki Toki in my research, and I have benefited a great deal from the discussions with them. I am thankful for former group members, Feng Zuo and Yimin Mao, who gave me great help during my Ph.D. years. I would like to thank all the members in Professors Chu and Hsiao's group. Many thanks to Hongyang Ma, Ran Wang, Liu Yang, Xiao Wang, Zhe Wang, Tsung-Ming Yeh, Justin Che, Rui Yang and Ying Su. We shared a wonderful time together. Thanks to Jane Wainio, Katherine M. Hughes and all other staffs from Chemistry Department for their help in my studies.

I would like to thank my parents, all other family members and friends for their understanding and support to finish my Ph.D. studies.

Chapter 1. Crystallization of Silica-Filled HDPE Nanocomposite

1.1 Introduction

Polymer-based nanocomposites have attracted wide attention in academic and industrial research in recent years. The usage of inorganic components to modify polymers can effectively influence organic polymers in different aspects, such as mechanical, thermal, electrical properties, et al. These properties can be finely tuned further by changing the component, composition and processing method of the nano additions [1-5]. Compared with traditional blend composites, the fillers in the nanocomposites have a much smaller length scale and a higher surface area to volume ratio. They can achieve enhanced effects with a smaller amount of material, provided that they can be dispersed uniformly. Besides, strong interactions between the nano filler and the polymer can produce new features that are not available in traditional composites.

High density polyethylene (HDPE) is one kind of important polymers in industry that has been used widely in different applications. However, relatively poor tensile toughness, impact strength, and processing ability limit its application. Imbedded inorganic particle fillers could significantly improve the mechanical properties of the composite [6, 7]. Silica is one kind of filler that is widely used in the polymer composite. The correlated research work of silica filled polyethylene has been previously reported in the literature [8-11].

Silica colloid is a random system that consists of a continuous solid network, forming a fractal structure, and the structure can be studied by using the small angle X-ray scattering technique [12-14]. The fractal structure can be recognized by a typical power-law decay region in a q range of $\xi \gg q^{-1} \gg a$, where ξ is the characteristic length of the fractal structure and a is the characteristic length of the primary particles [15]. Silica or carbon black in the nanocomposite has a self-similar network structure over a large length scale and can also be considered as a fractal network [16-19].

Silica particles have been used as fillers in rubber or plastic systems to enhance the mechanical properties. The structure of silica network in the composite and the interaction between filler-filler and between filler-polymer could be important to the macro-properties. However, due to the complexity of the system and the difficulty on the characterization of those micro structures, there remain many questions that need to be addressed, as the mechanism is not fully understood. In semi-crystalline composite systems, the crystallinity of polyolefins, such as that of polyethylene, is relatively high. Unlike non-crystalline systems, the fillers inside the polymer may adsorb the polymer molecules and act as crystal nuclei, which will have a greater influence on the kinetics of crystallization, the crystal structure, and the properties of the composite. The influence of fillers on the crystallization behavior of polyolefin has previously been reported in literature [20, 21], mainly by using the DSC (Differential Scanning Calorimetry) method.

In situ synchrotron X-ray scattering is a powerful tool used to study the evolution of crystal structure by wide angle diffraction and inhomogeneities on a macromolecular scale by small

angle scattering. However, the silica-filled HDPE system has been difficult to analyze in the small angle region because of the combination of signals from the crystals of polyethylene and the silica network structure.

In this chapter, we mainly use time-resolved wide angle X-ray diffraction (WAXD) and small angle X-ray scattering (SAXS) to study the structural changes of HDPE and the silica network under isothermal conditions. The silica filled HDPE nanocomposite was prepared by using the melting-blend method, where silica particles were pre-covered with a coupling agent used for dispersion of silica particles in the HDPE matrix without agglomeration. The goal is to investigate the role and the effect of silica network on the structure and morphology of high density polyethylene (HDPE) during isothermal crystallization.

1.2 Experiment

1.2.1 Materials

HDPE and silica-HDPE nanocomposite samples were obtained from ExxonMobil Chemical Company. Weight average molecular weight (M_w) and number average molecular weight (M_n) of HDPE was determined using the GPC method to be 1.22×10^5 g/mol and 1.54×10^4 g/mol, respectively, with a polydispersity of 7.92. Silica nano particles were purchased from Sigma-Aldrich with a particle size of 14 nm and surface area of 200 +/- 25 m^2/g. Before mixing, silica particles were coated with a thiol-silane coupling agent, 3-mercaptopropyltrimethoxysilane,

by the solution method. The silica-HDPE nanocomposite was then prepared by extruding mixing of the two components. A small amount of peroxide was added to start the thiol-ene reaction between the chain end vinyl group of HDPE and the thiol of the silane coupling agent during extrusion. Two different composition composites were prepared with varying silica weight percentage of 2% and 5%, respectively. These are denoted as HDPE-Si2% and HDPE-Si5%.

1.2.2 Measurements

Thermal properties of the samples were studied using a Perkin-Elmer DSC 7 differential scanning calorimeter (DSC) with a heating and cooling rate of 10 ℃/min under dried nitrogen gas atmosphere.

The nanocomposite morphology was examined by scanning electron microscopes (SEM) LEO Gemini 1550, which allowed for high resolution imaging of surfaces and cross-sections of solid materials. In addition, it was equipped with an EDS (energy dispersive X-ray spectroscopy) system using an EDAX detector that provided information on the elemental compositions at the detecting area. For composite samples, they were first fractured in liquid nitrogen and then sputter-coated with gold to avoid charging during observation.

1.2.3 *In-situ* X-ray scattering technique for the isothermal crystallization of silica-HDPE composite

In-situ wide-angle X-ray diffraction (WAXD) and small-angle X-ray scattering (SAXS) were used to characterize the isothermal crystallization behavior of HDPE and silica-HDPE

nanocomposites at the X27C Beamline, National Synchrotron Light Source (NSLS), Brookhaven National Laboratory (BNL). The wavelength of the synchrotron radiation was 1.371 Å. A charged coupled device (CCD, MAR-USA) detector was used to collect 2D scattering/diffraction patterns in real time. The CCD detector had a resolution of 1024×1024 pixels and each pixel size was 158.44 μm. The typical image acquisition time was 20 s for each data frame, with 13.3 s exposure time and 6.7 s data collecting time. The sample-to-detector distance was 1782 mm for the SAXS setup (calibrated with silver behenate) and 125.8 mm for the WAXD setup (calibrated with Al_2O_3). All X-ray images were corrected for background scattering, air scattering, and synchrotron beam fluctuations.

The isothermal crystallization experiment was performed in a single cell hot stage INSTEC HCS600V with a precision temperature controller STC200, which is equipped with the LN2-SYS liquid nitrogen cooling system. The hot stage had a temperature control of 0.1 ℃, with a heating and cooling rate of over 100 ℃/min. The sample was first melted at 170 ℃ for 5 minute to remove all residual stress and thermal history. The sample was then cooled to the desired crystallization temperature at an approximate rate of -100 ℃/min for isothermal crystallization. During the isothermal process, structural changes of the crystal and silica network were monitored *in situ* by time-resolved WAXD/SAXS as described above.

1.2.4 X-ray Data Analysis

The quantitative analysis of crystallinity dependence on the crystallization time was based on 2D WAXD patterns. The patterns were first corrected for background scattering, air scattering,

beam fluctuations, and Fraser correction (to compensate for the distortion from the flat-detector effect [22]). For isotropic WAXD patterns, 1D scattering profiles were obtained by integration along the scattering vector, expressed as $I(s) = 2\pi \int_{0^o}^{180^o} I(s,\phi)s^2 \sin \phi d\phi$, where the Lorentz correction was used to obtain the true mass distribution in the system. The areas of crystal peaks and of an amorphous background peak were then separated by using the curve fitting method. The crystallinity was obtained by dividing the sum of area of all crystalline peaks by the total area. Due to the missing information in the higher scattering angle region, the "crystallinity" obtained in this way should be called the "crystallinity index". This index value is less than the true crystallinity value, but such a calculation could still be useful to study the general trend of the crystallization process. It should be mentioned that in the early stage of crystallization, the crystallinity is relatively low and these data are crucial in determining the crystallization kinetic parameters by using the Avrami equation, which is shown in the Results and Discussion part below. According to previous study, the obtained crystallinity from the WAXD technique used here has a detecting limit as low as 1% [23], and this can provide good precision on the calculated results.

The 2D SAXS patterns were first corrected using the same method as the 2D WAXD patterns mentioned above. The 1D curve was then obtained by integration along the scattering vector direction as $I(s) = 2\pi \int_{0^o}^{180^o} I(s,\phi) \sin \phi d\phi$. The lamellar spacing was estimated by finding the position of the maximum scattering in the Lorentz-corrected SAXS profiles.

1.3. Results and Discussion

Before the isothermal crystallization experiment, the thermal properties were characterized by the DSC. The results are listed in Table 1.1. It was found that the addition of silica into HDPE decreased the melting temperature, probably caused by imperfections and less ordering of crystals in the silica-HDPE composite. On the other hand, the cold crystallization temperature was increased, indicating that silica particles might behave like a nucleus during undercooling, making the crystallization process to occur more easily.

Table 1.1 Thermal properties of HDPE and silica-HDPE composites from DSC measurements

Silica content (%)	T_m ℃	T_{cc} ℃
0%	138.8	113.1
2%	133.3	116.5
5%	132.9	116.5

T_m (Melting Temperature)　　**T_{cc} (Cold Crystallization Temperature)**

The isothermal crystallization of HDPE and that of silica-HDPE composite were performed at 120 ℃. The 1D WAXD curves of all the samples at the end of the crystallization process (400 s after reaching the experiment temperature) are shown in Figure 1.1. It is obvious that the polyethylene crystals in all three samples had the reflection peaks of (110), (200) and (210) located at the scattering vector s value of 2.42 nm^{-1}, 2.68 nm^{-1} and 3.36 nm^{-1}, respectively, in the

experimental scattering range. These are typical reflection peaks of an orthorhombic phase, and

the positions of these peaks are nearly the same in all the samples, suggesting that the crystal

lattice parameters are nearly unchanged with the addition of silica, and that the silica component

could reside beside the crystals of polyethylene. There was no indication of the appearance of

silica crystal reflection peaks, as nano silica particles will be in the noncrystalline state.
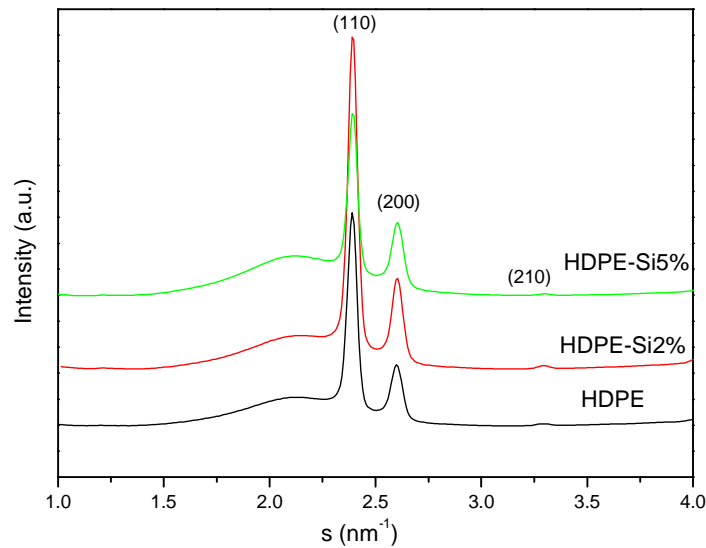
Figure 1.1 1D WAXD curves of HDPE and Silica-HDPE composite for isothermal
crystallization at 120 ºC for 400 s.

The evolution of crystallinity calculated from WAXD patterns during isothermal

crystallization is shown in Figure 1.2. Silica-HDPE composites showed higher final crystallinity

as the silica particles could act as nuclei. HDPE-Si5% had less crystallinity than HDPE-Si2%.

The possible reason for this observation will be discussed later. The crystallization kinetics of

polyethylene could be routinely studied by using the Avrami equation [24-26]:

$$X_c(t) = 1 - \exp(-Kt^n)$$
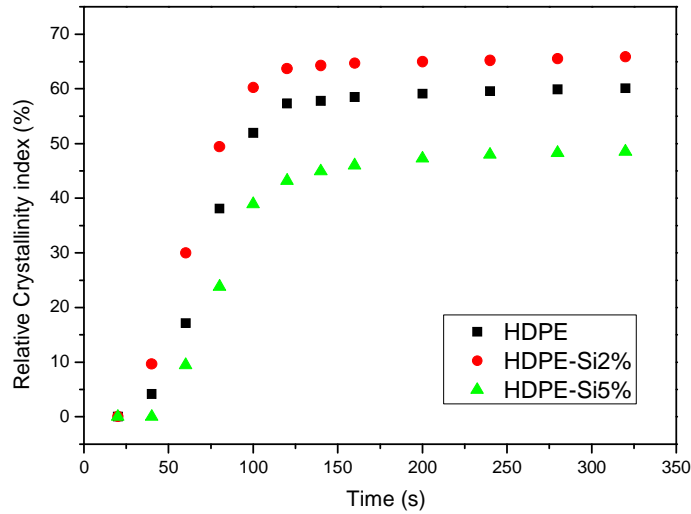
Figure 1.2 Evolution of crystallinity of HDPE and Silica-HDPE composite during isothermal crystallization at 120 ℃.

This function described the development of crystallinity as a function of time. Since the crystal volume fraction is usually less than 1 in a semi-crystal polymer system, X_c could be expressed as $v_c(t)/v_c(\infty)$, where $v_c(t)$ and $v_c(\infty)$ are volume fractions of the crystal at time t and at infinite time (∞). The crystallinity value could be obtained from the peak fitting of WAXD curves. K is the rate constant and n is the Avrami exponent that describes the mode of crystallization. The function could then be expressed as:

$$\lg\left[-\ln(1-\frac{v_c(t)}{v_c(\infty)})\right] = \lg K + n\lg t$$

The Avrami exponent is the slope of the straight line by plotting $\lg\left[-\ln(1-\frac{v_c(t)}{v_c(\infty)})\right]$ versus lg(t). Avrami plots of HDPE and silica-HDPE are shown in Figure 1.3. For semicrystalline polymers, like polyethylene, Avrami plots show linearity usually only in the initial stage,

followed by a deviation from linearity. The most probable reason for this is the occurrence of secondary crystallization [27-30]. Here, the two-stage crystallization phenomenon is also observed. From the linear part in the primary crystallization, the Avrami exponent of HDPE and HDPE-Si2% was calculated as 3.7 and 3.1, respectively. For pure HDPE, the Avrami exponent was close to 4, indicating a homogeneous nucleation mechanism during the isothermal crystallization. While the value was close to 3 in HDPE-Si2%, this observation was consistent with the heterogeneous nucleation process. The literature result also showed that silica nano particles could act as nucleating agents [20, 21]. For HDPE-Si5%, the curve had fewer points in the initial stage. It was reported that the X-ray determination of crystallinity had a lower accuracy for short crystallization times [31]. The primary crystallization step was too fast in HDPE-Si5% due to the high silica content, and it became difficult to study the crystallization process. Therefore, the Avrami exponent was not calculated here. The Avrami exponent and also the half-time of crystallization is summarized in Table 1.2.
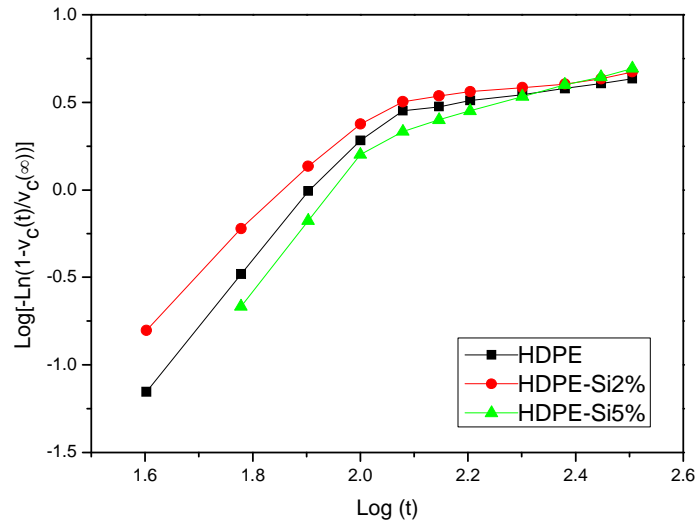
Figure 1.3 Plots of $\lg\left[-\ln(1-v_c(t)/v_c(\infty))\right]$ versus lg(t) for crystallization of HDPE and Silica-HDPE composite.

Table 1.2 Crystallization kinetic parameters of HDPE and silica-HDPE composites

Silica content (%)	Half-time of crystallization	Avrami exponent
	$t_{1/2}$ (s)	n
0%	74	3.7
2%	65	3.1
5%	83	--

Scanning electron microscope (SEM) images of the fracture surface of silica-HDPE can provide information about the silica morphology in the composite. No special structure was found in pure HDPE (not shown here). For HDPE-Si2% and HDPE-Si5%, the branched network

morphology of silica is shown in Figure 1.4. Though these SEM images were taken under room temperature, the morphology in the picture should be a good evidence for the branched network structure of silica in the nanocomposite. In the magnified picture, the length scale of the branch diameter was estimated as tens of nanometers, in agreement with the original primary particle size value.
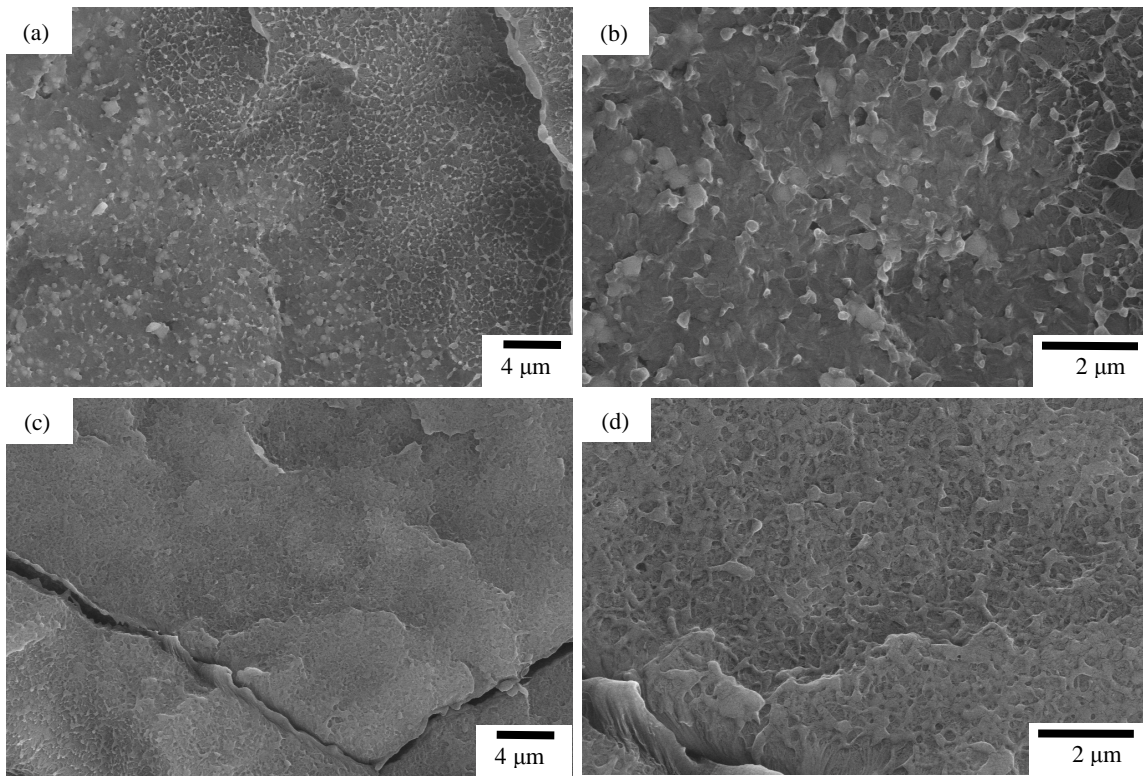
Figure 1.4 SEM images of Silica-HDPE nanocomposites: (a) HDPE-Si2% at 10K magnification, (b) HDPE-Si2% at 30K magnification, (c) HDPE-Si5% at 10K magnification, (d) HDPE-Si5% at 30K magnification.

It is well known that in the filled polymer system, an increase in the filler concentration can make the filler form a connected network structure. Jouault et al. [32] studied the dispersion of silica in polystyrene matrix. In their study, they found that with a small silica volume fraction, silica particles could gather into "primary aggregates" as finite size fractal clusters dispersed in

the matrix, and with an increase in the silica content, these primary aggregates would connect with each other to form a continuous network. In the case here, it was difficult to conclude if the silica particles would form a continuous network in the HDPE and how the silica structure changed with increasing of silica loading. But, at least it was reasonable to assume that the silica particles aggregated together and formed a similar branched network structure.

Wide angle X-ray diffraction can provide the crystal information of polyethylene. However, there was no direct silica signal in the diffraction curve. The length scale of the silica structure was larger than that of HDPE crystal. Small angle X-ray scattering is a powerful tool that can be used. SAXS curves of semi-crystal polymers have been extensively studied in the literature and the size of lamella crystal layer can be estimated from the curve. In the composite material, the scattering intensity comes from the sum of the signals for different components, or some new structure from the interaction between two components. In these situations, the analysis is difficult as it is necessary to separate the signals from the different components. To further understand the influence of silica on the HDPE lamella crystal structure during isothermal crystallization, 1D integrated SAXS curves were obtained. The results are shown in Figure 1.5, with the curves being plotted with an offset for easier viewing. For simplicity, only HDPE-Si2% curves are shown for comparison. For the initial SAXS curves in these samples, which were the first frame taken after the samples reached 120 ℃, the scattering intensity came from the sum of silica structure and amorphous polyethylene, since no crystals were formed at that time according to the WAXD patterns. It was found that the experimental curve of neat HDPE had much less scattering intensity when compared with the silica-HDPE composite. Therefore, the

13

scattering intensity of polymer was very small, and the major signal was from silica network structure in the nanocomposites. The scattering invariant Q was calculated from the SAXS curve and their dependence on time is plotted in Figure 1.6. The scattering invariant is obtained using the follow expression [33]:

$$Q = \int_0^\infty I(s)s^2 ds$$

Due to the detecting range of SAXS, the integration of s is limited. The invariant Q is proportional to the mean square density fluctuations in the system, reflecting all the inhomogenities in the system within the detecting range. Hence, the value includes both the signal from HDPE (mainly from the lamella crystal structure) and the silica network. It was found that most of the scattering intensity was contributed from the silica network structure in the silica-HDPE composite. As the crystallization began, the Q value increased rapidly in the initial stage due to the formation of crystals. After 100 s, it slightly increased and reached to a plateau. The evolution trend was similar to the increase in crystallinity as shown in Figure 1.2. This trend indicated that the increase of Q in the initial stage was mainly caused by the crystallization of HDPE. Though not quantitatively, it could be found that the main trend of the silica-HDPE scattering curves did not change, except for the occurrence of the lamella scattering shoulder. It should be noted that if the silica branched network collapsed and the silica particles aggregated in a large quantity, the scattering intensity should decrease. However, this was not the case here. It would be reasonable to presume that the silica network remained the same during the crystallization process, or at least most of the silica kept their structures, and only a small portion of silica might collapse.
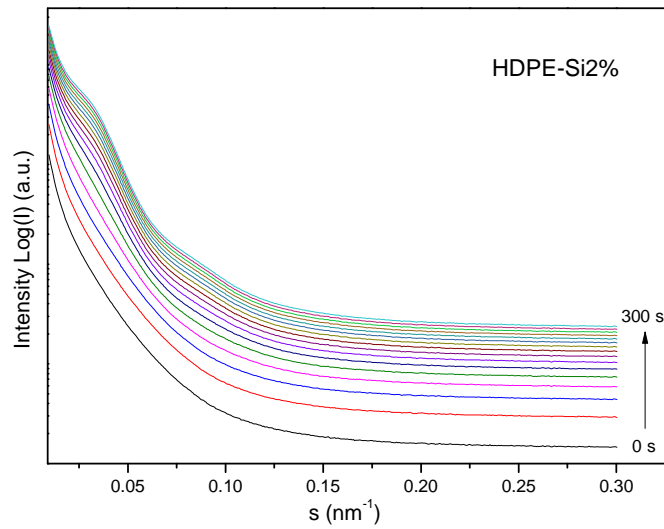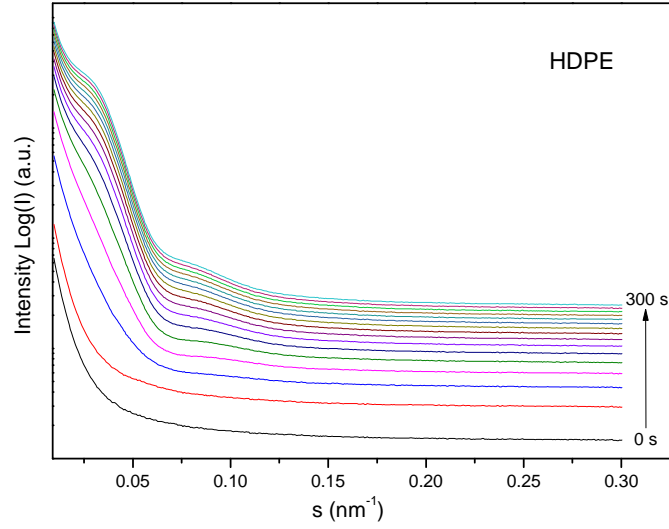
Figure 1.5 Evolution of SAXS curves of HDPE and HDPE-Si2% during isothermal crystallization under 120 ºC.
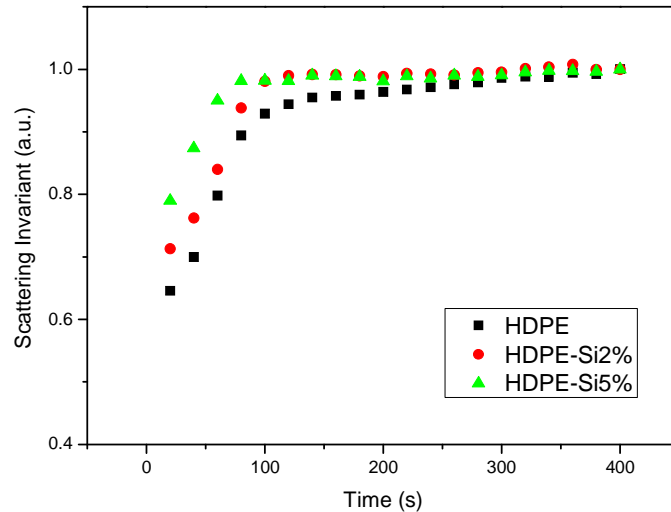
Figure 1.6 Evolution of scattering invariant for HDPE and silica-HDPE composite during isothermal crystallization at 120 ºC.

In all three samples, the lamella scattering peaks were observed in the SAXS curves during crystallization. However, the change in the curves and also the appearance of the lamella scattering peaks was more obvious in the pure HDPE sample. In the silica-HDPE sample, only small shoulders were observed during the isothermal crystallization process. Figure 1.7 (A) shows the SAXS curves of three samples at 400 s, where the samples had the highest degree of crystallinity at that time. With the addition of silica, the HDPE lamella peak became broader and the peak position was more difficult to locate. This was caused by the overlap of silica scattering signals. The scattering peak position was estimated by plotting Is^2 versus s, and the long period of the lamellar structure was obtained by the inverse of the peak position. The long period distance was almost the same in all three curves with a value of 31.2 nm. As it was presumed that the silica network would not change during the isothermal crystallization process, the silica

scattering signal was separated from all the scattering curves by subtracting it with the first initial scattering curve at the beginning of crystallization. The obtained curves are shown in Figure 1.7 (B). A clearer view of the lamella scattering peaks was acquired in the silica-HDPE composite, and the scattering curves were quite similar to the pure HDPE sample, suggesting that the addition of the silica nanoparticles did not significantly change the lamella structure of polyethylene, or at least in the observed length scale.

Based on all of the results above, it was possible to propose a model for the crystallization process of silica-HDPE nano-composites. At high temperatures, polyethylene was in the melt state and the polymer chains were randomly distributed in the system. The silica particles also formed a random branched network structure. The two components were mixed with each other. When the system was in the undercooling condition, the silica particles could behave as nucleus centers for the crystallization of HDPE. The crystals formed around the silica branch and the silica network would mostly remain during the process. Considering that there was no significant crystal lattice deviation with the addition of silica, the branched silica particle aggregates could only exist in the amorphous region of the polyethylene, and the lamella crystals formed in the "holes" of the branched network. The effect of nucleus would help polyethylene to crystallize. However, the existence of the silica network would decrease the freedom of crystal growth. When the silica content was relatively high, the branched network became more condensed, and there would be less space for the growth of crystals even with the higher nucleus content. So HDPE-Si5% had a slower crystallization rate and a smaller final amount of crystallinity than HDPE-Si2%. Figure 1.8 shows the schematic diagram for this process.
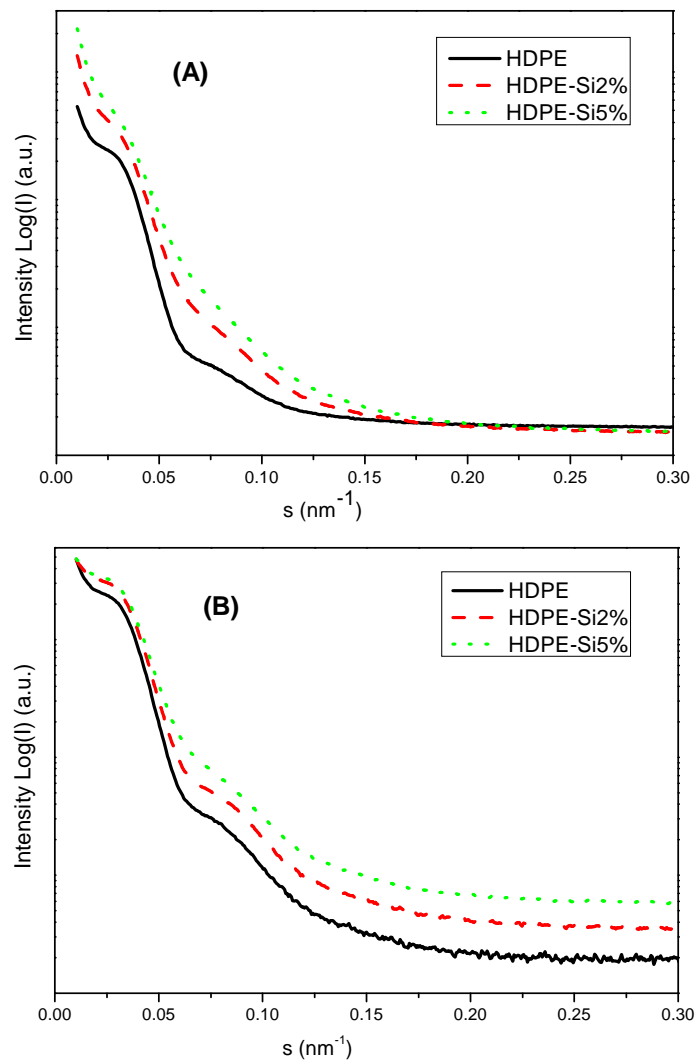
Figure 1.7 SAXS curves of HDPE and silica-HDPE composite at (A) 400 s of isothermal crystallization under 120 ℃ (B) at 400 s after subtracting the silica scattering signal.
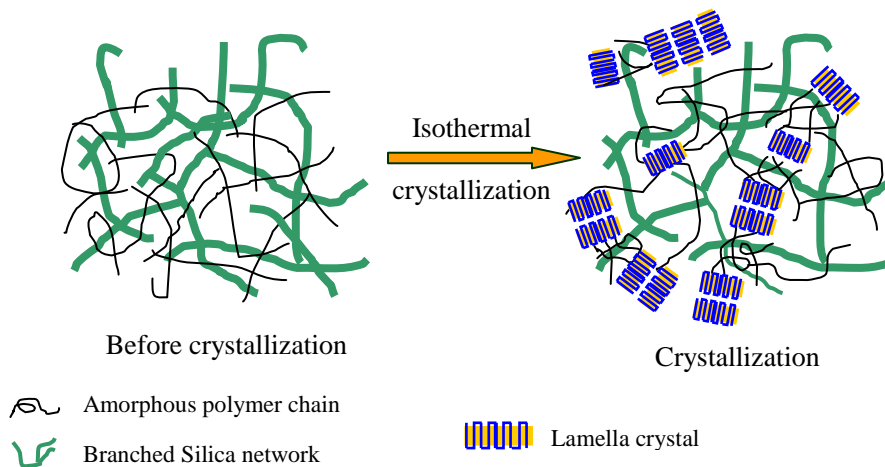
Figure 1.8 Schematic model for crystallization of silica-HDPE nano-composite (for illustration of crystallization only, the sketch may not reflect the true length scale relationship of these structures).

1.4 Conclusions

Silica-HDPE nano composite showed a different crystallization mechanism from that of pure HDPE. The silica particles inside the HDPE acted as nucleus centers for the crystallization of the polymer component. HDPE-Si2% had the highest crystallization rate and the highest crystallinity, while the higher silica content (HDPE-Si5%) did not favor the crystallization.

The silica inside the nano-composite had a branched network structure. During the isothermal crystallization process, the silica network structure was almost unchanged and resided inside the amorphous region of polyethylene. The silica particles could act as nucleus centers to favor crystallization, while the silica network would also impede the growth of crystals. This might be the reason for the lower crystallinity of HDPE-Si5%.

References

1. Balazs AC, Emrick T, and Russell TP. Science 2006;314(5802):1107-1110.

2. Schaefer DW and Justice RS. Macromolecules 2007;40(24):8501-8517.

3. Vaia RA, Jandt KD, Kramer EJ, and Giannelis EP. Macromolecules 1995;28(24):8080-8085.

4. Vaia RA and Giannelis EP. MRS Bull. 2001(26):394-401.

5. Schadler LS. Nanocomposite Science and Technology; Wiley-VCH: Weinheim, Germany, 2003.

6. Thongruang W, Balik CM, and Spontak RJ. Journal of Polymer Science Part B: Polymer Physics 2002;40(10):1013-1025.

7. Liu ZH, Kwok KW, Li RKY, and Choy CL. Polymer 2002;43(8):2501-2506.

8. Wang KH, Chung IJ, Jang MC, Keum JK, and Song HH. Macromolecules 2002;35(14):5529-5535.

9. Zhang MQ, Rong MZ, Zhang HB, and Friedrich K. Polymer Engineering & Science 2003;43(2):490-500.

10. Makarov C, Khalfin RL, Makarov V, Cohen Y, Sertchook H, Elimelech H, and Avnir D. Polymers for Advanced Technologies 2007;18(9):712-719.

11. Zou H, Wu S, and Shen J. Chemical Reviews 2008;108(9):3893-3957.

12. Schaefer DW and Keefer KD. Physical Review Letters 1986;56(20):2199-2202.

13. Vacher R, Woignier T, Pelous J, and Courtens E. Physical Review B 1988;37(11):6500-6503.

14. Schaefer DW, Rieker T, Agamalian M, Lin JS, Fischer D, Sukumaran S, Chen C, Beaucage G, Herd C, and Ivie J. Journal of Applied Crystallography 2000;33(3 Part 1):587-591.

15. Donatti DA, Vollet DR, Ibanez Ruiz A, Mesquita A, and Silva TFP. Physical Review B 2005;71(1):014203.

16. Mélé P, Marceau S, Brown D, de Puydt Y, and Albérola ND. Polymer 2002;43(20):5577-5586.

17. Meier JG, Mani JW, and Klüppel M. Physical Review B 2007;75(5):054202.

18. Schneider GJ, Vollnhals V, Brandt K, Roth SV, and Goritz D. Journal of Chemical Physics 2010;133(9).

19. Matějka L, Pleštil J, and Dušek K. Journal of Non-Crystalline Solids 1998;226(1–2):114-121.

20. Jiasheng Q and Pingsheng H. Journal of Materials Science 2003;38(11):2299-2304.

21. Jain S, Goossens H, van Duin M, and Lemstra P. Polymer 2005;46(20):8805-8818.

22. Fraser RDB, Macrae TP, Miller A, and Rowlands RJ. Journal of Applied Crystallography 1976(9):81-94.

23. Wang ZG, Hsiao BS, Sirota EB, Agarwal P, and Srinivas S. Macromolecules 2000;33(3):978-989.

24. Avrami M. J. Chem. Phys. 1939(7):1103.

25. Mandelkern L. Crystallization of polymers McGraw-Hill, New York, 1963.

26. Gedde UW. Polymer Physics, Chapman & Hall, New York, 1995

27. Velisaris CN and Seferis JC. Polymer Engineering & Science 1986;26(22):1574-1581.

28. Hwang JC, Chen C-C, Chen H-L, and Yang W-CO. Polymer 1997;38(16):4097-4101.

29. Mandelkern L. Crystallization of Polymers: Kinetics and mechanisms, Cambridge University Press, 2004.

30. Gordon M and Hillier IH. Phil. Mag. 1965;11(109):31-41.

31. Wenig W. Journal of Materials Science 1994;29(18):4708-4712.

32. Jouault N, Vallat P, Dalmas F, Said Sr, Jestin J, and Boué Fo. Macromolecules 2009;42(6):2031-2040.

33. Glatter O and Kratky O. Small Angle X-Ray Scattering; Academic Press: New York, 1982.

Chapter 2 . Uniaxial Stretching of Silica-Filled HDPE Nanocomposites

2.1 Introduction

The use of fillers in polymeric systems has become a common method in industry to improve their properties or simply to reduce the cost. In recent years, polymer nanocomposites have attracted a great deal of attention in both academic and industrial research fields. In these new nanocomposites, the fillers inside usually have a much smaller length scale and higher surface area to volume ratio, with at least one dimension of the filler in the nanometer range. According to the dimensions, the nano filler can be specified as nanoparticles, nanotubes or nanosheets. Due to their high surface area to volume ratio, the filler inside the polymer can have strong interactions with the polymer matrix and significantly influence the chemical and physical properties of the composites. The reduction of the filler size down to nanometric scale can produce substantial enhancements in various properties with much less amount of materials [1-8].

As stated in Chapter 1, silica particles can be used as fillers in polymers, such as polyethylene and polypropylene, to improve the tensile toughness, impact strength and processing ability [7-12]. While the increased performance is observed, the true mechanism and

the silica structure inside the polymer matrix, under different external forces, are still unclear. In this study, uniaxial stretching was carried out on HDPE and silica-HDPE nanocomposites to investigate the effects of filled silica on the tensile performance. During stretching, *in-situ* wide-angle X-ray diffraction (WAXD) and small-angle X-ray scattering (SAXS) were applied to monitor the structural changes of the lamellar crystal and silica network in the composite under deformation. Scanning electron micrographs (SEM) was used to obtain the morphology information of the stretched HDPE and silica-HDPE. In this work, we aimed to study the influence of silica particles on the crystal structure of HDPE, the formation of the silica structure during stretching and its effect on the mechanical properties of nanocomposites.

2.2 Experiment

2.2.1 Materials

HDPE and silica-HDPE nanocomposite samples were obtained from ExxonMobil Chemical Company. Two composites HDPE-Si2% and HDPE-Si5% were prepared along with the control sample HDPE. The detailed information could be found in Chapter 1.

2.2.2 Measurements

TGA thermograms of HDPE and silica-HDPE were collected at a heating rate of 20 °C/min using a TGA 7 (Perkin-Elmer Inc.).

The tensile properties of HDPE and its composites were studied using a modified Instron 4442 tensile apparatus. All the samples were first melt-pressed into a flat sheet at 170 ℃ with a thickness of 0.8 mm. The samples were then cut into dumbbell shapes for testing, with a length of 30 mm between the Instron clamps and a width of 4 mm. A constant deformation rate of 3 mm/min was applied to the specimen throughout the deformation study under room temperature. The stress and strain reported in this study were engineering stress and engineering strain measured directly from the Instron apparatus.

The nanocomposite morphology was examined by using a scanning electron microscope (SEM) LEO Gemini 1550, which allowed for high resolution imaging of the surfaces and cross-sections of solid materials. The detailed information could be found in Chapter 1.

In-situ wide-angle X-ray diffraction (WAXD) and small-angle X-ray scattering (SAXS) were used to characterize the structural changes of HDPE and silica-HDPE nanocomposite during stretching at the X27C Beamline, National Synchrotron Light Source (NSLS), Brookhaven National Laboratory (BNL). The beamline setup and image collection condition were similar to those stated in Chapter 1. All X-ray images were corrected for background scattering, air scattering, and synchrotron beam fluctuations.

Melt rheological measurements were performed by an Anton-Paar stress rheometer MCR 301-Physica under nitrogen atmosphere. Before testing, polymers samples were premolded into disk-shapes with a suitable thickness at 180 ℃. Oscillatory shear measurements (frequency sweep testes) were performed using a parallel plate with diameter of 25 mm and gap of 1 mm

under 180 ˚C. The chosen frequency range was 0.05 – 628 rad/s. Constant strain amplitude (γ = 1%) was applied in all measurements, within the linear viscoelastic limit.

2.3 Results and Discussion

Before the stretching experiment, TGA was employed to evaluate the thermal stability of HDPE and silica-HDPE nanocomposites. Figure 2.1 shows thermograms of these samples. From the weight loss profiles, the filled silica improved the thermal stability of HDPE in the nanocomposites. The degradation temperature of neat HDPE for 10.0 wt % weight loss was 368 ˚C. With increasing silica loading, the degradation temperature was increased, and for HDPE-Si5%, it was 396 ˚C for 10.0 wt % weight loss. Generally, the incorporation of silica into the polymer matrix will enhance thermal stability. The incorporated silica may form a network structure and act as a heat barrier during decomposition.
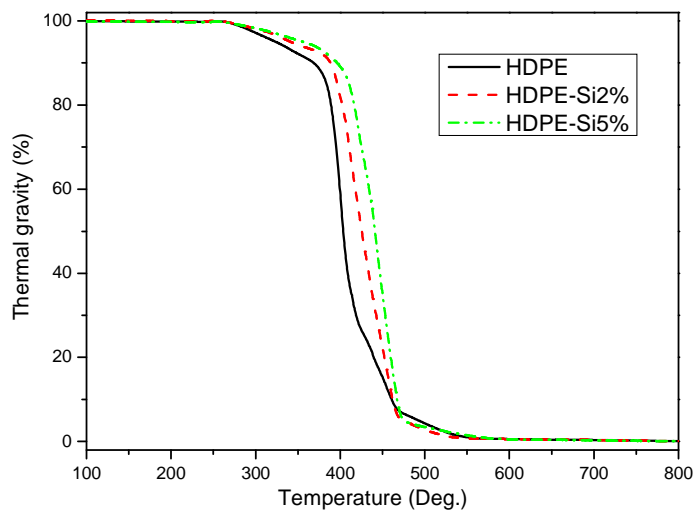
Figure 2.1 TGA thermograms of HDPE, HDPE-Si2%, and HDPE-Si5%.

Simultaneous X-ray and tensile deformation measurements were carried out at 25 ˚C. The stress-strain curves for all three samples are shown in Figure 2.2. All the profiles show typical tensile behavior of polymers. The yielding point was clearly observed in all samples at a strain of about 10%. With the filled silica, the yield strength increased from 24.0 MPa for neat HDPE to 26.4 MPa for HDPE-Si2% and 25.8 MPa for HDPE-Si5%. A higher silica loading did not show a further increase in the tensile performance. The evolution of the WAXD patterns for neat HDPE and silica-HDPE composite did not show significant difference. For simplicity, Figure 2.3 shows selected WAXD patterns of HDPE and HDPE-Si5% at strains 10%, 30% and 100%.. From these profiles, the addition of silica into the HDPE did not have an important influence on the crystal structure during stretching. Under current conditions, two strong reflection peaks were observed in these patterns. They could be ascribed to the (110) and (200) diffraction peaks of orthorhombic crystal phase of polyethylene. It is known that the monoclinic phase of polyethylene may appear under deformation [13-15]. While under the current experimental conditions, no new diffraction peaks were found or were too small to be detected in WAXD. The phase transformation was not considered in this study. At strain of 10%, the orientation of these diffraction peaks was still very weak. While at strain of 30%, (110) and (200) gradually moved to the equatorial direction and became a two-point pattern at strain of 100%, indicating that the crystals had a relatively high orientation. The crystallinity of polyethylene during stretching was calculated. Integrated 1D WAXD curves were separated into different crystal peaks and an amorphous background. The crystallinity of polyethylene was obtained from the ratio of the sum of the integrated area of all crystal diffraction peaks to the total integrated area. The evolution of

the calculated crystallinity of HDPE, HDPE-Si2% and HDPE-Si5% at various strains are shown in Figure 2.4. Initially, the crystallinity of HDPE (51.2%) and of HDPE-Si2% (50.4%) were slightly higher than that of HDPE-Si5% (47.8%). The addition of silica in the polyethylene decreased the ordering of polymer chains during crystallization. With increasing strains, the crystallinity of all three samples was gradually decreased. This indicated the destruction of the original crystals caused by the stretching force. At strains of about 40% to 60%, a decrease of crystallinity reached a plateau value in all three samples, which did not change significantly upon further stretching.
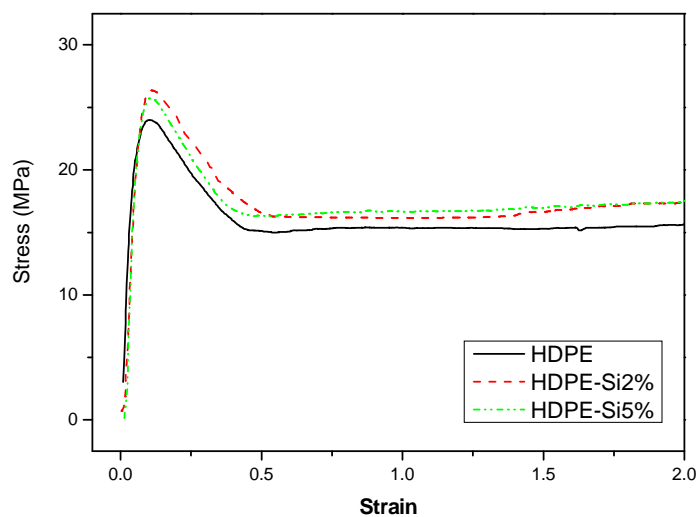
Figure 2.2 Stress-strain curves of HDPE, HDPE-Si2% and HDPE-Si5% at 25 ˚C**.**
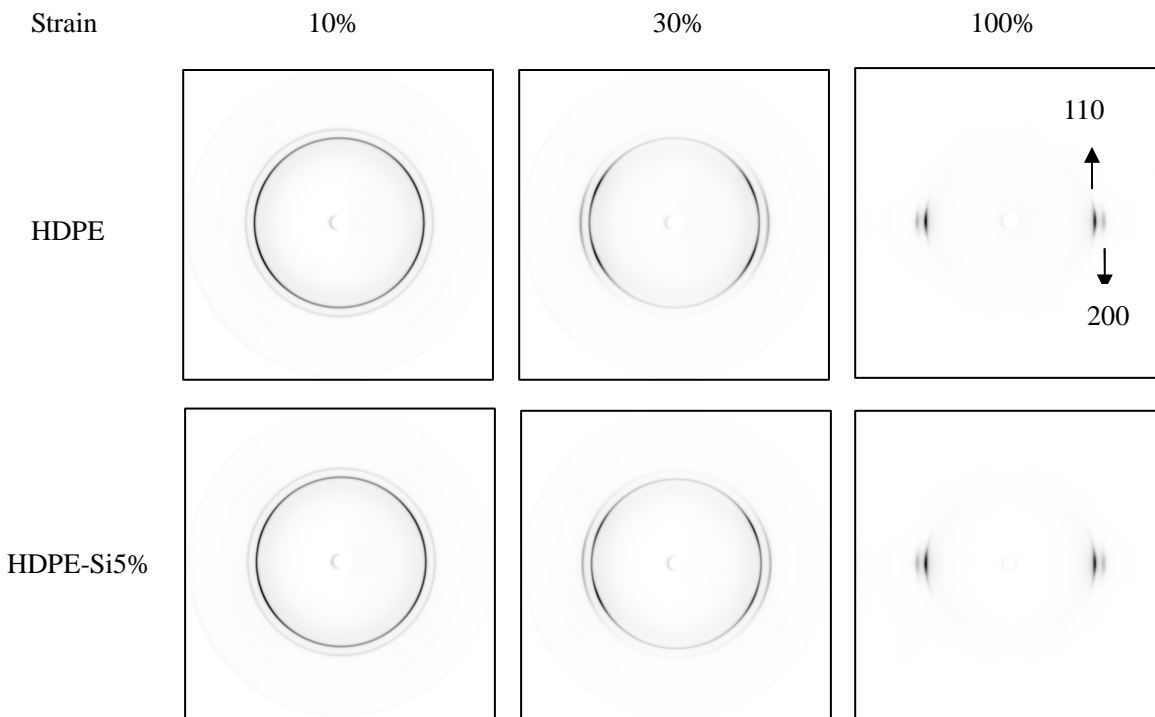
Figure 2.3 Selected WAXD patterns of HDPE and HDPE-Si5% at strains of 10%, 30% and 100%.
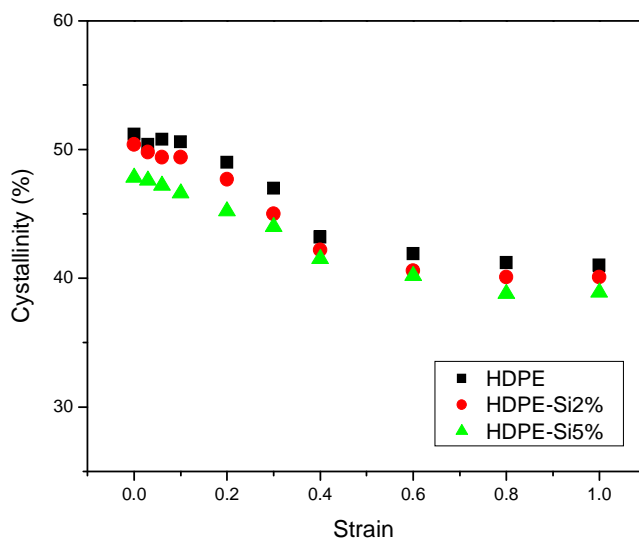
Figure 2.4 Evolution of crystallinity of HDPE, HDPE-Si2% and HDPE-Si5% during stretching at 25 ˚C.
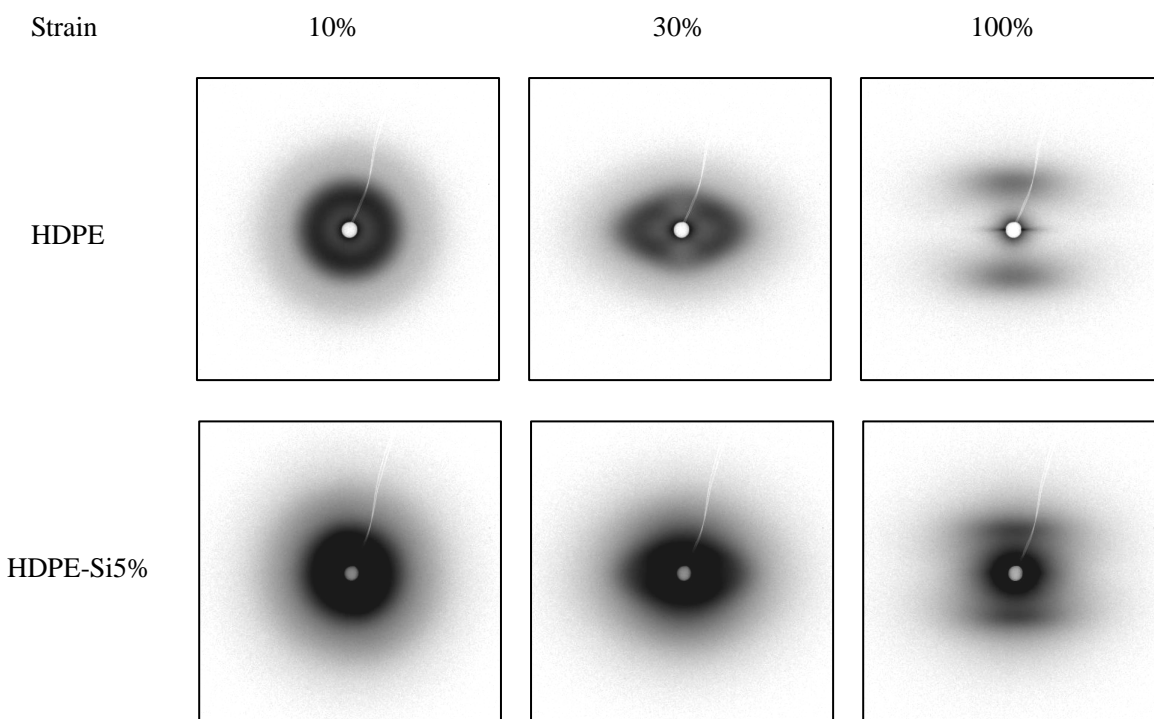
Figure 2.5 Selected SAXS patterns of HDPE and HDPE-Si5% at strains of 10%, 30% and 100%.

Different from WAXD patterns, SAXS of these samples showed quite different scattering patterns between the neat HDPE and silica-filled HDPE. Selected SAXS patterns for HDPE and HDPE-Si5% at strains of 10%, 30% and 100% are shown in Figure 2.5. At low strain of 10%, the SAXS profiles showed high isotropic scattering patterns. When the strain reached to 30%, the SAXS results showed off-axis four-point patterns. This was clearly present in neat HDPE, which indicated the tilting of lamellar crystals under deformation. At high strain of 100%, the HDPE sample showed a two-point pattern in the meridian direction, suggesting that lamella crystals had high orientation and aligned perpendicular to the machine direction, while for HDPE-Si5%, besides the lamellar scattering streak, a strong scattering signal appeared in the lower scattering angle region. This signal is isotropic and is related to the silica in the composite. Figure 2.6

shows the integrated SAXS intensity profiles. For neat HDPE, the lamellar scattering maximum was clearly observed at low strains. The scattering peak gradually decreased with increasing strain and then became almost constant at higher strains. The decrease in intensity was due to the destruction of the original crystals, which were identified in the WAXD results. The SAXS profiles of HDPE-Si2% and HDPE-Si5% were quite different. The lamellar scattering peak also decreased with increasing strain, while the intensity was very weak when compared with that of neat HDPE. There were large scattering signals in the low scattering angle region, probably caused by the silica network in the nanocomposite. The strong scattering intensity of the silica network would lead to difficulty in detecting the lamellar peak. Another interpretation could be that lamellar crystals had a less ordered structure caused by the addition of silica, resulting in weaker and broader scattering peak.   In order to obtain more quantitative information on the structural change during stretching, the scattering invariant Q at various strains was calculated from the SAXS curves. Figure 2.7 shows the strain dependence of invariants. The scattering invariant was obtained by using the follow expression [4]

$$Q = \int_0^\infty I(s)s^2 ds$$

As has been stated in Chapter 1, the invariant Q was proportional to the mean square density fluctuations in the system. It should reflect the scattering signals from both lamellar crystals and silica network. It should be noted from the Conclusion in Chapter 1, that most of the scattering intensity came from the silica network in the nanocomposite. Therefore, the invariant of the silica-HDPE should generally be larger than that of the neat HDPE and should increase with increasinge silica loading. However, there was a significant drop in all three samples on the

invariant with further increase in the strain and the invariant finally reached a plateau. Considering the position of the drop and its relationship with the WAXD results in Figure 2.4, the invariant drop could be caused by the destruction of lamellar crystals. It is interesting to note that the invariant was kept almost as a constant before and after the drop, suggesting that the stretching force could have little effect on the silica network structure, which was probably the reason for the improved tensile performance in the silica-HDPE nanocomposites.
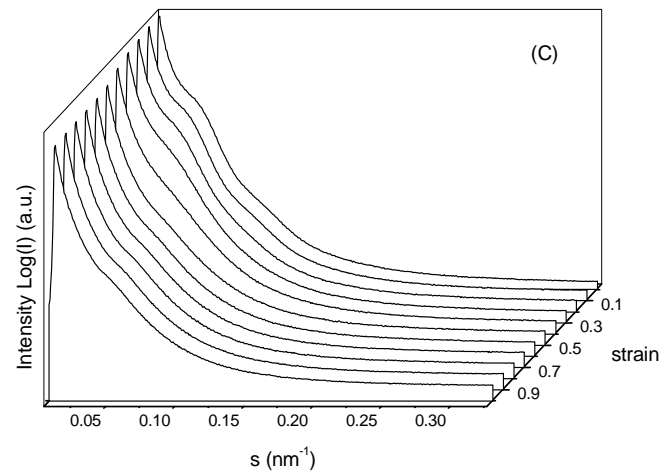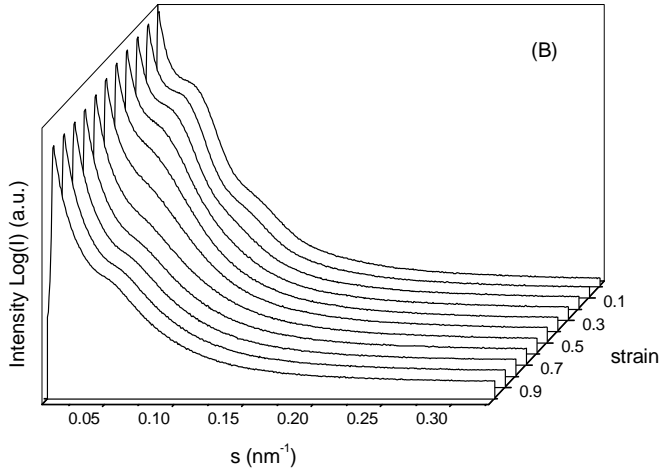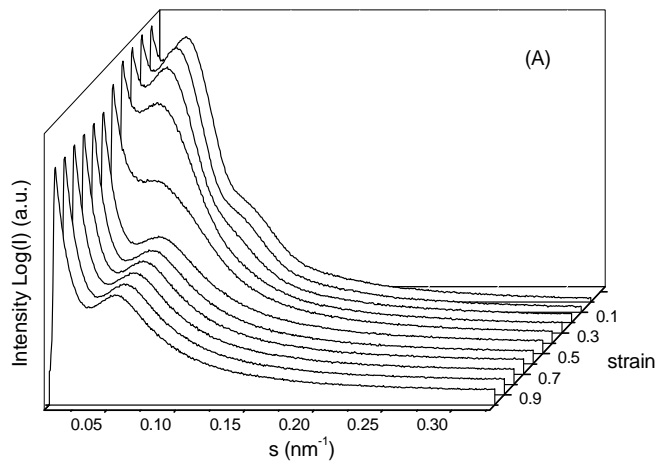
Figure 2.6 Evolution of SAXS intensity profiles during stretching: (A) HDPE, (B) HDPE-Si2%, (C) HDPE-Si5%.
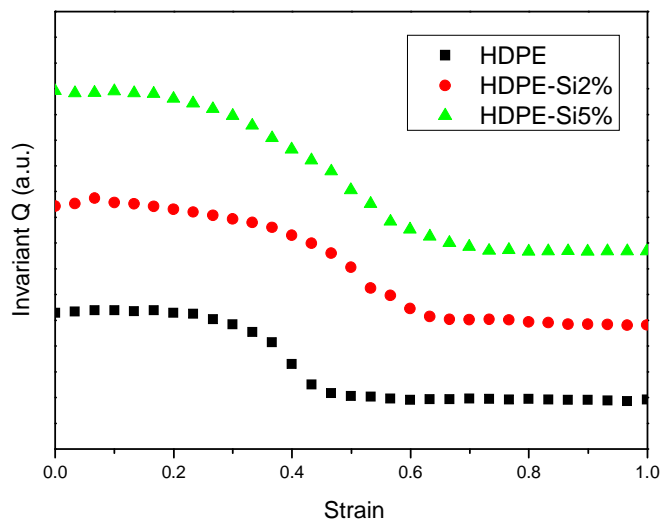
Figure 2.7 Invariants of HDPE, HDPE-Si2% and HDPE-Si5% at different strains.

Scanning electron micrographs (SEM) of the tensile deformed HDPE and its silica composites (at strain of 400%) parallel to the tensile direction are shown in Figure 2.8. From Figure 2.8 (a), on the surface of stretched neat HDPE, there were many large elongated cavities along the stretching direction. While in the silica-filled HDPE, as shown in Figure 2.8 (b) and 2.8 (c), the number and size of cavities under the same strain became smaller. The results suggested that the silica network structure could still exist under deformation. The silica and polymer matrix had good interfacial adhesion, resulting in tougher performance of nanocomposite in the tensile test.
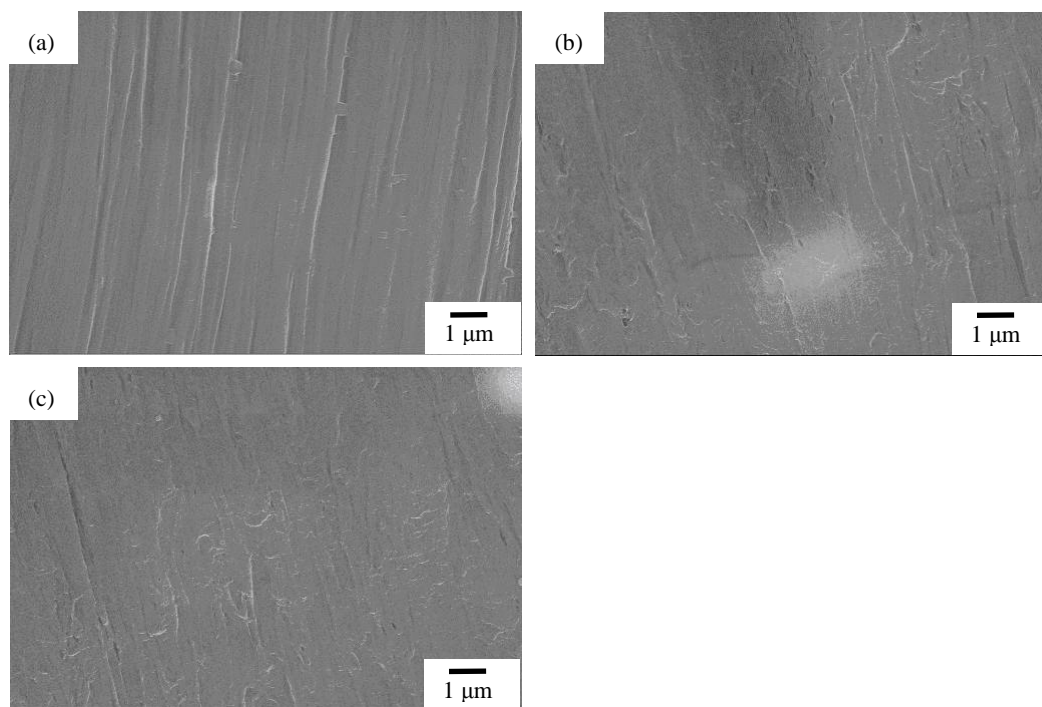
Figure 2.8 Scanning electron micrographs of tensile deformed composites parallel to the tensile direction: (a) HDPE, (b) HDPE-Si2%, (c) HDPE-Si5%.

In the nanocomposite, the incorporation of filler particles can produce substantial differences in the rheological behavior. Dynamic frequency sweep testes were performed on HDPE and silica-HDPE composite at 180 ℃. Figure 2.9 shows the frequency dependence of shear storage modulus (G') of three samples. For neat HDPE, typical rheological behavior was observed. For the silica-filled nanocomposite, the storage modulus showed similar trends in the high frequency region. However, in the low frequency region, the storage modulus increased in the silica-filled composite. Similar results were also observed and reported in other filled polymer nanocomposite systems [16-20]. In filled nanocomposite, the storage modulus tended to become frequency independent and a low-frequency plateau or pseudo-plateau could be present under certain condition. This kind of solid-like behavior could be attributed to the strong

interactions between nanoparticles and the polymer matrix [3, 21, 22]. In the current system, the

storage modulus of silica-HDPE composites showed less dependence at lower frequency, while

higher silica loading did not increase the G' any further. In the composite, the primary silica

particles interacted to form aggregates which together with the polymer matrix to form a network

structure. Silica-silica particle interactions inside the network and silica-polymer interactions in

the system should play an important role in improving the mechanical properties of the

nanocomposite.
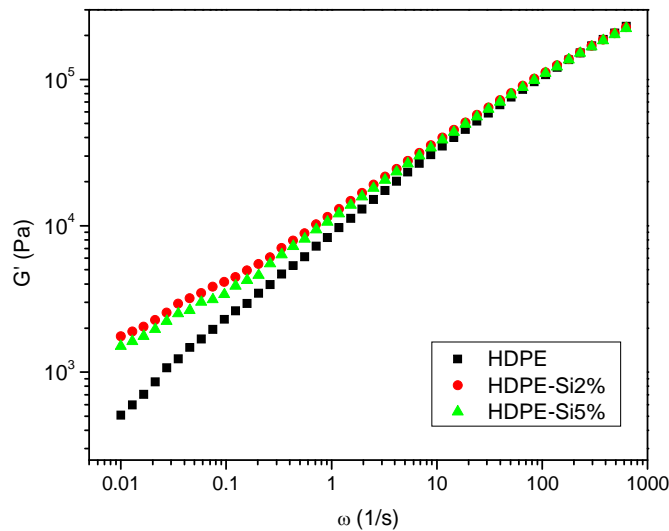
Figure 2.9 Storage modulus (G') curves of HDPE, HDPE-Si2% and HDPE-Si5% (T = 180 ˚C).

2.4 Conclusions

Tensile experiments showed that the addition of silica filler in the high density polyethylene

enhanced the tensile performance. During stretching, *in-situ* WAXD patterns did not show

significant different features in the silica-HDPE nanocomposite, while from SAXS results, silica-filled HDPE had a much stronger scattering intensity when compared with neat HDPE. Based on the calculation of invariant values from integrated SAXS curves, the scattering signals could be contributed mainly from the silica entities. In the silica-HDPE nanocomposite, the silica primary particles aggregated together and formed a network structure. This structure seemed to be unchanged with increasing strain. TEM images revealed that in the stretched surface, silica-HDPE samples had fewer amounts and smaller sizes of elongated cavities. The storage modulus of silica-HDPE samples also showed a less dependence on frequency in the low frequency region from dynamic rehological measurements,probably caused by the interactions among the silica particles in the silica network and the polymer matrix.

References

1. Crosby AJ and Lee JY. Polymer Reviews 2007;47(2):217-229.

2. Balazs AC, Emrick T, and Russell TP. Science 2006;314(5802):1107-1110.

3. Cassagnau P. Polymer 2008;49(9):2183-2196.

4. Liu ZH, Kwok KW, Li RKY, and Choy CL. Polymer 2002;43(8):2501-2506.

5. Hussain F, Hojjati M, Okamoto M, and Gorga RE. Journal of Composite Materials 2006;40(17):1511-1575.

6. Osman MA and Atallah A. Polymer 2006;47(7):2357-2368.

7. Kontou E and Niaounakis M. Polymer 2006;47(4):1267-1280.

8. Zou H, Wu S, and Shen J. Chemical Reviews 2008;108(9):3893-3957.

9. Zhang MQ, Rong MZ, Zhang HB, and Friedrich K. Polymer Engineering & Science 2003;43(2):490-500.

10. Dorigato A and Pegoretti A. Engineering Fracture Mechanics 2012;79(0):213-224.

11. Lai S-M, Chen J-R, Han J-L, Yu Y-F, and Lai H-Y. Journal of Applied Polymer Science 2013;130(1):496-503.

12. Makarov C, Khalfin RL, Makarov V, Cohen Y, Sertchook H, Elimelech H, and Avnir D. Polymers for Advanced Technologies 2007;18(9):712-719.

13. Grubb DT and Prasad K. Macromolecules 1992;25(18):4575-4582.

14. Butler MF, Donald AM, Bras W, Mant GR, Derbyshire GE, and Ryan AJ. Macromolecules 1995;28(19):6383-6393.

15. Russell KE, Hunter BK, and Heyding RD. Polymer 1997;38(6):1409-1414.

16. Sepehr M, Utracki LA, Zheng X, and Wilkie CA. Polymer 2005;46(25):11569-11581.

17. Sinha Ray S and Okamoto M. Macromolecular Materials and Engineering 2003;288(12):936-944.

18. Sinha Ray S and Okamoto M. Progress in Polymer Science 2003;28(11):1539-1641.

19. Galgali G, Ramesh C, and Lele A. Macromolecules 2001;34(4):852-858.

20. Hoffmann B, Dietrich C, Thomann R, Friedrich C, and Mülhaupt R. Macromolecular Rapid Communications 2000;21(1):57-61.

21. Dorigato A, Pegoretti A, and Penati A. eXPRESS Polymer Letters 2009;4(2):115-129.

22. Suprakas SR. J. Ind. Eng. Chem. 2006;12:811-842.

Chapter 3. Extensional Flow-Induced Crystallization in Isotactic Polypropylene Melt

3.1 Introduction

Flow-induced crystallization of polymers has been an important subject in polymer processing. The applied flow could substantially influence the development of a precursor structure, which would eventually dictate the final morphology and properties [1-5]. Polyolefins, especially polyethylene (PE) and polypropylene (PP), occupy a large part of the total polymer production every year in the world and have wide applications in different fields. Therefore, understanding the relationship between applied flow and formed precursor structure during the early crystallization stage is essential in providing useful information to direct best processing conditions for the desired products.

The well-documented shish-kebab structure is found to be a fundamental form of the precursor structure in the entangled polymer melt under an external flow field [6-10]. This superstructure consists of a central fibrillar core (shish structure) and disk like lamellar crystals (kebab structure) that is perpendicular to the shish. The formation of this kind of morphology is sensitive to the applied flow and also the intrinsic properties of polymer, especially those long chains in the melt. After decades of study, the mostly accepted theory right now is the

coil-stretch transition. It was first proposed by de Gennes in dilute polymer solution, in which the hydrodynamic interaction between the stretched chain and the solution was considered [11]. Later, Keller extended it in the molten polymer, and proposed two critical conditions in the coil-stretch transition [12-15]. Firstly, for monodisperse polymers, there exists a critical strain rate $\dot{\varepsilon}_c$. In polymer solution or melt, polymer chains would only be stretched when the strain rate exceeds a critical value. Besides, under a fixed flow rate, a critical molecular weight (M*) exists, which means that in a polydisperse polymer solution or melt, only polymer chains with a higher molecular weight than M* could remain in the stretched state after flow, while the chains with lower molecular weight will roll back into the coiled state without experiencing the coil-stretch transition, because the higher molecule weight polymer chains have longer relaxation times, which can help them keep at the stretched state. The critical strain rate and the molecular weight are influenced by each other. It is presumed that their relationship could be expressed as $\dot{\varepsilon}_c \propto (M^*)^{-\beta}$. An increase of strain rate would affect the critical molecular weight. With higher strain rates, more polymer chains would undergo the coil-stretch transition. Accordingly, polymer species with high molecular weight in a polydisperse melt or blend melt can play an essential role in the formation of the precursor crystal structure under flow. Muthukumar simulated the flow-induced crystallization from a solution containing different chains and showed that long chains could be stretched and then formed the shish cores, while the short chains aggregated as kebabs [16]. However, there still exists a great deal of controversial problems in the flow induced precursor structure. The true process of coil-stretch transition and the clear definition of the two critical conditions require further investigation [17-21].

There are different kinds of polymer processing methods involving the flow induced crystallization, such as extraction, injection molding, fiber spinning, film blowing, etc. In each method, the nature of the flow is different. The extension of polymer chains is highly dependent on the nature of the flow. The applied flow fields may consist of both rotational and extensional components. The extensional part will contribute to the deformation of the polymer chain, while the rotational part could make the chain roll back (end-over-end tumbling of molecule) and impede the stretching of polymer chains. Chu et al [22, 23] compared the polymer dynamics under elongation flow and shear flow in a dilute polymer solution. They found that under steady shear flow, the mean fractional extension gradually increased with flow strength and finally only approach 0.4 – 0.5. This differed remarkably from the case of pure elongational flow, where the extension rises rapidly to a value close to the full contour length of the polymer chain. The situation in a polymer melt is more complex due to the interaction between molecules and the surrounding matrix. Most of the studies on the flow induced crystallization of a polymer melt use shear flow to inspect the precursor structure in the deformed polymer. In a simple shear flow, theoretically it is thought to be composed by equal parts of extensional and rotational component. So, the commonly used shear flow is a weak deforming force. It is unlikely to extend all the long chains in the solution or melt and will not attain a stable and strong stretched state. The usage of extension or extension dominant flow could eliminate or at least decrease the interference of the rotational component. However, most of the experiments using elongation flow are performed under dilute polymer solution. Extension dominant flow used in melt polymer crystallization study is still rare [13, 15, 24]. There are different ways to generate extensional or extensional

dominant flow. Recently, an apparatus based on a modified extensional rheometer device was used to generate extensional dominant flow and to study its influence on polymer melt using synchrotron X-ray scattering technique [25, 26]. This device was based on the SER equipment designed by Sentmanat [27]. The SER device was composed of a pair of drums on the bearing. The rotation of drums would wind up the sample fixed upon it and generate the elongation force. It was capable to adjust the flow applied on the polymer at different strain and strain rate, and to record the stress-strain curve simultaneously. Another kind of modified elongational rheometer that required smaller sample size and used a new type of clamps to extend the sample was developed [28]. A correlated work using this machine has also been reported for the elongation flow-induced morphological change of a diblock copolymer melt [29]. In this study, a custom built cross-slot flow device was used. The mechanical construction was different from the SER equipment mentioned above. Dominant extensional flow could be generated at the central location of two channels across the stagnation point. A detailed description about the device has been included in the experimental section below. This kind of construction was used previously for microscopy and rheometer [30, 31], and it could be used in a low viscosity polymer melt or even polymer solution. Pure extensional flow could generate a stable stretched effect on long polymer chains and will be a promising way to understand the nature of the shish-kebab precursor structure formation.

Studies of shear induced crystallization of polypropylene and its copolymers and blends have been previously reported extensively. In the current study, only one kind of isotactic polypropylene (iPP) with a weight averaged molecular weight (Mw) of 330,000 g/mol was

chosen to investigate the dynamic evolution of the precursor structure under the extensional flow condition by collecting the *in-situ* time-resolved small-angle X-ray scattering (SAXS) patterns. The study was focused on the influence of extensional flow on polymer at different strain rates and strains. Previously, correlated WAXD experiments were performed to study the crystallization behavior of isotactic polypropylene from diffraction patterns [32]. The SAXS scattering patterns will provide more information about the dynamic evolution of the shish and kebab precursor structure, which can help understand the mechanism during the extensional flow-induced crystallization.

3.2 Experiment

3.2.1 Materials

Isotactic polypropylene (*i*PP) (M_w = 330, 000 g/mol, polydispersity ~ 4.2, provided by ExxonMobil Company), was synthesized by using the Ziegler-Natta method and was used for the experiments directly.

3.2.2 Instrumentation

The extensional flow was produced in a specially designed instrument that contained a melt feeding chamber and a cross-slot flow cell. A schematic drawing is shown in Figure 3.1. In the feeding chamber, a motor-driven plunger was used to deliver the polymer melt from the barrel to

the cross-slot flow cell. The inner shape of the barrel was cylindrical in shape with 260 mm in length and 15.3 mm in diameter, which could store a maximum of about 48,000 mm^3 of polymer melts. The plunger was controlled by a stepping motor and could move at fixed speeds with a precision of 0.1 mm/sec.
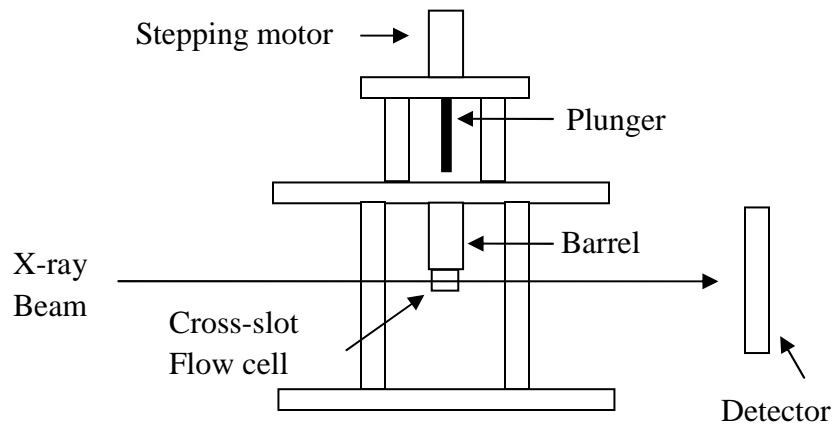
Figure 3.1 A schematic diagram showing melt feeding chamber and cross-slot flow cell.

The cross-slot flow cell was composed of three pieces of metal blocks. These blocks were composed of a pair of outflow channels (2 mm in depth and 2 mm in height) and could generate extensional flow at the central location of the two channels across the stagnation point. Figure 3.2 shows a schematic illustration. Two pieces of diamond windows were attached on both sides of the stagnation point (with Kapton films between them) for synchrotron X-ray measurements. Both the feeding chamber and the cross-slot flow cell could be heated up to 300 ˚C, and the temperature was controlled by a temperature controller with a thermocouple as the sensor. More specific details of the instrument could also be found elsewhere [32].
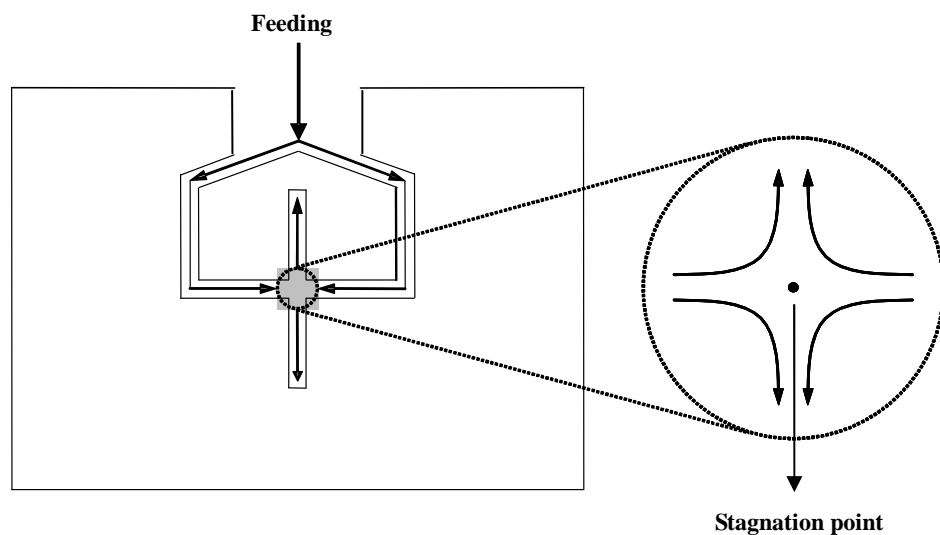
Figure 3.2 Schematic illustration of cross-slot flow cell.

The strain rate of the extensional flow generated in this cross-slot flow cell, $\dot{\varepsilon}$, could be calculated by using the following equation: $\dot{\varepsilon} = \dfrac{Q}{H^2 \cdot D} = \dfrac{S \cdot v}{H^2 \cdot D}$ [31], where Q is the volume flow rate; S is the barrel area; v is the plunging speeding; H and D are the height and depth of the outflow channels. According to the specific dimensions of this device, the equation could be simplified to $\dot{\varepsilon} = 23.2 \cdot v$ s^{-1}.

In-situ SAXS experiments were performed at the Advanced Polymers Beamline (X27C), the National Synchrotron Light Source (NSLS), Brookhaven National Laboratory (BNL). The wavelength of the synchrotron radiation was 1.371 Å. To acquire the dynamic evolution of the precursor structure, a charged coupled device (CCD, MAR-USA) detector was used to collect the 2D scattering patterns. This CCD had a resolution of 1024×1024 pixels and each pixel size was 158.44 μm. For the SAXS setup, the sample-to-detector distance was 1969 mm calibrated by

silver behenate. All X-ray images were corrected for background scattering, air scattering and synchrotron beam fluctuations.

3.2.3 Experimental procedure

Before testing, samples were first heated to 210 ˚C, which was sufficiently higher than its equilibrium melting temperature, for 5 min to remove any memory effects of prior thermal and mechanical histories. The melts were subsequently cooled to the experimental temperature of 163 ˚C, with a cooling rate of 3 ˚C/min. After holding for 3 additional minutes, the extensional flow was applied to the sample. The temperature was then maintained for one hour for SAXS data collections. The data acquisition time was 15 s and the data storage time was 5 s for each image collection. The strain rate dependence and strain dependence tests were performed. For strain rate dependence tests, the chosen strain rates were $\dot{\varepsilon}$ = 0, 4.6, 8.1, 11.6, 23.2 and 34.7 s^{-1}, with a fixed duration time, t_s = 15 s. For strain dependence measurements, a fixed strain rate $\dot{\varepsilon}$ = 23.2 s^{-1} was chosen, and different strains were obtained by applying the flow at different duration times, t_s = 0, 5, 10, 15, 20 and 25 s, and the strains were ε = 0, 116, 232, 348, 464 and 580, respectively.

3.3 Results and discussion

In the quiescent melt (strain rate $\dot{\varepsilon}$ = 0) and at low strain rates ($\dot{\varepsilon}$ = 4.6 and 8.1 s^{-1}), the SAXS patterns exhibited only diffused scattering features throughout the experimental period,

typical images for *i*PP samples without an ordered structure and preferred orientation. After the applied flow rate exceeds 11.6 s^{-1}, an oriented precursor structure was formed. Figure 3.3 shows the selected 2D SAXS patterns of *i*PP after applying extensional flow at various strain rates (a) 11.6 (b) 23.2 (c) 34.7 s^{-1} for 15 s. With high strain rates (b) and (c), a scattering maximum appeared in both the equatorial and meridian directions immediately after the cessation of extensional flow, which was an indication of the shish and kebab precursor structure [33, 34]. At a lower strain rate (a), an oriented structure also appeared after 200 s of applying the flow. In all the patterns, the scattering intensity gradually increased with time, especially for the kebab structure in the meridian direction.

Figure 3.3 Selected 2D SAXS patterns of *i*PP collected after flow cessation with strain rate: (a)11.6, (b) 23.2, and (c) 34.7 s^{-1} for 15 s.

In order to examine the time evolution of different components of the oriented structure and their relationship, the scattered intensity of shish (I_{shish}) and of kebabs (I_{kebab}) were separated by integration with following expressions:

$$I_{Shish} = 2\pi \int_{0.018}^{0.52} \int_{50^o}^{90^o} I(s,\phi)s^2 \sin\phi \, ds \, d\phi$$

$$I_{Kebab} = 2\pi \int_{0.018}^{0.52} \int_{0^o}^{50^o} I(s,\phi)s^2 \sin\phi \, ds \, d\phi$$

The intensity of shish is obtained by integration using the signal with a polar angle from 50˚ to 90˚, while for kebabs it is from 0˚ to 50˚. This can separate well the shish and kebab scattering signals in these SAXS patterns. The integrated value was similar to the scattering invariant, but the integration boundary was from 0.018 nm^{-1} to 0.52 nm^{-1} due to the limited detecting range. This value could reflect all the mean square density fluctuations in the system, including crystal, other ordered structures, and amorphous phase. The obtained I_{shish} and I_{kebab} could be used to quantitatively estimate the amount of shish and kebab structure. A schematic diagram for the calculation of integrated SAXS intensity of shish and kebab structure is shown in Figure 3.4.
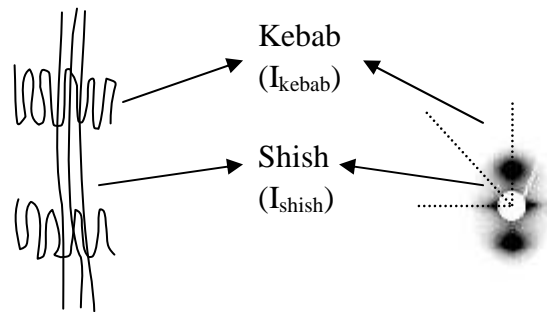
Figure 3.4 Schematic diagram for calculation of integrated SAXS intensity of shish (I_{shish}) and kebab (I_{kebab}) structure.

Integrated results of scattering patterns with strain rates of 11.6, 23.2 and 34.7 s^{-1} are shown in Figure 3.5. The intensity of the shish entity increased steadily in the beginning of the experimental period. However, the increasing trend nearly stopped after 500 s and became almost constant in all the plots at different flow rates. While for the kebab structure, except for the sample with 11.6 s^{-1} strain rate, the scattered intensity increased gradually throughout the whole experimental period. The formation of the shish structure was a faster process than that of the kebab structure, in agreement with previous results that stretched long chains would first form the shish core structure, followed by the attached folded coiled chains, which would compose of the kebab structure [33, 34]. The evolution of the oriented structure (for both shish and kebab structures) evidently depended on the strain rate of the elongation flow. Adopting Keller's theory, the formation of a precursor structure was closely related to the coil-stretch transition of polymer chains under the flow. With low strain rates ($\dot{\varepsilon}$ = 4.6 and 8.0 s^{-1}), no oriented structure was formed, since the applied strain rates were lower than the critical value $\dot{\varepsilon}_c$. When $\dot{\varepsilon}$ = 11.6, 23.2 and 34.7 s^{-1}, $\dot{\varepsilon} > \dot{\varepsilon}_c$, the applied extensional flow became strong enough to keep a certain amount of long chains in the stretched state even after the cessation of flow. The stretched chains would form the shish core and subsequently the lamella kebab structure. The critical strain rate value $\dot{\varepsilon}_c$ was within 8.0 s^{-1} and 11.6 s^{-1}.

Figure 3.5 Evolution of scattered intensity from shish and kebab in *i*PP after flow at different strain rates: 11.6, 23.2 and 34.7 s^{-1}.

To further inspect the relationship between shish and kebab structures, the ratios of I_{kebab} and I_{shish} were calculated and plotted in Figure 3.6. I_{kebab}/I_{shish} increased with time under all strain rate conditions. This finding was reasonable according to the coil-stretch transition theory. However, the ratio of I_{kebab}/I_{shish} showed a different evolution trend with different applied strain rate, especially at the low strain rate of 11.6 s^{-1}, where I_{kebab}/I_{shish} became much smaller when compared with the other two conditions after 500 s. A possible explanation is provided as follows. A strain rate of 11.6 s^{-1} was relatively small and might be insufficient to generate enough amounts of stretched long chains. It would then take a longer time to form nuclei from the stretched chains, and consequently could make it difficult for the coiled chains to adsorb on the nuclei to form a kebab structure. In other words, the scarcity of nuclei would impede the growth of the kebab structure and finally the I_{kebab}/I_{shish} value in 2500 s was significantly less

51

than that at high strain rates, while the evolution of I_{kebab}/I_{shish} was very similar at different strain rates of 23.2 and 34.7 s^{-1}, and the final value at 2500 s was almost the same,suggesting that the amount of kebab related to each unit of shish arrived at a saturated state at the end of the experiment time.

Figure 3.6 Ratios of scattered intensity (I_{Kebab}/I_{shish}) from shish and kebab in *i*PP after flow at different strain rates: 11.6, 23.2 and 34.7 s^{-1}.

Figure 3.7 shows selected 2D SAXS patterns of *i*PP, after applying the extensional flow, at various times and different strains (a) 116 (b) 348 (c) 580 (same strain rate 23.2 s^{-1} with different duration time 5, 15 and 25 s). The total applied strain on the melt along the outflow stream could be estimated by the equation: $\varepsilon = \int_{t1}^{t2} \dot{\varepsilon} \cdot t \cdot dt = \dot{\varepsilon} \cdot t_s$, where t_s is the flow duration time. At high strains ($\varepsilon = 348$ and 580), the oriented shish and kebab structure formed at the very early stage and the scattering intensity of the kebab part increased with time. While for the lower strain ($\varepsilon = 116$), the oriented precursor structure did not appear first. Until at 500 s, a weak

scattered signal was detected in the meridian direction and even at 2500 s, the scattering signal from the oriented structure was still not very strong. There was no obvious crystal reflection peak detected in the WAXD patterns at low strain values of 116 and 232, as shown in our previous experiment [32]. The results from SAXS and WAXD seemed inconsistent. It should be noticed that SAXS was more sensitive than WAXD in detecting ordered structures, providing that it had sufficient electron density difference with the surrounding environment. The scattering intensity was proportional to the volume fraction of the ordered structure, as well as the density contrast between the ordered structure and the surrounding matrix (the amorphous matrix here). These ordered structures might not necessarily form a crystal structure. WAXD could only detect X-ray diffraction from well-ordered crystal structures. In this case, the appearance of a scattering signal in the SAXS pattern indicated the existence of a precursor ordered structure after flow. This observation was not contrary to the conclusion obtained from WAXD experiments. The precursor structure could form under strain rates larger than the critical strain rate $\dot{\varepsilon}_c$, while a certain amount of time (critical strain) would be necessary for these precursor structures to form crystals, explaining why the scattering signal was observed in the SAXS patterns but not in the WAXD patterns for *i*PP with strains of 116 and 232.
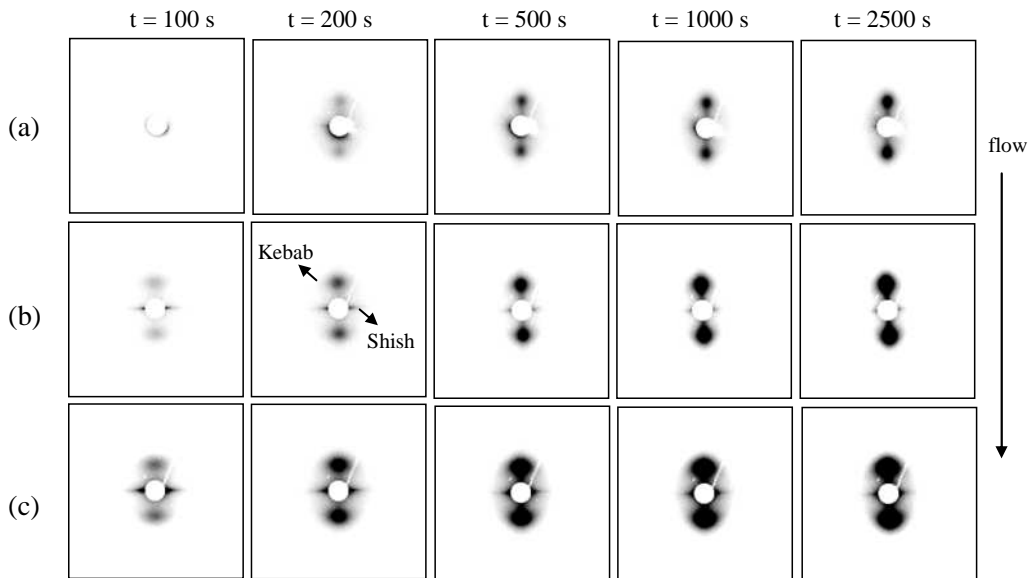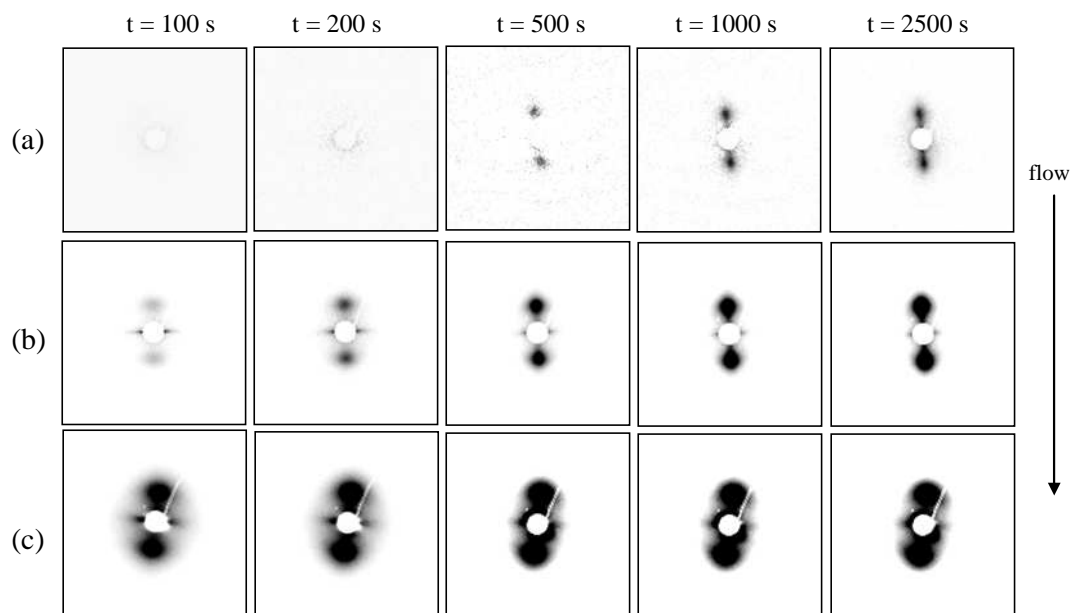
Figure 3.7 Selected 2D SAXS patterns of *i*PP collected after flow cessation with strain: (a) 116, (b) 348, and (c) 580.

The evolution of the scattered intensity from shish and kebab entities in *i*PP after applying the extensional flow at different strains of 116, 348 and 580 are plotted in Figure 3.8. The calculation method was the same as the strain rate dependent experiment as shown in Figure 3.4 and Figure 3.5. The shish structure mainly generated in the first 500 s, while the kebab structure grew steadily during the experimental time. This phenomenon was also observed in the strain rate dependent experiment as shown previously. However, the situation at the highest strain ($\varepsilon =$ 580) was different. The increasing trend of the scattered intensity from the kebab structure ceased after 500 s, which was quite similar to the behavior of the shish structure. It seemed that the amount of kebab structure became saturated in a short time period when applying flow at high strain. Figure 3.9 shows the ratio of scattered intensity (I_{Kebab}/I_{shish}) at different strains. The plot for the highest strain ($\varepsilon = 580$) showed abnormal behavior again. I_{Kebab}/I_{shish} increased

quickly before 500 s, and then stopped and even decreased slightly to a level much smaller than the value at strain $\varepsilon = 348$. Considering the coil-stretched theory, a possible explanation could be that with high strain flow, a sufficiently long time duration would favor the orientation of all stretched polymer chains with molecular weights larger than the critical value M^*. In other words, most of the long chains could be stretched and bundles of these parallel chains would form the primary nuclei and grew to the shish core structure along the flow direction. The applied flow in a relatively long time (25 s) helped the stretched chains to complete this thermodynamic process. With most of these stretched chains form the shish entities, the scattering intensity of shish structure at high strain ($\varepsilon = 580$) was much higher than that at low strain conditions, as shown in Figure 3.8. Thus, a lesser amount of stretched chains were relaxed back and a lesser amount of coiled chains were available to adsorb on the shish core to form the kebab structure, and finally, the kebab scattering intensity reached a plateau value quickly during the crystallization process.
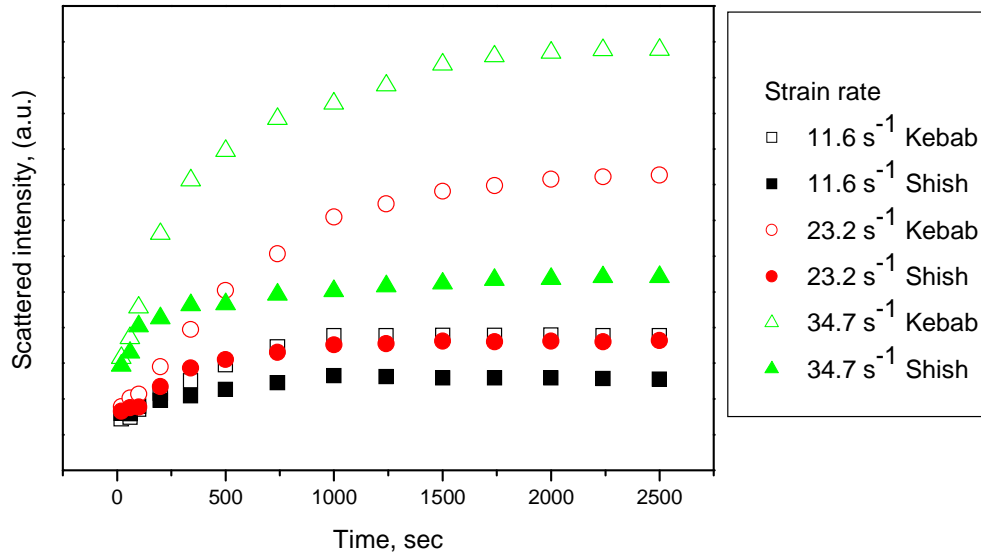
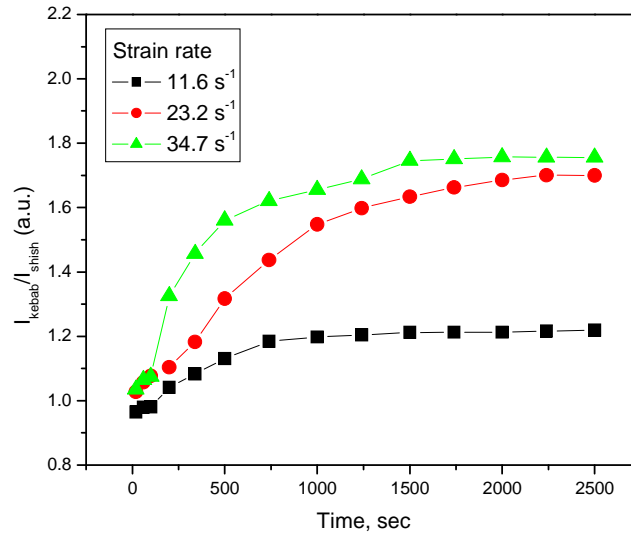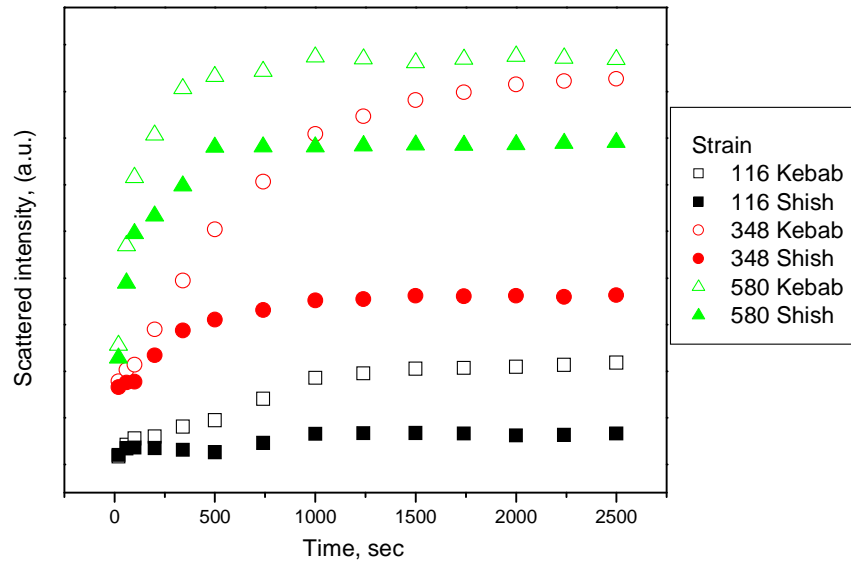Figure 3.8 Evolution of scattered intensity from shish and kebab in *i*PP after flow at different strain: 116, 348 and 580.
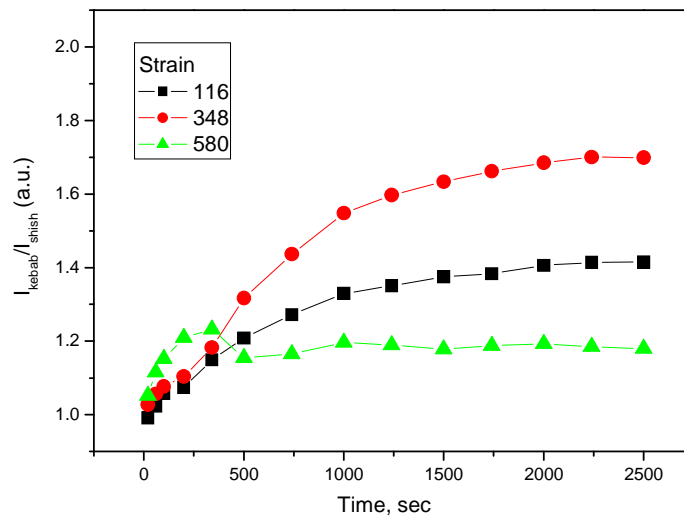
Figure 3.9 Ratios of scattered intensity (I_{Kebab}/I_{shish}) from shish and kebab in *i*PP after flow at different strain: 116, 348 and 580.

The intensity of scattering patterns can provide quantitative information of the ordered structure, while the intensity distribution of SAXS patterns reflects the dimensional information of ordered structure (shish and kebab entities). Here, the Ruland streak method was applied to estimate the kebab diameter. This method was first introduced to analyze the equatorial streak feature of polymer and carbon fibers in the SAXS pattern [35, 36]. Since this method basically relies on the separation of size and orientation distribution effects on the scattering width, it could also be applied to the meridian streak in separating the average kebab diameter, <D>, and its misorientation in the shish-kebab structure (as long as the kebab diameter and orientation is finite)[37]. If all the azimuthal distribution of the scattering pattern is modeled by a Lorentzian function, the observed azimuthal integral width (radian) of the streak, B_{obs}, the average kebab diameter, <D>, and the azimuthal width due to misorientation, B_ϕ will have following relationship:

$$B_{obs}(s) = \frac{1}{\langle D \rangle s} + B_\phi$$

If all the azimuthal distributions have Gaussian expressions, then the relationship becomes:

$$B_{obs}^2(s) = \left(\frac{1}{\langle D \rangle s} \right)^2 + B_\phi{}^2$$

In this study, it was found that a better fit was obtained with the Lorentzian function for all of the azimuthal distributions. Thus, based on the plot, the slope, 1/<D>, was the inverse of the kebab diameter and the intercept, B_ϕ, was the misorientation. A typical example of the analysis for the polypropylene with applied extensional flow (strain rate of 23.2 s^{-1} and duration time of 15 s) at

200 s is shown in Figure 3.10. From the plot, the estimated Kebab diameter at 200 s was about

198 nm with a misorientation width, B_ϕ, of around 0.3.
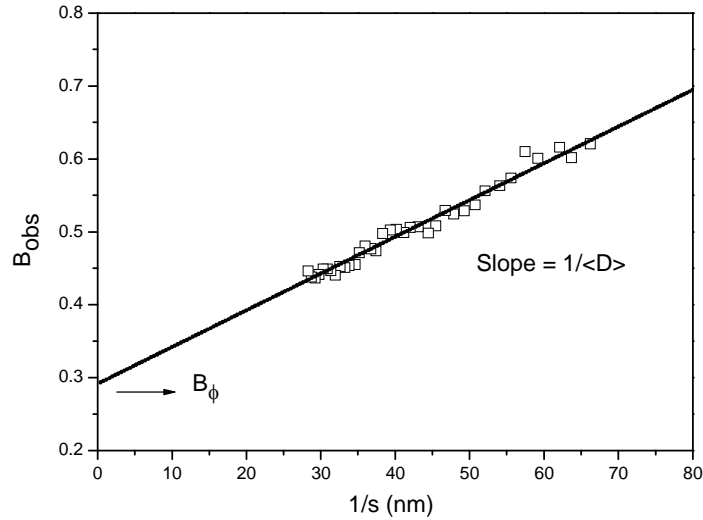
Figure 3.10 Plot of integral width (B_{obs}) versus reverse of scattering vector (1/*s*) for polypropylene at 200 s after an applied extensional flow (strain rate 23.2 s^{-1} and duration time 15 s). To avoid large errors, only the intermediate s region ($0.015 < s < 0.035$ nm-1) was selected.

The Ruland streak analysis method was used to roughly estimate the size of the kebab structure. The changes of the average kebab diameter for polypropylene at applied extensional flow conditions of $\dot{\varepsilon}$ = 23.2 s^{-1}, t_s = 15 s; $\dot{\varepsilon}$ = 34.7 s^{-1}, t_s = 15 s; and $\dot{\varepsilon}$ = 23.2 s^{-1}, t_s = 25 s were calculated separately (the situation with smaller strain rates or smaller strains was not included due to relatively low scattering intensity). The obtained results are shown in Figure 3.11. The kebab disk grew relatively fast in the beginning of the experiment, and then gradually reached to a plateau value. It is interesting to find that the evolution of the kebab diameter was

quite similar for polypropylene with flow conditions of $\dot{\varepsilon}$ = 23.2 s^{-1}, t_s = 15 s; and $\dot{\varepsilon}$ = 34.7

s^{-1}, t_s = 15 s. However, for the situation with $\dot{\varepsilon}$ = 23.2 s^{-1}, t_s = 25 s, the kebab diameter was

obviously smaller when compared with others after 500 s. Typically in this case, the kebab

diameter was around 250 nm, while for the other two conditions, the kebab reached around 290

nm at the end of the experimental time period.
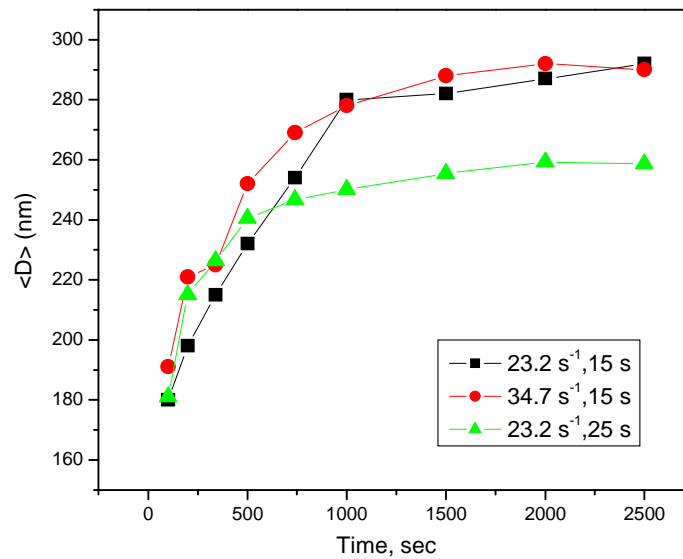
Figure 3.11 Changes of the average kebab diameter for propylene with applied extensional flow conditions of $\dot{\varepsilon}$ = 23.2 s^{-1}, t_s = 15 s; $\dot{\varepsilon}$ = 34.7 s^{-1}, t_s = 15 s; and $\dot{\varepsilon}$ = 23.2 s^{-1}, t_s = 25 s, respectively. The average kebab diameter was estimated by using the Ruland streak analysis method.

There are still conflicting opinions regarding the formation of lamella. Different models

have been proposed to explain the experiment results. Generally, under quiescent conditions,

lamella will grow from the melt. Polymer chains will fold and attach to the lateral sides of other

chains. The lamellar thickness is determined by the supercooling condition below the

equilibrium melting point given by the Gibbs–Thomson equation. The lamellar thickness should be close to a thermodynamic variable, which is mainly dependent on the crystallization temperature. Though no direct evidence indicates the influence of external force on the thickness of the lamellar crystal, it is believed that the kebab disk thickness would be less influenced by the applied flow. There were previous studies on the shear induced crystallization of polypropylene that reported there was almost no change in the lamellar thickness and the long period with increasing shear rates [38]. If the thickening of lamellae is not considered during the crystallization process, after the cessation of flow, the kebab gradually increases along the lateral direction. When the kebab diameter reaches to a certain amount, the growing rate will decrease and secondary crystallization may happen. For the situation with $\dot{\varepsilon}$ = 23.2 s^{-1}, t$_s$ = 25 s, the lamellar disk diameter did not reach to a plateau value, as it stopped at a much smaller value. Recalling the evolution of I$_{shish}$, I$_{kebab}$ and their ratios as shown in Figure 3.8 and Figure 3.9, and for the applied flow with longer duration time, stretched polymer chains had enough time to form the shish entities. There were then a less amount of oriented polymer chains left to form the lamella disk, and the lamella disk could not grow further. Finally, the disk diameter under flow of high strain was smaller when compared with others.

Simulation of 2D SAXS patterns based on a shish-kebab structure model was previously proposed [34, 39]. The model assumed a periodic disk-like kebab structure with a cylindrical symmetry around the shish-axis. For simplicity, without losing the important feature of the structure, the kebab was assumed to have a perfect orientation along the shish (the flow direction) and the lamellar disk had infinite height. The scattering contributions from the shish were

ignored, as it mainly appeared in the equatorial direction and could be analyzed separately. Totally, there were six parameters to simulate the scattering of the kebab. These include the kebab disk average diameter D, the distribution h(D), thickness T, the distribution h(T), the distance between the centers of nearest neighboring disk L, and the distribution h(L). In this model, introducing three distribution parameters could simulate the real situation and give an improved fitting on the scattering pattern. From the simulation, it was found that an increase in the polydispersity of disk diameter, thickness and long period, i.e., h(D), h(T) and h(L), increased the scattering intensity at low angles due to the large density fluctuations, while the scattering maximum peak became diffused [34, 39]. Thus, the shish-kebab structure with small h(D), h(T) and h(L), which represented a well ordered lamella structure, had a sharp scattering maximum peak and formed two points patterns in the meridian direction. Previous study in shear induced crystallization showed that the scattering maximum peak became diffused or even disappeared with increasing crystallization time. However, in the current extensional flow induced crystallization experiment, the scattering curves were somewhat different when compared with previous results. The 1D SAXS scattering curves for polypropylene in the meridian direction with flow strain rate of 23.2 s^{-1}, duration time of 15 s at different experiment times are plotted in Figure 3.12. The scattering maximum appeared at around 100 s after the cessation of flow in the SAXS patterns. The intensity of the maximum increased in the beginning and did not become diffused with crystallization time, indicating that the polydispersity of the lamellar disk dimensional size did not increase significantly under the current experimental conditions. With low distribution value, two distinct scattering maxima was observed along the

meridian direction and formed a two-point pattern, while with a large distribution value, the

scattering became broader and resembled streaks. Most of the kebab scattering patterns under the

extensional flow conditions showed well-defined dumbbell like two-point patterns with a clear

distinct scattering maxima. Though these were not compared quantitatively, the scattering

patterns were different When compared with our previous results from shear induced

crystallization (shear flow on polypropylene or polyethylene) [33, 40]. The results seemed

reasonable as the extensional flow was a relatively strong force and it had a less amount of

rotational components inside, providing a more efficient way to form an oriented structure. The

detail comparison between the extensional flow and shear flow needs to be studied further.
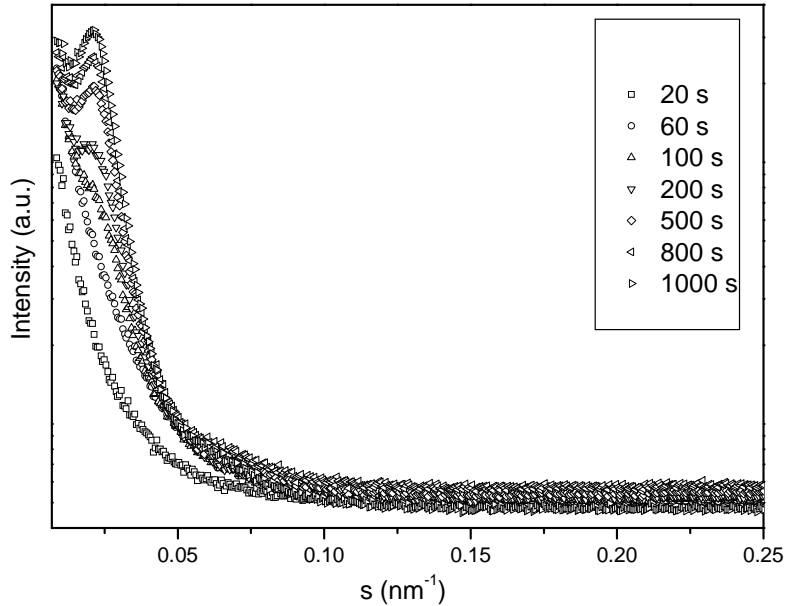
Figure 3.12 Experimental 1D SAXS profiles along meridian direction for polypropylene under extensional flow with $\dot{\varepsilon}$ = 23.2 s^{-1}, t$_s$ = 15 s at crystallization times of 20 s, 60 s, 100 s, 200 s, 500 s, 800 s and 1000 s.

For the strain rate dependence experiment, oriented shish and kebab formation appeared only when the strain rate exceeded the critical value $\dot{\varepsilon}_c$, ($\dot{\varepsilon}$ = 11.6, 23.2 and 34.7 s^{-1}). While at the fixed strain rate $\dot{\varepsilon}$ = 23.2 s^{-1}, the kebab scattering pattern was observed in the smallest strain ($\varepsilon = 116$) in the experiment. With longer duration time, i.e., stronger strain, stretched chains will be kept in the stretched condition after the cessation of flow to form the shish structure. A certain amount of induced time was necessary for these chains to stretch and relax in order to form crystals. There were two effects that could have significant influences on the flow induced crystallization. After applying the external force, the polymer chains were stretched and oriented along with the flow direction. These polymer chains then had two choices: either forming a shish structure or relaxing back to coiled chains that could form kebabs later. This formation could depend on many factors, such as molecular properties, temperature, applied strain rate, duration time et al. With polypropylene, the molecular structure could be of importance. With increasing strain rate, more polymer chains could undergo the coil-stretch transition. With increasing strain, longer induced time should help these bundles of stretched chains to form more shish entities and the relaxed coiled chains could adsorb on the shish to form kebab lamella structures. High strains should increase the crystallization rate, while might not help much on the final crystallinity.

3.4 Conclusions

By using a specially designed cross-slot flow cell, a stable extensional flow was generated. The extension flow induced crystallization in a mono-component polyolefin, isotactic

polypropylene (*i*PP), was studied. An oriented precursor structure was detected and the structure showed a typical shish and kebab form. Detail mechanism of the shish and kebab formation could be closely related to the characteristics of the applied extension flow. By adopting the extensional flow at different strains and strain rates, the oriented precursor structure only appeared when the applied strain rate exceeded the critical strain rate $\dot{\varepsilon}_c$. The ordered precursor structure, including both shish and kebab entities, increased with increasing strain rate and strain. SAXS was more sensitive than WAXD to detect the flow induced oriented structure. The kebab scattering pattern which could not be detected in WAXD patterns was observed in SAXS patterns at low strains. From 2D SAXS patterns in the meridian direction, the growth of the lamellar disk diameter was estimated. Under high strain conditions, the oriented kebab did not increase any further when the strain value was higher.

References

1. Flory PJ. Journal of Chemical Physics 1947;15(6):397-408.

2. Ziabicki A. Fundamentals of Fiber Formation: The Science of Fibre Spinning and Drawing, Wiley: New York 1976.

3. Keller A and Kolnaar HWH. Mat. Sci. Tech. 1997;18:189.

4. Eder G and Janeschitz-Kriegl H. Mat. Sci. Tech. 1997;18:268.

5. Kumaraswamy G. J. Macromol. Sci. Polym. Rev. 2005;45:375.

6. Mitsuhashi S. Bull. Text. Res. Inst. 1963;66:1.

7. Pennings AJ and Kiel AM. Kolloid Z. Z. Polym 1965;205:160.

8. Binsbergen FL. Nature 1966;211:516.

9. Keller A and Machin MJ. J. Macromol. Sci. Phys. 1967;B1:41.

10. Hill MJ and Keller A. J. Macromol. Sci. Phys. 1969;B3:153.

11. de Gennes PG. J. Chem. Phys. 1974;60:5030.

12. Pope DP and Keller A. Colloid & Polymer Science 1978;256(8):751-756.

13. Miles MJ and Keller A. Polymer 1980;21(11):1295-1298.

14. Keller A and Odell JA. Colloid & Polymer Science 1985;263(3):181-201.

15. Keller A and Kolnaar JWH. Progress in Colloid & Polymer Science 1993;92:81-102.

16. Dukovski I and Muthukumar M. J. Chem. Phys. 2003;118:6648.

17. Seki M, Thurman DW, Oberhauser JP, and Kornfield JA. Macromolecules 2002;35(7):2583-2594.

18. Janeschitz-Kriegl H, Ratajski E, and Stadlbauer M. Rheologica Acta 2003;42(4):355-364.

19. Elmoumni A, Winter HH, Waddon AJ, and Fruitwala H. Macromolecules 2003;36(17):6453-6461.

20. Schrauwen BAG, Breemen LCAv, Spoelstra AB, Govaert LE, Peters GWM, and Meijer HEH. Macromolecules 2004;37(23):8618-8633.

21. Wang M, Hu W, Ma Y, and Ma Y-q. Macromolecules 2005;38(7):2806-2812.

22. Smith DE and Chu S. Science 1998;281:1335.

23. Smith DE, Babcock HP, and Chu S. Science 1999;283:1724.

24. van Meerveld J, Peters GWM, and Hütter M. Rheologica Acta 2004;44(2):119-134.

25. Yan T, Zhao B, Cong Y, Fang Y, Cheng S, Li L, Pan G, Wang Z, Li X, and Bian F. Macromolecules 2010;43(2):602-605.

26. Tian N, Zhou W, Cui K, Liu Y, Fang Y, Wang X, Liu L, and Li L. Macromolecules 2011;44(19):7704-7712.

27. Sentmanat ML. Rheologica Acta 2004;43(6):657-669.

28. Meissner J and Hostettler J. Rheologica Acta 1994;33(1):1-21.

29. Kwon YK, Ko YS, and Okamoto M. Polymer 2008;49(9):2334-2341.

30. Perkins TT, Smith DE, and Chu S. Science 1997;276:2016-2021.

31. Odell JA and Carrington SP. Journal of Non-Newtonian Fluid Mechanics 2006;137(1–3):110-120.

32. Keum JK. Ph. D. Thesis. 2007, Stony Brook University.

33. Somani RH, Yang L, Hsiao BS, Agarwal PK, Fruitwala HA, and Tsou AH. Macromolecules 2002;35(24):9096-9104.

34. Somani RH, Yang L, Zhu L, and Hsiao BS. Polymer 2005;46(20):8587-8623.

35. Perret R and Ruland W. Journal of Applied Crystallography 1969;2(5):209-218.

36. Perret R and Ruland W. Journal of Applied Crystallography 1970;3(6):525-532.

37. Keum JK, Somani RH, Zuo F, Burger C, Sics I, Hsiao BS, Chen H, Kolb R, and Lue C-T. Macromolecules 2005;38(12):5128-5136.

38. Wen H, Jiang S, Men Y, Zhang X, An L, Wu Z, and Okuda H. J. Chem. Phys. 2009;130:164909.

39. Keum JK, Burger C, Hsiao BS, Somani R, Yang L, Chu B, Kolb R, Chen HY, and Lue CT. Progr. Colloid. Polym. Sci. 2005;130:114.

40. Somani RH, Yang L, Hsiao BS, Sun T, Pogodina NV, and Lustiger A. Macromolecules 2005;38(4):1244-1255.

Chapter 4. Uniaxial Stretching of Ionic Liquid/Ultra-High Molecular Weight Polyethylene Blends

4. 1 Introduction

The incorporation of ionic liquids into polymer systems has been an interesting topic because ionic liquids can be used as solvents, processing aides, and plasticizers, to facilitate the synthesis and processing of polymers, as well as to enhance the polymer properties [1-4]. Ionic liquid is a salt with a low melting point, allowing it to stay in the liquid state at relatively low temperatures. Different from ordinary organic solvents, ionic liquids consist entirely of ions and thus have many unique properties, e.g. they are nonflammable, thermally stable, non-volatile, and have high ion conductivity [1, 5-6]. The most notable application of ionic liquids in polymers is the usage as polymerization solvents. Because of the unique properties of ionic liquids, the course of polymerization is often different from those of common solvents. This has been seen in radical polymerization, ionic polymerization, polycondensation and atom transfer radical polymerization (ATPR) involving ionic liquids [7-12]. In addition, ionic liquids can also be used as solvents to dissolve polymers with poor solubility in common solvents. These polymers include biopolymers such as silk, wool [13-15] and cellulose [16], just to name a few.

In this study, we explore the subject related to another application that is the formation of polymeric blends with ionic liquids. The low volatility, thermal stability and high conductivity of ionic liquids and their interactions with the polymer matrix make them good candidates as solid electrolytes, suitable for battery and fuel cell applications [3]. The ionic liquids can also be added to solid polymers as plasticizers, which would increase the flexibility of the matrix as well as facilitate its processability. For example, Scott et al [17, 18] reported that imidazolium-based ionic liquids were good plasticizers for processing of poly methyl methacrylate (PMMA). They found that both glass transition temperature and elastic modulus decreased with increasing content of ionic liquid. Similar plasticization effect was also observed in systems of different polymers and ionic liquids [19, 20]. It was found that many traditional plasticizers were not suitable for high temperature usage, but ionic liquids could sustain their high temperature applications.
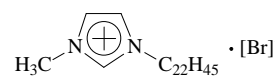
The goal of this study is to investigate the role of ionic liquids in affecting the structure and morphology of semi-crystalline polymers under deformation, where ionic liquids are used as plasticizers. The chosen polymer matrix was ultra-high molecular weight polyethylene (UHMWPE) and the chosen ionic liquid (IL) was 1-docosanyl-3-methylimidazolium bromide. Since the molecular weight of UHMWPE was extremely high (the weight average molecular weight Mw is usually in the range of several millions), the polymer possessed a great deal of chain entanglements and was very difficult to melt process. The dense entanglement structure greatly affects the crystalline structure and morphology of UHMWPE, resulting in high modulus, high tensile strength but very low elongation-to-break ratio. Various kinds of low molar mass

additives were developed and tested to improve the processability of UHMWPE. One example was the use of low molecular weight paraffin that could enhance the mobility of highly entangled UHMWPE chains during processing and be removed after the process. In this work, we demonstrate that the type of ionic liquid, having a long aliphatic tail that is compatible to the polyethylene backbone, can also be used for the same purpose and be retained in the UHMWPE matrix to create a new material. The chosen IL/UHMWPE blends were prepared by the solution mixing method to ensure the homogenous distribution of IL in the UHMWPE matrix. Simultaneous synchrotron wide-angle X-ray diffraction (WAXD) and small-angle X-ray scattering (SAXS) measurements in combination with uniaxial tensile deformation were performed on the blends and the control sample (i.e., pure UHMWPE) to understand the structure, processing and performance relationships.

4.2 Experimental

4.2.1 Materials and Preparation

The UHMWPE sample Hizex 340M was obtained from Mitsui Chemical Co. Ltd., Japan. It had a weight average molecular weight (M_w) of 1.5×10^6 g/mol and a polydispersity of about 10.5. The chosen ionic liquid was 1-docosanyl-3-methylimidazolium bromide ionic liquid (IL)

, synthesized in our laboratory using the procedures described elsewhere [21]. The nanocomposite was prepared based on the solution mixing method as follows. First, the

desired amount of IL was dissolved in decalin to form a homogenous solution. The UHMWPE sample (1 wt % of decalin solution) along with 1 wt % (based on the amount of UHMWPE) of antioxidant BHT (2,6-di-tert-butyl-4-methylphenol) were subsequently added into the IL/decalin solution. The whole mixture was then heated to 140 ℃ for 1 hour with vigorous stirring until the mixture became a clear solution. The UHMWPE/IL solution was cooled to room temperature and decalin was extracted from the suspension. The recovered product was dried in a vacuum oven at 60 ℃ for 2 days. The thermogravimetric analysis (TGA) traces did not show any residues of decalin in the sample.

The control sample (pure UHMWPE) and two nanocomposites with different IL contents: 0.6 wt % and 3 wt % (based on the amount of UHMWPE) were prepared using the same procedure. Hereafter, they were referred as the samples of 0%, 0.6% and 3% IL/UHMWPE, respectively. These samples were melt-pressed into flat films (held at 170 ℃ and 2.0 MPa for 5 minutes) for simultaneous synchrotron X-ray/deformation studies. The melting temperature of each sample was determined from differential scanning calorimetry (DSC) at a heating rate of 10 ℃/min under dried nitrogen gas flow. The crystallinity of UHMWPE was estimated from DSC using the measured value of heat of fusion (in perfect PE crystals, the heat of fusion was assumed to be 290 J/g [22]). Table 4.1 lists the crystallinity results.

Table 4.1 Melting temperature and crystallinity of IL/UHMWPE blends and pure UHMWPE from DSC measurements.

IL content (%)	melting temperature (°C)	crystallinity (%)
0%	131.1	61.5
0.6%	129.7	59.2
3%	127.4	53.8

4.2.2 Simultaneous X-ray and Deformation Measurements

In-situ wide-angle X-ray diffraction (WAXD) and small-angle X-ray scattering (SAXS) in combination with tensile deformation measurements were performed at the X27C Beamline, the National Synchrotron Light Source (NSLS), Brookhaven National Laboratory (BNL). The wavelength of the synchrotron radiation was 1.371 Å. To monitor the structure change, a charged coupled device (CCD, MAR-USA) detector was used to collect 2D scattering/diffraction patterns in real time. The CCD detector had a resolution of 1024×1024 pixels and each pixel size was 158.44 μm. The typical image acquisition time was 30 s for each data frame. The sample-to-detector distance was 1745 mm for the SAXS setup (calibrated with silver behenate) and 112.5 mm for the WAXD setup (calibrated with Al_2O_3). All X-ray images were corrected for background scattering, air scattering and synchrotron beam fluctuations.

The film sample was uniaxially and symmetrically stretched using a modified Instron 4442 tensile apparatus. The symmetrical deformation ensured that the focused X-ray beam always

illuminated on the same position of the sample during deformation. The original length of the sample between the Instron clamps was 20 mm, where the width was 5 mm and the thickness was 0.5 mm. A constant deformation rate, 4 mm/min, was applied to the specimen throughout the deformation study. The tensile experiments were carried out at room temperature (25 ºC) and 120 ºC, respectively. The stress and strain reported in this study were engineering stress and engineering strain measured directly from the Instron machine.

4.2.3 X-ray Data Analysis

The SAXS patterns of these samples exhibited discrete scattering peaks or scattering streak in different directions, which reflected the change of the lamellar structure during deformation. A semi-quantitative analysis was performed to measure the lamellar spacing by finding the position of the maximum scattering in the Lorentz-corrected SAXS profiles.

The quantitative analysis was applied on all 2D WAXD patterns, which were first corrected for background scattering, air scattering, beam fluctuations and Fraser correction (to compensate for the distortion from the flat-detector effect [23]). To simplify the analysis, the stretched samples were assumed to possess fiber symmetry, i.e., they had cylindrical symmetry along the stretching direction. This was confirmed by WAXD patterns taken from orthogonal directions perpendicular to the stretching direction, where near identical patterns were observed. To integrate the WAXD pattern along the scattering vector, the scattered intensity was expressed as $I(s) = 2\pi \int_{0^o}^{180^o} I(s, \phi) s^2 \sin \phi d\phi$, where the Lorentz correction was used to obtain the true mass distribution in the system. The calculated (Is^2 vs. s) profile was then separated into different

crystal peaks and an amorphous background, where the quantity of each component could be determined (a typical example is shown in Figure 4.1). The 2D WAXD patterns were further separated into two parts: isotropic part and anisotropic part using the halo method [24], as illustrated in Figure 4.2. The isotropic part was formed due to the unoriented species, including amorphous and unoriented crystal phases; while the anisotropic part was formed due to the oriented species, including oriented mesomorphic and crystal phases.
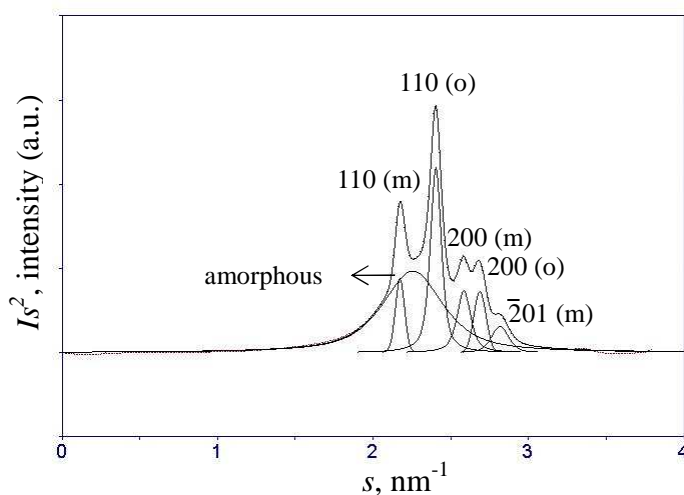
Figure 4.1 Deconvolution of reflection peaks from an integrated WAXD intensity profile. (o) and (m) indicate the reflection peaks from orthorhombic and monoclinic phase of polyethylene crystal, respectively.
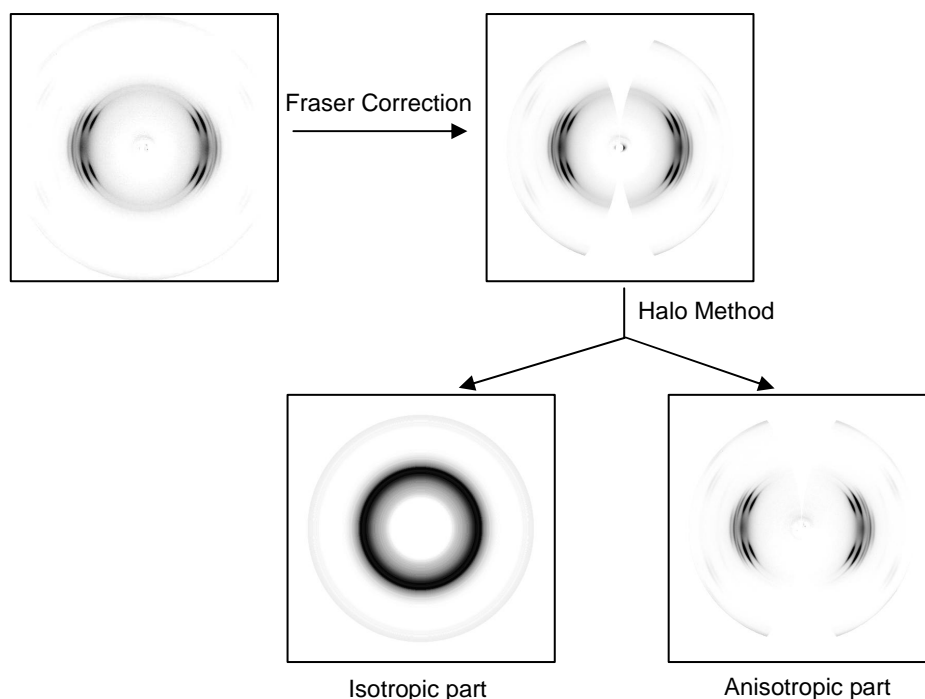
Figure 4.2 Schematic diagrams for separation of oriented part and unoriented part from a 2D WAXD pattern.

4.3 Results and Discussion

Simultaneous X-ray and tensile deformation measurements were first carried out at 25 ℃. Figure 4.3 shows the stress-strain curves for all three samples. It was found that by adding ionic liquid, the yield strength decreased (the 3% IL/UHMWPE exhibited the lowest yield point value), but the elongation-to-break ratio increased (e.g., 104 % for pure UHMWPE, 338 % for 0.6% IL/UHMWPE and 252 % for 3% IL/UHMWPE). The final values of tensile strength for the three samples, however, were quite comparable. Thus, the incorporation of ionic liquid into UHMWPE could largely increase the elongation-to-break ratio while keeping similar or slightly higher tensile strength.
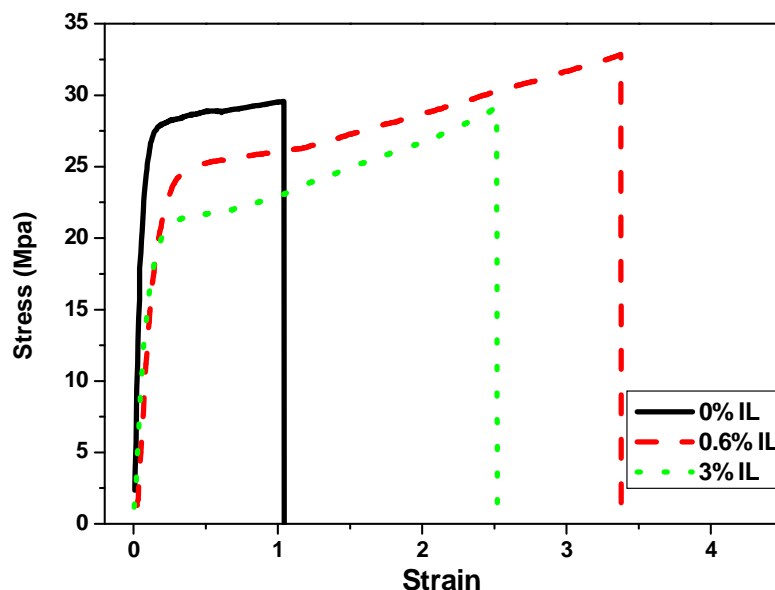
Figure 4.3 Stress-strain curves of UHMWPE and two IL/UHMWPE blends (0.6% and 3% IL) at 25 ℃.

The in-situ SAXS and WAXD results could provide detailed structure information (from lamellar to crystal) of the system during the stretching process. It was found that two IL/UHMWPE blends exhibited very similar trends in terms of the changes of scattering/diffraction patterns during deformation, while pure UHMWPE did not show notable variations in scattering/diffraction patterns due to the short elongation-to-break ratio. The exemplary results from the 0.6% IL/UHMWPE blend are illustrated in Figure 4.4, where the stress-strain curve and selected WAXD and SAXS images at different strains are shown. The initial WAXD pattern showed an isotropic feature with only orthorhombic crystal reflections. When the strain was increased, the diffraction patterns shifted towards the equator, where several new reflections from the monoclinic phase also appeared. Figure 4.5 shows a 2D WAXD pattern

taken from the 0.6% IL/UHMWPE blend at strain 100%. There were five distinct diffraction peaks - two from the orthorhombic phase and three from the monoclinic phase. The values of scattering vector s for these crystal reflection peaks are listed in Table 4.2. It is known that in polyethylene, the orthorhombic phase is the most stable form, while the monoclinic phase is the metastable form. The structure of the monoclinic phase and its possible formation mechanism in oriented polyethylene has been reported by Seto et al. [25, 26]. The positions of the detected monoclinic peaks (010), (200) and $(\bar{2}10)$ in this study were nearly the same as the results from the Seto study, giving the unit cell parameters of $a = 8.09$ Å, $b = 4.79$ Å, $c = 2.53$ Å, and $\gamma = 107.9°$ (here we refer the chain-axis as the c-axis, which was different from the original literature [25, 26]). We note that the phase transformation from the orthorhombic to monoclinic phase could be induced by stress, which is often termed the martensitic transformation [26-28]. This behavior was observed in all three samples (blends and control).
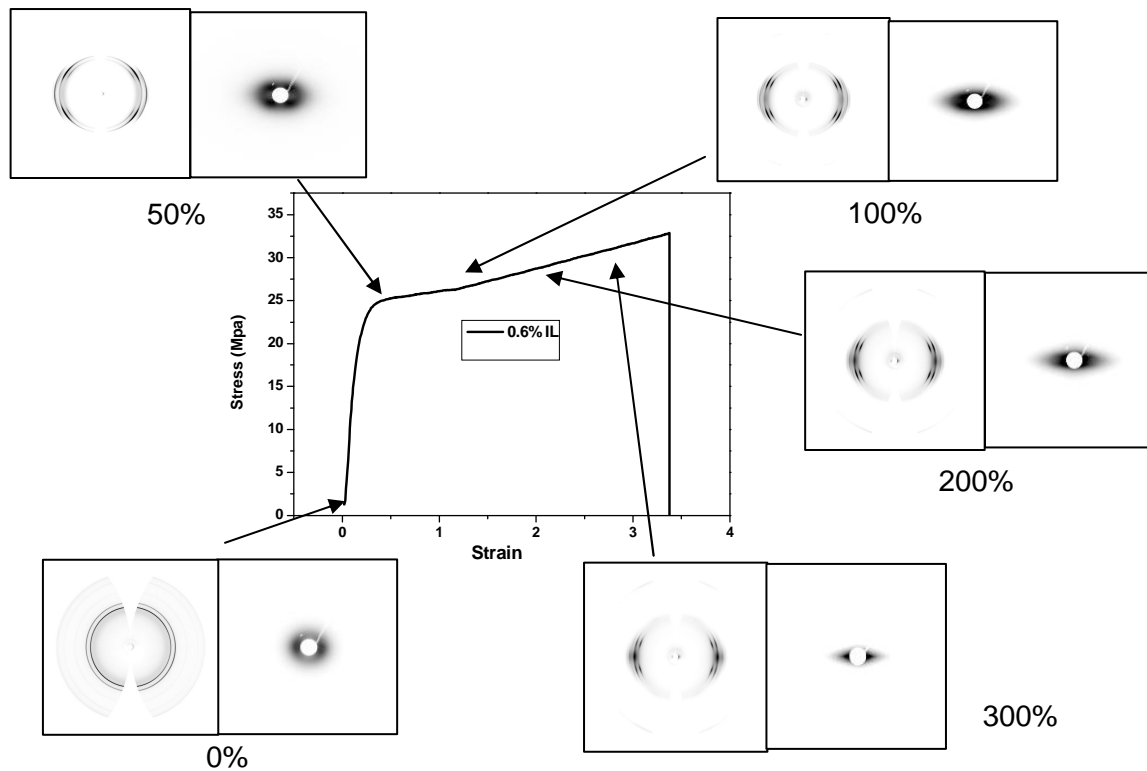
Figure 4.4 Selected WAXD and SAXS patterns for 0.6% IL/UHMWPE blend at different strains during stretching at 25 ºC.
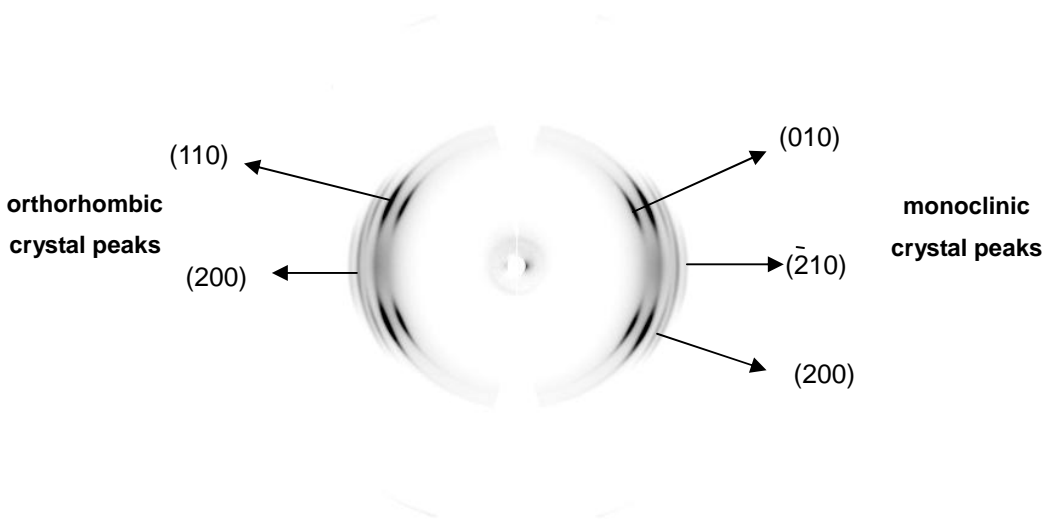
Figure 4.5 Typical WAXD pattern of 0.6% IL/UHMWPE blend at strain 100% and 25 ºC with the crystal reflection peaks from two different crystal phases.

Table 4.2 Scattering vector s of crystal reflection peaks found during stretching of the 0.6% IL/UHMWPE blend at 25 ℃.

	Orthorhombic phase		Monoclinic phase		
crystal peak	(110)	(200)	(010)	(200)	$(\overline{2}10)$
scattering vector s (nm^{-1})	0.241	0.269	0.218	0.259	0.283

In SAXS measurements, the scattering maximum was found to move toward the equator and formed a streak-like scattering pattern at high strains. This pattern (equatorial streak) could be attributed to the non-correlated fibrillar structure, either from extended and/or microvoids. The observation of equatorial scattering streak in deformed polymer film or fiber has been reported in the literature [29, 30]. If these streaks were due to single scattering entity (e.g. microvoids or crystal fibrils), the dimensions and the orientation of these scatterers could be estimated by using the method demonstrated by Ruland [31, 32]. For the current results, as the nature of the scattering streak was complex and might consist of both contributions, we decided not to focus on the SAXS streak analysis but the quantitative WAXD analysis.

Using the method mentioned earlier, the evolution of crystallinity and components of different crystal phases for UHMWPE and IL/UHMWPE blends at 25 ℃ were determined from the WAXD data, where the results are shown in Figure 4.6. It was found that the total crystallinity decreased slightly with increasing IL content (especially in the high concentration sample). This observation was consistent with the DSC results and could be explained as follows. As the ionic liquid behaved like a plasticizer for UHMWPE, it could enhance the overall

mobility of the entangled chains and increase the plasticity of the material. As a result, the presence of ionic liquid also decreased the melting point and crystallinity. A similar role of plasticizer that could increase the segmental mobility as well as the overall chain mobility and decrease the crystallinity in other semi-crystalline polymers has been reported [33,34].
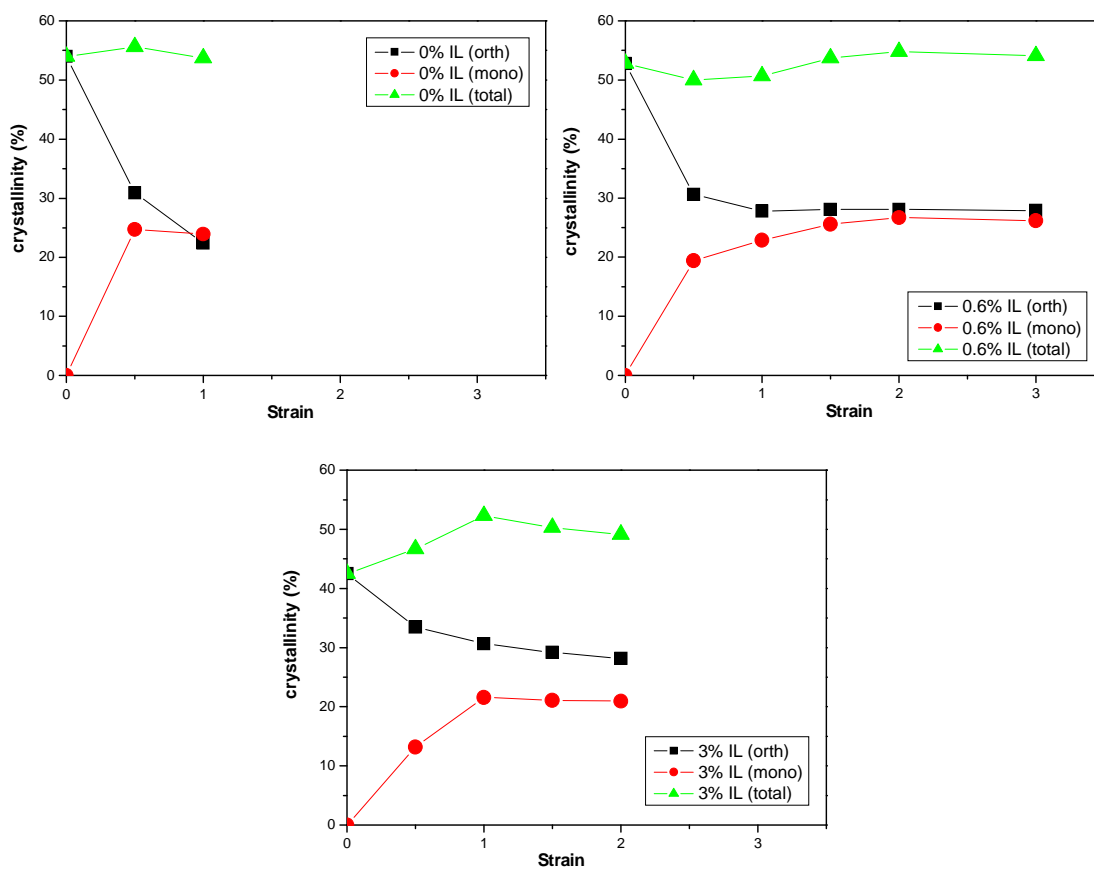
Figure 4.6 Evolution of crystallinity for UHMWPE and two IL/UHMWPE blends (0.6% and 3% IL) during stretching at 25 ℃.

As mentioned earlier, stress-induced phase transformation was seen in all three samples. The evolution process of different phases during deformation was similar, i.e., with the increase in strain, the content of the orthorhombic crystal phase decreased and that of the monoclinic

crystal phase increased. Both phases reached constant values at higher strains in the blends (this was not the case for neat UHWMPE as the material had a relatively low strain to break ratio). In the presence of ionic liquid, the phase transformation became more gradual than pure UHMWPE, implying that the time it took to reach the plateau values increased and the extent of the phase transformation decreased in the IL/UHMWPE blends. Comparing the results between pure UHMWPE and 3% IL/UHMWPE, the blend sample showed a much smaller decrease in the crystallinity by stretching (from 42.5% to 28.2%) than that in pure UHMWPE (from 54.0% to 22.4%). The addition of ionic liquid clearly delayed the stress-induced phase transformation in UHMWPE, i.e., in the presence of ionic liquid, the stress-induced melting behavior was retarded, while the enhancement in the overall chain mobility led to further crystallization at a relatively low strain (as seen in the 3% IL/UHMWPE blend).

The WAXD results were analyzed to determine the crystal orientation. Upon stretching, both (110) reflection from the orthorhombic phase and (010) reflection from the monoclinic phase showed some interesting changes in orientation. First, both reflections exhibited a four-point pattern along the off-axis, and converted to a two-point pattern on the equator at higher strains. At some strain the two features co-existed, indicating the presence of two populations for crystal orientation under deformation [35, 36]. With the increase in strain, the intensity of the four-point pattern decreased and the intensity of the two-point pattern increased. The appearance of the four-point pattern for the (110) reflection indicated that the crystallographic *a*-axis was preferentially oriented (i.e., perpendicular to the stretching direction) at low strains. At higher strains, the chain axis (i.e., the *c*-axis) became aligned with the

stretching direction, forming the two-point pattern on the equator. The change in crystal orientation did not occur in a step transformation manner with the strain, rather it occurred very gradually. During stretching, the co-existence of the two orientation populations was clearly detected from the six-point pattern in the WAXD profile at 200% strain in Figure 4.4. The change of crystal orientation in the (010) reflection of the monoclinic phase was very similar to that in the (110) reflection of the orthorhombic phase.

The change of crystal orientation could be described quantitatively by the Hermans' orientation parameter (f). Using the stretching direction as the reference axis, the parameter f can be defined as,

$$f = \frac{3 < \cos^2 \phi_{hkl,z} > -1}{2}, \text{ where } < \cos^2 \phi_{hkl,z} > = \frac{\int_0^{\pi/2} I(\phi) \cos^2 \phi \sin \phi d\phi}{\int_0^{\pi/2} I(\phi) \sin \phi d\phi}$$

The f value represents the extent of the crystal orientation, with 0 being completely random and 1 being completely oriented along the reference axis. Since no pure reflection was found in the c-axis, the Wilchinsky method [37] was used to determine the c-axis orientation by combining the information from the (200) and (110) reflections of the orthorhombic phase. For the monoclinic phase, three different reflections (010), (200) and ($\bar{2}10$) were used to estimate the orientation parameter along the c-axis. The results indicated that Hermans' orientation parameters (f) obtained from the two crystal phases were in fact quite similar. Figure 4.7 shows the evolution of Hermans' orientation parameter with strain obtained from the orthorhombic phase. The initial f value was found to be around 0.1 to 0.2, which was not completely random. This could be attributed to the melt-pressing process during sample preparation. For pure

UHMWPE, the *f* value did not change much until after the strain of 50%. Whereas the *f* values of the two IL/UHMWPE blends increased steadily and reached a plateau value after the strain of 150% (both blends exhibited the same trend). Overall, the IL/UHMWPE blend showed higher crystal orientation compared with that of pure UHMWPE. This result was consistent with the earlier observation, i.e., the ionic liquid could increase the overall chain mobility in UHMWPE and facilitate the change of crystal orientation.

Figure 4.7 Evolution of Hermans' orientation parameter along the *c*-axis for UHMWPE and two IL/UHMWPE blends (0.6% and 3% IL) at 25 ℃.

The combined X-ray/stretching test was also carried out at a higher temperature (i.e., 120 ℃), with the corresponding stress-strain curves being shown in Figure 4.8. The yield points were clearly seen in the high temperature deformation of these three samples. Due to the increasing overall chain mobility at higher temperatures, a larger elongation-to-break ratio was obtained

when compared with that at room temperature. However, both IL/UHMWPE blends still exhibited larger elongation-to-break ratios than pure UHMWPE. The 0.6% IL/UHMWPE blend exhibited better elongation-to-break performance than the 3% IL/UHMWPE blend. The tensile strength of the blend also increased significantly when compared with that of pure UHMWPE, especially for the 0.6% IL/UHMWPE blend.
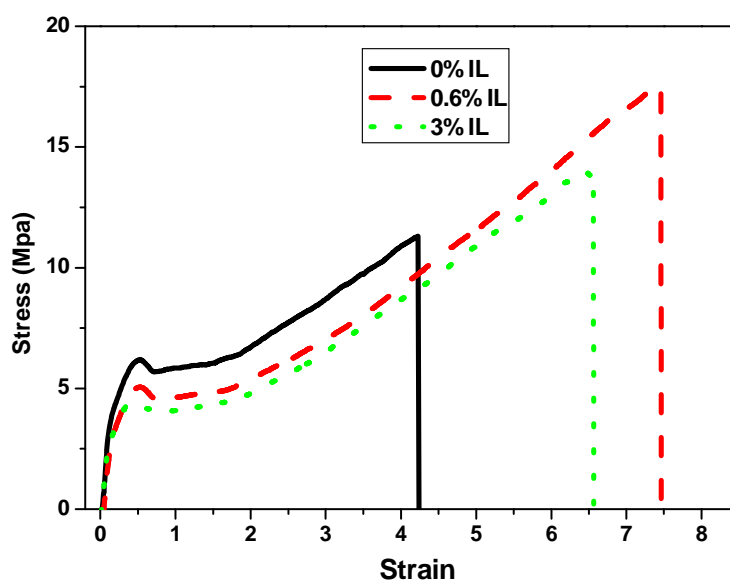
Figure 4.8 Stress-strain curves of UHMWPE and two IL/UHMWPE blends (0.6% and 3% IL) at 120 ℃.

Selected WAXD and SAXS images of the 0.6% IL/UHMWPE blend at different strains are shown in Figure 4.9. In WAXD patterns, all diffraction peaks were found to move towards the equatorial direction with increasing strain, and they eventually exhibited a two-point pattern on the equator, indicating a very high crystal orientation. However, no phase transformation was observed during stretching at 120 ℃, unlike the deformation study at room temperature. The

corresponding SAXS results showed some interesting cross-streak patterns at high strains, indicating the formation of ordered structure in large scale. The detail of this structure will be discussed later.
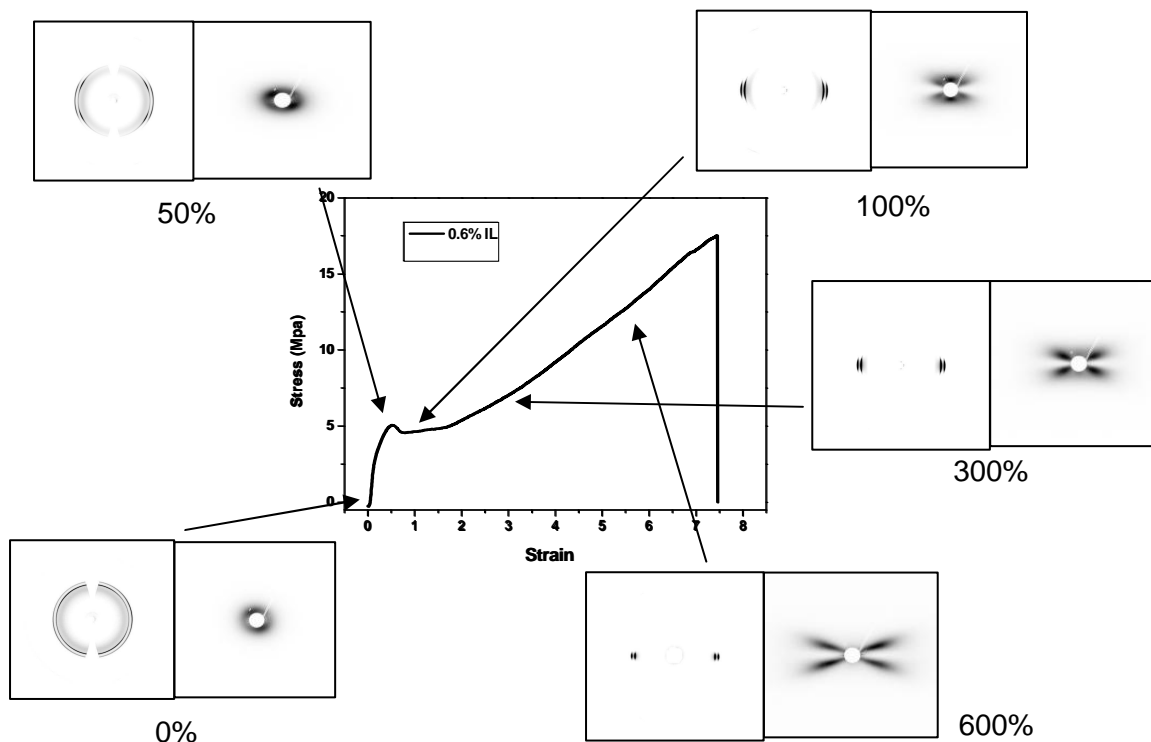
Figure 4.9 Selected WAXD and SAXS patterns for 0.6% IL/UHMWPE blend at different strains during stretching at 120 ºC.

The change in crystallinity during stretching at 120 ^{o}C was calculated, with the results being illustrated in Figure 4.10. Since no phase transformation was observed in these samples, only the total crystallinity was estimated. It was found that the total crystallinity decreased with increasing IL content. However, the trends of the change in the three samples were similar, i.e., the crystallinity increased at low strains and reached a plateau value at higher strains. At room temperature, stretching led to the destruction of the orthorhombic phase and formation of the monoclinic crystal, whereas at high temperatures, stretching resulted in an increase in the

orthorhombic phase. Clearly, the mechanisms of the stretch-induced structure changed at low and high temperatures were very different.
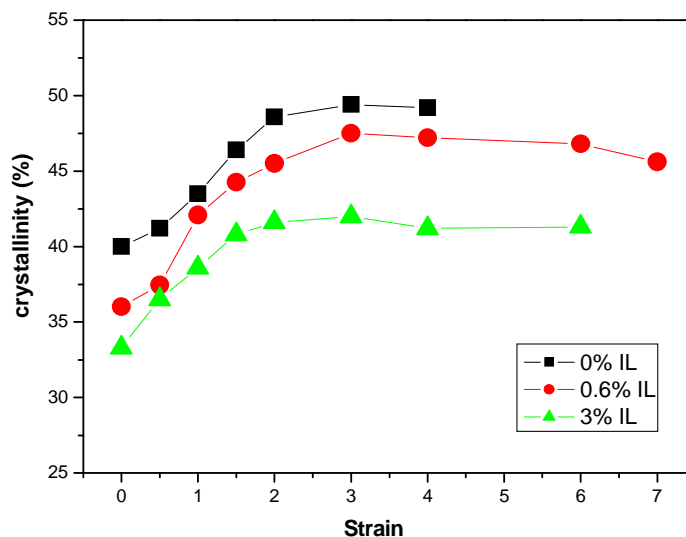
Figure 4.10 Evolution of crystallinity for UHMWPE and two IL/UHMWPE blends (0.6% and 3% IL) during stretching at 120 ºC.

During deformation at high temperatures, the four-point pattern of (110) reflection was observed only at low strains (below 100%). At higher strains, the sharp two-point pattern appeared in the equatorial direction indicating the formation of *c*-axis orientation along the stretching direction. This was quite reasonable since the high mobility of polymer chains at high temperatures made it easy for the chain axis to align along the stretching direction; while at low temperatures, the *a*-axis orientation was more favorable in the initial drawing stage than the *c*-axis orientation. Hermans' orientation parameters at different strains were calculated and the results are shown in Figure 4.11. The blend samples showed better orientation than pure UHMWPE. For example, the *f* value was 0.91 at the end point of the 0.6% IL/UHMWPE blend,

indicating the achievement of a very high crystal orientation at the end of stretching. In general, the three samples showed a similar trend in the change of Hermans' orientation parameters, i.e., the f value increased rapidly in the low strain range (strain < 100%) and then slowly reached a plateau value. This behavior was similar to the crystallinity change observed in Figure 4.10. However, such a comparison was quite different from the results at room temperature, i.e., the crystal orientation increased steadily throughout the stretching process (as seen in Figure 4.7).
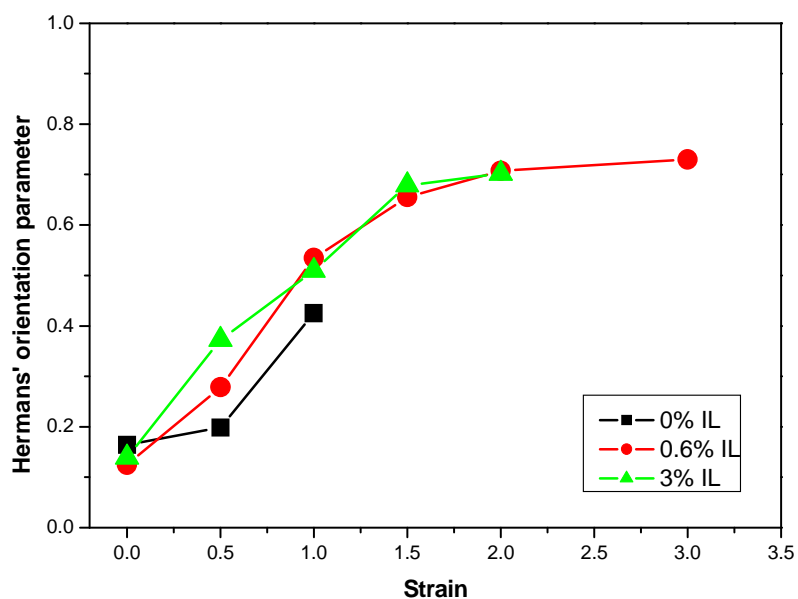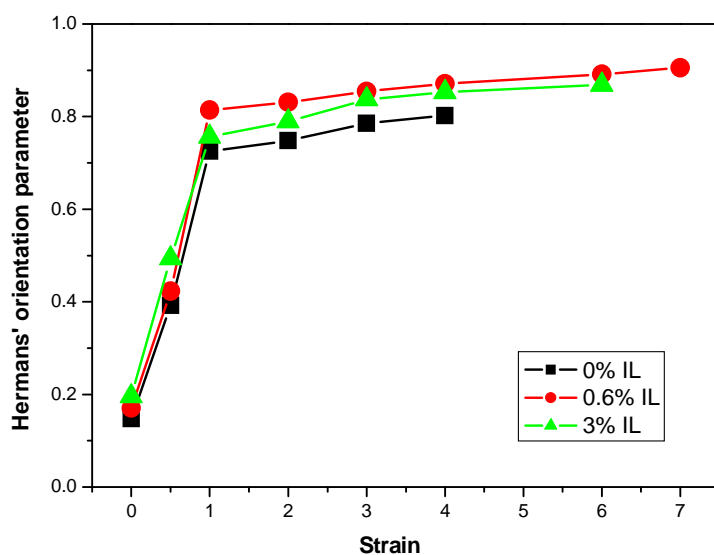

Figure 4.11 Evolution of Hermans' orientation parameter in the c-axis for UHMWPE and two IL/UHMWPE blends (0.6% and 3% IL) at 120 ℃.

To understand the structure change under different stretching conditions, WAXD patterns of the 0.6% IL/UHMWPE blend collected at different strains were further separated into oriented and unoriented components for both crystal and amorphous phases using the Halo method mentioned earlier. Figure 4.12(A) and 4.12(B) illustrate the evolution of mass fractions for

crystal (further separated into oriented and unoriented crystal), oriented amorphous (or mesomorphic as labeled in the figures) and amorphous phases during stretching at 25 ℃ and 120 ℃, respectively. At room temperature, the crystal fraction exhibited a small increase at large strain, but the increase in the oriented crystal fraction was continuous and prominent. In addition, the mesomorphic fraction was found to increase with strain, but both unoriented crystal and amorphous fractions decreased continuously. Overall, the general trends of the above changes at 120 ℃ were similar to those at room temperature. However, there were two notable differences between the results from two temperatures (25 ℃ and 120 ℃): (1) the unoriented crystal fraction at 120 ^{o}C decreased rapidly to a negligible value (fraction ~ 0) at strain 100%, whereas the unoriented crystal fraction at room temperature maintained a finite value at high strains; (2) the mesomorphic fraction (~ 35% at strain 600%) at 120 ^{o}C in the large strain region was higher than that (~22% at strain 300%) at room temperature. These observations could be understood by the mobility enhancement of the amorphous chain in the interlamellar region, i.e., with the higher chain mobility (at 120 ^{o}C), it was relatively easier to realign the crystal phase, resulting in a very rapid decrease in the unoriented crystal fraction.
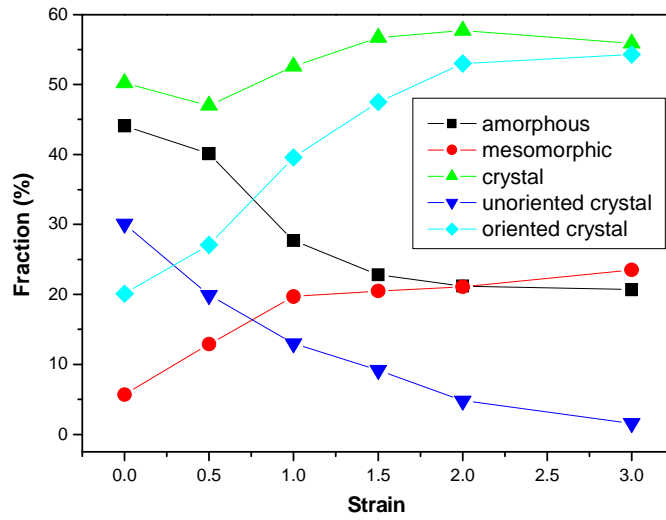
(A)
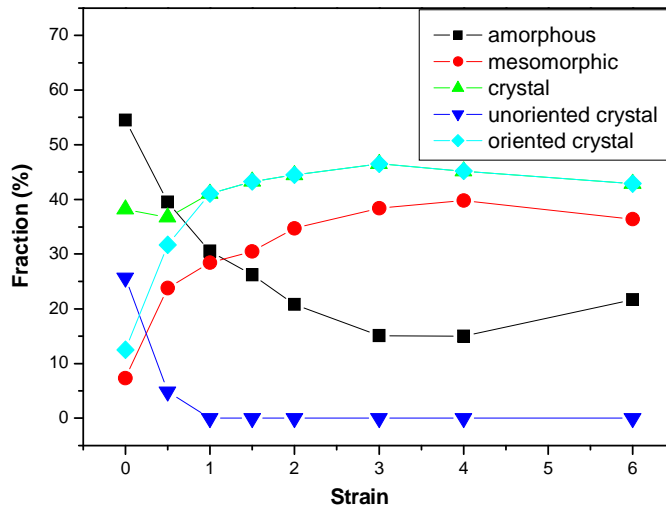
(B)

Figure 4.12 Evolution of mass fractions of oriented and unoriented components in the 0.6% IL/UHMWPE blend during stretching at 25 °C (A) and 120 °C (B).

During the deformation of pure UHMWPE at 120 °C, a cross pattern in SAXS at high strains range, which was very different from the result at room temperature, was observed. The cross pattern feature was much more distinct in the IL/UHMWPE blend. Figure 4.13 shows selected SAXS patterns for the 0.6% IL/UHMWPE blend collected at different strains. At strain 100%, the SAXS pattern, in fact, possessed two components. One was the scattering streak along the meridian; the other was the typical cross pattern. Both patterns exhibited weak scattering maxima indicating the presence of two lamellar structures. The feature of two scattering components became much clearer at strain 150%. However, at strain 300%, only the cross pattern was observed. In the previous literature, the appearance of two-point and four-point patterns have also been reported [38, 39]. The scattering pattern observed in this study exhibited more streak-like feature instead of point-like feature, indicating a broader distribution of the lamellar long spacing. The appearance of meridional scattering streak indicated the presence of the lamellar structure aligned perpendicular to the stretch axis, while the cross pattern indicated the presence of another lamellar structure aligned with a tilt angle with respect to the stretch axis. From the WAXD results, especially the evolution of the Hermans orientation parameter, it was reasonable to argue that most of the amorphous chains in the interlamellar region tended to orient along the stretching direction in the beginning of the stretching process (i.e., strain less than 100%). As a result, the lamellar axis became perpendicular to the stretch direction. At strain above 100%, fragmentation of some crystals might occur, releasing the local stress and resulting in the tilting of the lamellar structure. From the geometry of the cross pattern, it was found that the tilt angle (relative to the original lamellae that were perpendicular to the stretching direction)

increased with increasing strain. The schematic diagram of the two types of lamellae present during stretching is shown in Figure 4.14. Such tilted lamellar structure has been reported before [38,39], where the tilting angle as well as the long period value or the average distance between adjacent lamellae (along the lamellar normal) could be estimated by the position of the scattering maximum. The long period change as a function of strain is shown in Figure 4.15. The long period decreased with increasing strain. Comparing the three samples, the addition of ionic liquid was found to decrease the long spacing as well as the rate of decrease by strain, implying that the presence of ionic liquid could increase the overall mobility of amorphous chains in the interlamellar region and thereby would retard the shearing motion between the adjacent lamellae, leading to a smaller decrease in the long period but an increase in the elongation-to-break ratio. At high temperatures, the fraction of oriented crystals was primarily induced at low strains (Figure 4.12B), while the resulting lamellae orientation occurred continuously at high strains; at room temperature, the fraction of oriented crystals was completed at much higher strains (Figure 4.12A).

| 0% | 70% | 100% | 150% | 300% | 600% |
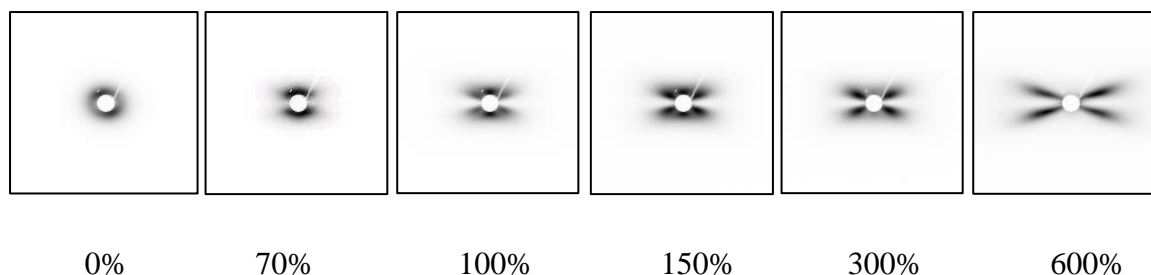
Figure 4.13 SAXS profiles of 0.6% IL/UHMWPE at different strains stretched at 120 °C.
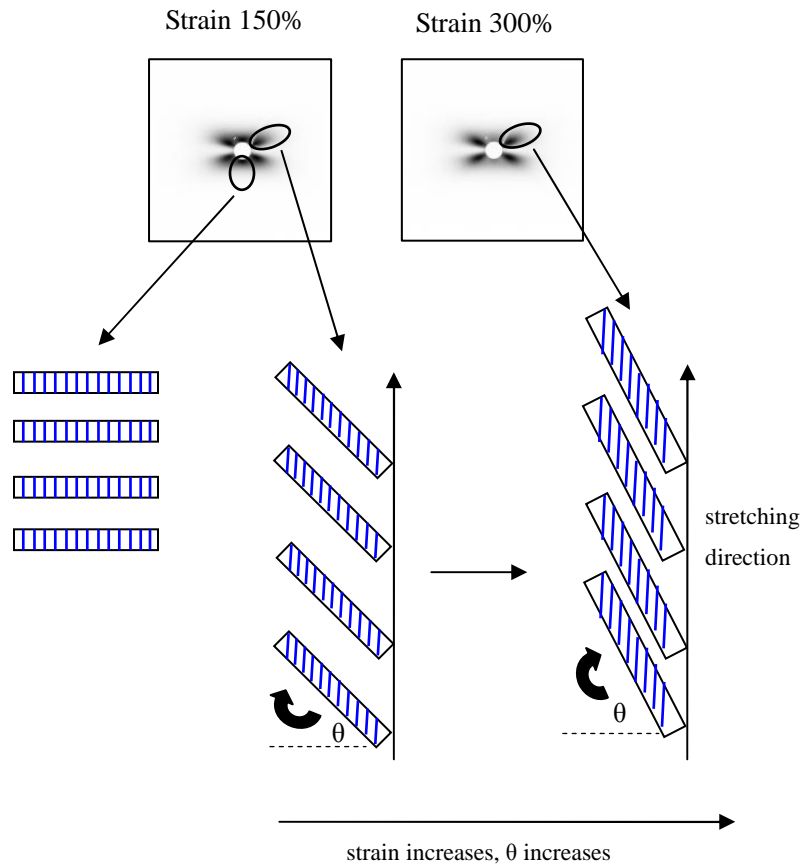
Figure 4.14 Schematic diagrams for two populations of lamellar structures during stretching at 120 °C

Ionic liquid/UHMWPE blends showed an increased elongation-to-break ratio at both temperatures, as caused by the plasticization effect of the ionic liquid. The hydrocarbon chains at the end of the ionic liquid might act as a solvent and interacted with the surrounding polyethylene chains, which could increase the overall chain mobility during the stretching process. Although ionic liquid/UHMWPE blends showed improved toughness when compared with pure UHMWPE, too much ionic liquid could not further improve the performance (e.g. 3% IL/UHMWPE exhibited a lower elongation-to-break ratio and smaller tensile strength compared

with 0.6% IL/UHMWPE) as too much ionic liquid would suppress the formation of crystallite region, leading to a less effective crystalline network.
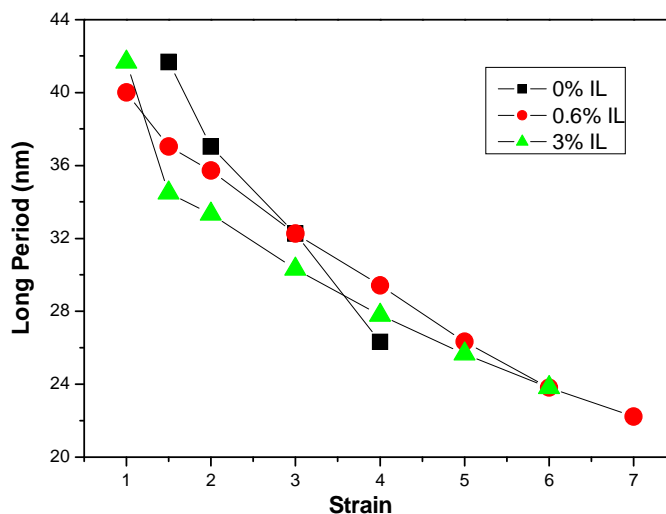
Figure 4.15 Evolution of lamellar long period at 120 ℃ for UHMWPE and two IL/UHMWPE blends (0.6% and 3% IL).

4.4 Conclusions

The addition of a small amount of ionic liquid (e.g. 0.6 %) to UHMWPE could significantly increase the elongation-to-break ratio at both low and high temperatures (e.g. 25 ℃ and 120 ℃), while maintaining comparable or better tensile strength, due to the increase in chain mobility by the plasticization effect of ionic liquid. However, too much loading of ionic liquid (e.g. 3 %) did not further improve the toughness of the UHMWPE matrix. In this study, the 3% IL/UHMWPE sample exhibited lower elongation-to-break ratio and smaller tensile strength when compared with 0.6% IL/UHMWPE at both temperatures. The structure changes induced by stretching in

the IL/UHMWPE blend and pure UHMWPE samples were quite different at the two temperatures. At low temperature, the plasticization effect of ionic liquid on the amorphous UHMWPE chains dominated the structure change, where phase transformation was observed in all three samples. The ionic liquid blend sample showed a relatively weak phase transformation when compared with pure UHMWPE, which could be attributed to the increase in chain mobility. At high temperature, all three samples exhibited higher crystal orientation than that at low temperature, where the oriented crystal fraction was completed at relatively low strains. With further increase in strain, the lamellar structure was found to tilt towards the stretching direction. The addition of ionic liquid delayed the lamellar movement under strain.

References

1. Welton T. Chem. Rev. 1999;99:2071-83.

2. Kubisa PJ. Polym. Sci., Part A 2005;43:4675-83.

3. Winterton NJ. Mater. Chem. 2006;16:4281-93.

4. Ueki T, Watanabe M. Macromolecules 2008;41:3739-49.

5. Wasserscheid P, Keim W. Angew. Chem., Int. Ed. 2000;39:3772-89.

6. Wilkes JS. Green Chem. 2002;4:73-80.

7. Harrisson S, Mackenzie SR, Haddleton DM. Macromolecules 2003;36:5072-5.

8. Strehmel V, Laschewsky A, Wetzel H, Görnitz E. Macromolecules 2006;39:923-30.

9. Biedroń T, Kubisa P. J Polym Sci Part A: Polym Chem 2004;42:3230-5.

10. Vygodskii YS, Lozinskaya EI, Shaplov AS, Lyssenko KA, Antipin MY, Urman YG. Polymer 2004;45:5031-45.

11. Kaar JL, Jesionowski AM, Berberich JA, Moulton V, Russell AJ. J. Am. Chem. Soc. 2003; 125:4125-31.

12. Carmichael AJ, Haddleton DM, Bona SAF, Seddon KR. Chem. Commun. 2000;1237-8.

13. Fujita K, MacFarlane DR, Forsyth M. Chem. Commun. 2005;4804-6.

14. Phillips DM, Drummy LF, Naik RR, De Long HC, Fox DM, Trulove PC, Mantz RAJ. Mater Chem. 2005;4206-14.

15. Xie HB, Li SH, Zhang SB. Green Chem. 2005;7:606-8.

16. Forsyth SA, MacFarlane DR, Thomson RJ, VonItzstein M. Chem. Commun., 2002;714-5.

17. Scott MP, Brazel CS, Benton MG, Mays JW, Holbrey JD, Rogers RD. Chem. Commun. 2002;1370-1.

18. Scott MP, Rahman M, Brazel CS. Eur. Polym. J. 2003;39:1947-53.

19. Lewandowski A, Swiderska A. Solid State Ionics, 2003;161:243-9.

20. Rahman M, Shoff HW, Brazel CS. ACS Symp. Ser., 2005;913:913.

21. Chu B, Hsiao BS, Ma HY, Taniguchi N. PCT patent. WO/2009/108236

22. Wunderlich B, Cormier CM. J. Polym. Sci., Polym. PartA-2 1967;5:987-91.

23. Fraser RDB, Macrae TP, Miller A, Rowlands RJ. J Appl Crystallogr 1976;9:81-94.

24. Ran S, Zong X, Fang D, Hsiao BS, Chu B, Ross R. J Appl Crystallogr 2000;33:1031-6.

25. Tanaka K, Seto T, Hara T. J. Phys. Soc. Japan 1962;17:873-4.

26. Seto T, Hara T, Tanaka K. Japan J. Appl. Phys. 1968;7:31

27. Butler MF, Donald AM, Bras W, Mant GR, Derbyshire GE, Ryan AJ. Macromolecules 1995;28:6383-93.

28. Russell KE, Hunter BK, Heyding RD. Polymer 1997;38:1409-14.

29. Grubb DT, Prasad K. Macromolecules. 1992;25:4575-82.

30. Butler MF, Donald AM, Ryan AJ. Polymer 1998;39:39-52.

31. Ruland, W. J. Polym. Sci., Part C 1969;28:143-51.

32. Perret R, Ruland W. J. Appl. Cryst. 1969;2:209-18.

33. Jang J, Lee DK. Polymer 2003;44:8139-46,

34. Wypych G. Handbook of Plasticizers. ChemTec Publishing, 2004.

35. Aggarwal SL, Tilley GP, Sweeting OJJ. Polym. Sci.1961;51:551-68.

36. Chen XM, Yoon KW, Burger C, Sics I, Fang DF, Hsiao BS, Chu B. Macromolecules 2005;38:3883-93.

37. Wilchinsky ZW. J Appl Phys 1960;31:1969-72.

38. Kaji K, Mochizuki T, Akiyama A, Hosemann R, J. Matls. Sci. 1978;13:972-84.

39. Song HH, Argon AS, Cohen RE Macromolecules 1990;23:870-6.

Chapter 5. Effect of Comonomer Content on Structure and Property Relationship of Propylene-1-Octene Copolymer during Uniaxial Stretching

5.1 Introduction

Polypropylene (PP) is one of the most important polymers in chemical industry due to its low cost and broad applications. It has excellent chemical resistance, good mechanical properties and is relatively easy to process. Polypropylene chains also have excellent ability to crystallize and can form different crystal structures. However, the different crystal structure has different effects on final properties. Although polypropylene has widespread usages, it still has limitations for certain applications, due to its weak impact strength at low temperatures and poor elastic performance. Scientists have been interested in synthesizing new polypropylene-based materials with modified structures and improved properties to overcome these limitations.

Thermoplastic elastomers (TPE) are a new kind of materials that have gained significant interest as they contain both thermoplastic and elastomeric characteristics. These materials possess improved elastic properties over conventional plastic materials and can be processed easier than traditional rubber products. There are several pathways to produce new TPF materials. One is through the processing route by mechanical mixing of conventional plastic materials

(such as PP) with elastomers, such as ethylene-propylene rubber (EPR) [1-3], ethylene-propylene-diene rubber (EPDM) [4-6] and ethylene-octene copolymer (EOC) [7-10]. Another route is by polymerization, such as copolymerization of polyolefin containing different comonomer type and content, to produce new propylene- or ethylene-based materials. The development of metallocene catalysts has greatly facilitated this method, where incorporation of varying comonomers can be controlled in a random or blocky fashion [11, 12]. For example, the propylene-based random copolymer family, containing hexene, butylene, ethylene and octene comonomer units have recently been synthesized [13-23]. With certain copolymer compositions the materials exhibited both plastic and elastic characteristics having good mechanical strength as well as decent elasticity. The versatile tuning conditions during synthesis clearly provide a new pathway to tailor the final properties. As the propylene segment is the only crystallizable component, the type and content of different comonomer greatly influence the crystalline morphology and thermodynamic properties. Furthermore, the interactions among different segments also lead to phase separation which yields hierarchical structures at different length scales [9, 24].

The purpose of the present study is to further understand the relationships between comonomer composition, structure and mechanism property of polyolefin random copolymers. To be specific, propylene-octene (PP-O) random copolymers at different octene contents (molecular ratio of 5%, 8% and 10%) were chosen as a model copolymer system to investigate the influence of comonomer on the structural change of propylene during tensile deformation and its relationship with the mechanical performance. *In-situ* wide-angle X-ray diffraction

(WAXD) and small-angle X-ray scattering (SAXS) were used to monitor the structural changes during deformation. The scattering and diffraction results have provided useful structural information at different length scales from crystal unit cells to lamellae.

5.2 Experiment

5.2.1 Materials and Preparation

Propylene-octene (PP-O) random copolymer samples were obtained from ExxonMobil Chemical Company. They were synthesized using a solution polymerization method based on the metallocene catalyst. Three different copolymer samples having octene comonomer mole percentages of 5%, 8% and 10% (i.e., weight percentages of 12%, 19% and 23%) were prepared. The weight-average molecular weights of these three copolymers were 115K g/mol, 132K g/mol and 105K g/mol, respectively. They were denoted as PP-O-5, PP-O-8 and PP-O-10 in this paper hereafter.

5.2.2 Simultaneous X-ray and Deformation Measurements

Tensile deformation measurements were performed on a modified Instron 4442 tensile apparatus, which allowed the film sample to be uniaxially and symmetrically stretched. The symmetrical deformation ensured the focused X-ray beam always illuminated on the same position of the sample during stretching. The peak melting temperatures of PP-O-5 and PP-O-8

determined by differential scanning calorimetry (DSC) were 96.3 ℃ and 83.6 ℃. For PP-O-10, the melting peak became broad, in the range of 65 ℃ to 75 ℃. So in the tensile experiment, 60 ℃ was chosen as the experiment temperature, since under this condition polymer chains had relatively high mobility in the copolymer and could make it easy to observe the different deformation behavior and larger difference on the lamella structures in these samples from X-ray scattering patterns during the stretching process.

Dumbbell-like tensile specimens were prepared by compression molding the samples at 180 ℃. All specimens were stored at room temperature for around 1 week before the tensile test in order to minimize any possible aging effects on the sample. The initial length of the specimen between the Instron clamps was 30 mm, having width and thickness of 4 mm and 1 mm, respectively. A constant crosshead speed, 6 mm/min, was applied to the specimen throughout the deformation study. The maximum strain was around 7 due to the limitation of the tensile apparatus. The step-cycle tensile test was also carried out at the chosen experiment temperature (i.e., 60 ℃). This test combined the stepwise stretching and loading-unloading cycles to evaluate the elastic recoverability of the specimen. In specific, the specimen was extended step-by-step to the desired strains of 50%, 100%, 200% and 300%, respectively. When the deformation reached the desired strain, the crosshead reversed back at the same crosshead speed until zero stress was detected. The extension was then applied again to reach the next target strain, whereby the process would repeat itself until the completion of the final cycle. The recovery ratio was calculated as $1-\left(\varepsilon_r / \varepsilon_0\right)$, where ε_r represents the residual strain and ε_0 represents the target

strain. The stress and strain reported in this study were engineering stress and engineering strain measured directly from the Instron machine.

In-situ wide-angle X-ray diffraction (WAXD) and small-angle X-ray scattering (SAXS) measurements during tensile deformation were performed at the X27C Beamline in the National Synchrotron Light Source (NSLS), Brookhaven National Laboratory (BNL). The wavelength of the synchrotron radiation was 1.371 Å. To monitor the structural changes, a charged coupled device (CCD, MAR-USA) detector was used to collect 2D scattering/diffraction patterns in real time. The CCD detector had a resolution of 1024×1024 pixels and each pixel size was 158.44 μm. The typical image acquisition time was 30 s for each frame collection. The sample-to-detector distance was 1910 mm for the SAXS setup (calibrated with silver behenate) and 121.1 mm for the WAXD setup (calibrated with Al_2O_3). All X-ray images were corrected for background scattering, air scattering and synchrotron beam fluctuations.

5.2.3 X-ray Data Analysis

Quantitative analysis was applied on all 2D WAXD patterns, which were also compensated for Fraser correction due to the distortion from the flat-detector [25]. The stretched samples were assumed to possess fiber symmetry, i.e., with cylindrical symmetry along the machine direction. This was proven to be a good approximation for this type of single axis deformation systems. WAXD patterns were integrated along the scattering vector and the integrated scattered intensity could be expressed as $I(s) = 2\pi \int_{0^o}^{180^o} I(s,\phi)s^2 \sin\phi d\phi$. In this integration, the Lorentz correction factor (s^2) was used to obtain the mass distribution of the system. The integrated intensity profile

was then de-convoluted into different crystal reflection peaks and an amorphous background using the peak fitting method. The crystallinity was determined from the ratio of the integrated area under all crystalline components to the total integrated area.

Typical SAXS image exhibited a broad meridional 2-bar pattern superimposed with an equatorial streak during stretching. The image indicated the lamellar structure under deformation, where the lamellar long period, lamellar thickness, orientation and lateral size could be estimated. The lamellar long period was obtained by the maximum scattering position in the Lorentz-corrected integrated 1D SAXS profile. Lamellar thickness, lateral size and orientation were obtained by a semi-quantitative fit of the 2D SAXS pattern, to be described below. For the stretched system, fiber symmetry was assumed in the SAXS/WAXD pattern, which was verified in our earlier studies [26-29]. This assumption greatly simplified the theoretical approach for the analysis of 2D scattering/diffraction images. The 2D WAXD analysis has been demonstrated earlier [26-29] and will not be repeated here. The 2D SAXS analysis for the system with preferred orientation was adopted [30]. The principle is briefly described as follows. Figure 5.1 illustrates the spherical trigonometric relationship of the scattering system with preferred orientation in reciprocal space [26, 31]. In this case, the scattered intensity J (s, φ) can be expressed as [26, 31, 32]:

$$J(s,\varphi) = \int_0^{\pi/2} I(s,\varphi')F(\varphi,\varphi')\sin\varphi' d\varphi'$$

where φ is the polar angle with respect to the principal axis of the fiber, φ' is the polar angle in the coordinate system of the structural unit I (s, φ') and F (φ, φ') is the integral kernel correlated with the orientation distribution function (ODF) $g(\beta)$. In our approach, the Onsager orientation

distribution function was used as the ODF with the following expression [29]:

$$g_O(\beta) = p\cosh(p\cos\beta)/\sinh(p)$$

where β is the angle between primary axis of J $(s,\ \varphi)$ and I $(s,\ \varphi')$, p is the orientation distribution parameter related to the breadth of the profile and from that Hermans' orientation parameter P_2, as given by [29]:

$$P_2 = 1 - 3p^{-1}[\coth(p) - p^{-1}]$$

Thus, the integral kernel F $(\varphi,\ \varphi')$ has the form [26, 29]:

$$F(\varphi,\varphi') = p\csc h(p)\cosh(px)I_0(py)$$

where $x = \cos\varphi\cos\varphi'$, $y = \sin\varphi\sin\varphi'$ and I_o is the modified Bessel function of the first kind at zero order.

The intensity distribution $I(s,\varphi')$ can be factorized into $I(s_{12},s_3) = I_{12}(s_{12})I_3(s_3)/2\pi s_{12}$, where $s_{12} = s\sin\varphi'$, $s_3 = s\cos\varphi'$. $I_3(s_3)$ represents the 1D scattered intensity related to the lamellar thickness and distribution. $I_{12}(s_{12})$ is related to the lamellar lateral size, which could be simulated by a Gaussian distribution,

$$I_{12}(s_{12}) = b^{-1}\exp(-\pi s_{12}^2/b^2)$$

or Lorentzian distribution,

$$I_{12}(s_{12}) = b^{-1}(1 + \pi^2 s_{12}^2/b^2)^{-1}$$

From the simulation results, the P_2 orientation and the lamellar lateral size b can be obtained. The detailed analysis will also be shown in the correlated text.
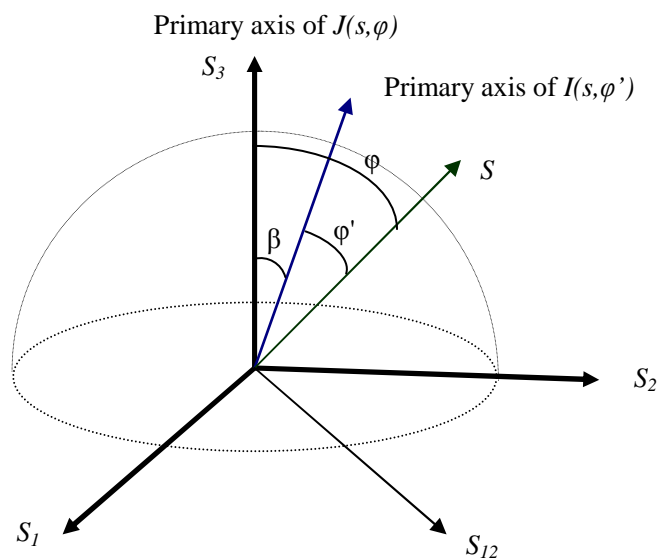
Figure 5.1 Spherical-trigonometric relationships between scattering vector *s* and primary axis of the intensity distribution of the structural unit *I (s, φ')* and the oriented ensemble *J (s, φ)*.

5.3 Results and Discussion

The stress-strain curves of propylene-octene copolymer at different octene concentrations (5%, 8% and 10%) and 60 °C are shown in Figure 5.2. The incorporation of the comonomer resulted in notable changes of mechanical properties. For example, with an increase in the octene content, the elastic modulus and tensile yield stress decreasd significantly. The tensile behavior of the PP-O-5 sample showed a typical trend of semi-crystalline polymers, exhibiting highly localized yield and neck regions. On the other hand, for PP-O-8 and PP-O-10, these samples behaved more like elastomers, especially noticeable for PP-O-10, where the neck region became diffused and mixed with the strain-hardening region at high strains.
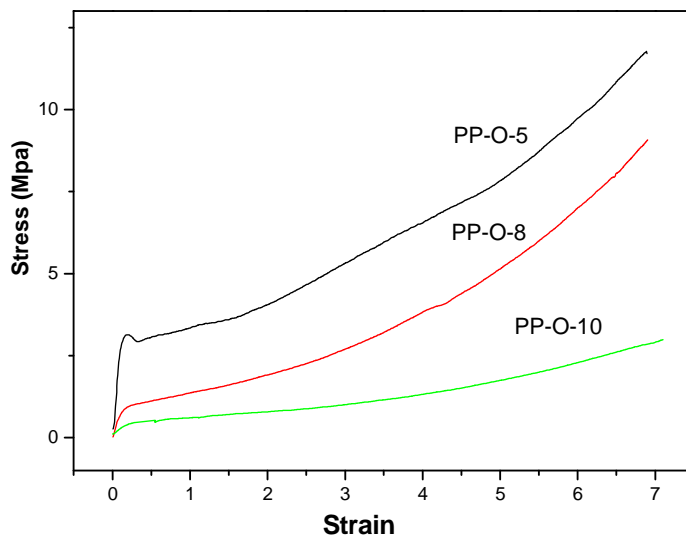
Figure 5.2 Stress-strain curves of propylene-octene copolymer with different octane concentrations (5%, 8% and 10%) at 60 ℃.

Before studying the crystal orientation change at different strains, the chosen propylene-octene copolymer samples were kept at 60 ℃ for a long enough time until there was no noticeable change with the stress. This process was aimed to eliminate the annealing/aging effect of the copolymers at 60 ℃, especially for high octene content samples. Thus, the possible aging effect was ignored during the stretching process in order to avoid the complexity when discussing the influence of stretching force on the crystal structure of copolymers. Figure 5.3 illustrates the 1D integrated WAXD patterns of the three propylene-octene copolymers before the stretching experiment. These copolymer samples exhibited several discrete diffraction peaks at scattering vector s with values of around 1.53, 1.82, 2.00, and 2.34 nm^{-1}. The peaks matched the characteristic diffraction from the α-phase crystal form of iPP homopolymer and they could

be indexed as (110), (040), (130), and (111) reflections, respectively. Systematic studies have found that the inclusion of comonomer would induce different crystal structures. γ-phase iPP was commonly observed in the propylene-based copolymer within certain comonomer content [20, 21]. Even the new crystal phase could form in the propylene-1-hexene copolymer under certain conditions [19]. γ-phase propylene was also observed in propylene-1-butylene copolymer during stretching in our previous studies [28]. However, the characteristic diffraction peak of the γ-phase in iPP (117) at around $s = 2.25$ nm^{-1} [33, 34], was not observed here. It was found that with higher octene content, the intensity of the second diffraction peak (at around $s = 1.88$ nm^{-1}) became more intense when compared with that of the first peak. Similar behavior was reported and explained by the presence of iPP γ-phase from the (008) diffraction peak at the same s position [35]. However, as the characteristic (117) diffraction peak was not seen here, it could more likely be that the γ-phase was not formed in the copolymer or the corresponding structure possessed large defects. The crystallinity (α-phase) of these copolymers was calculated as 27%, 24% and 14% for PP-O-5%, PP-O-8% and PP-O-10%, respectively. It was reasonable to find that crystallinity was decreased with the incorporation of the non-crystallizable component.
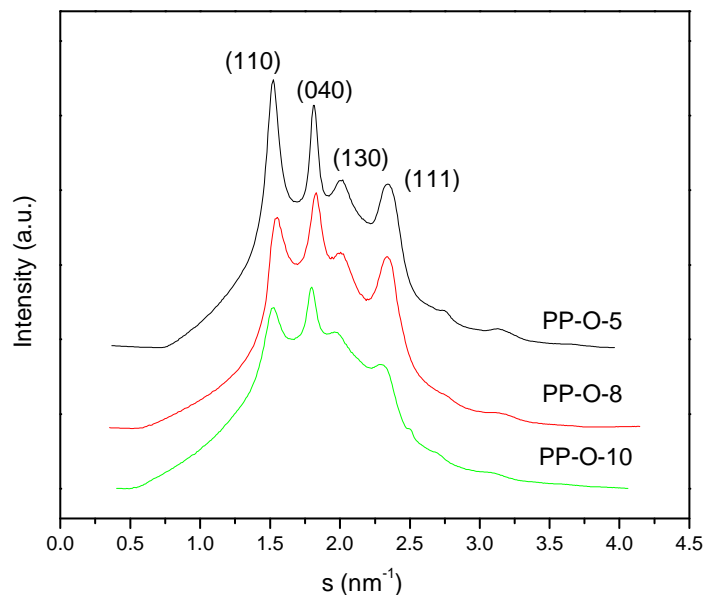
Figure 5.3 Integrated 1D WAXD profiles of PP-octene copolymer at 60 ℃ before stretching.

Figure 5.4 shows selected 2D WAXD profiles during stretching. For simplicity, only the profiles of PP-O-5 and PP-O-10 at strains of 100%, 300% and 700% are shown. Copolymers could exhibit higher crystal orientation at larger strains, and PP-O-5 showed higher crystal orientation than PP-O-10. There was no observable phase change during the stretching process and all copolymers only exhibited α-phase crystals throughout deformation. In PP-O-10 at strain of 700%, the three arcs in the equatorial direction could be assigned as the (110), (040) and (130) diffraction peaks, respectively, where the c axis was parallel to the machine direction. The weak scattering streaks in the meridian direction appeared at high strains and could be caused by the scattering of the daughter lamellae (they had a tilt angle of about 80 ° with respect to the mother lamellae) [18, 36, 37]. These meridian streaks thus could be ascribed as the (110) reflection of

the daughter lamellae, as indicated in the profiles. It was noticed that there was another streak in the meridian direction at a higher scattering angle. Considering the position and shape, this streak could be attributed to the (220) peak of the daughter lamellae, as indicated in Figure 5.4. The result could be explained as follows. During stretching, the mother lamellae bore a majority of tensile force, especially at high strains. These mother lamellae were easy to be fragmented, with the decreased size leading to the broadening of the corresponding reflection peaks, and was consistent with the experimental results in PP-O-5. In addition, the increased disorder in the mother lamellae would significantly decrease the reflection intensity, especially for those high-angle peaks; while the daughter lamellae reflection peaks would be much less influenced. As a result, the (220) peak from the daughter lamellae in the meridian direction could remain intact, while the (220) peak from the mother lamellae in the equatorial direction would become diffused and weak.
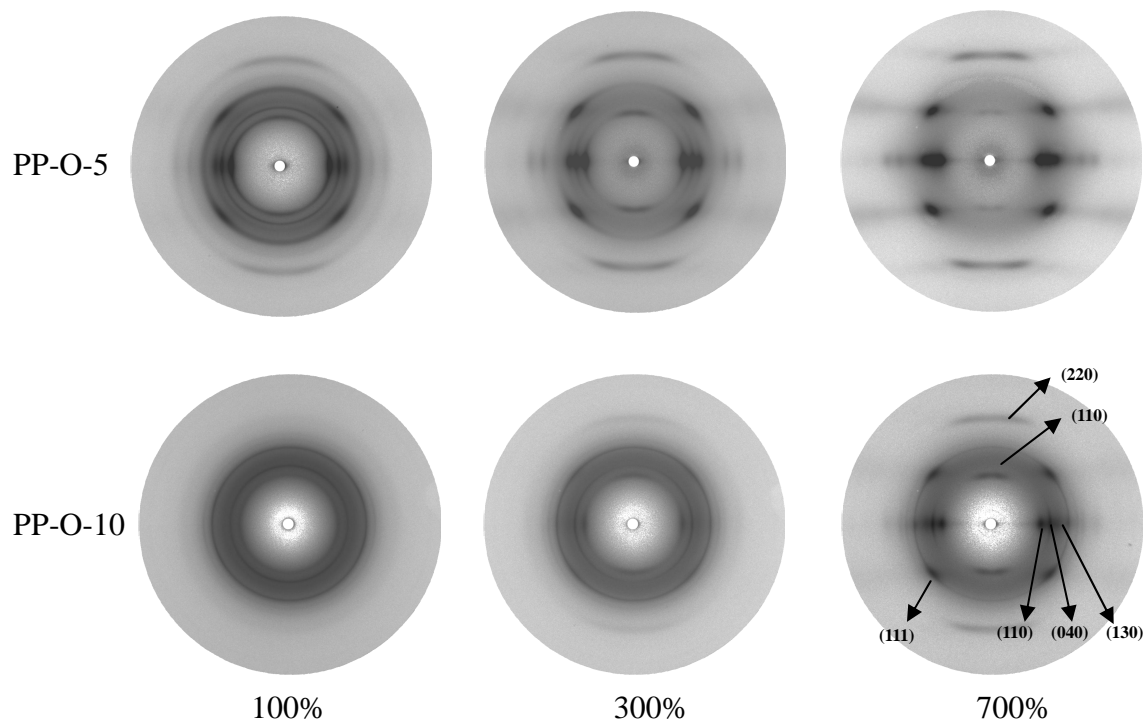
Figure 5.4 Selected 2D WAXD profiles of PP-O-5 and PP-O-10 copolymer stretched under 60 ℃ at strains 100%, 300% and 700%.

The integrated 1D WAXD profiles of PP-O-5 and PP-O-10 at different strains are plotted in Figure 5.5. With increasing strain, the scattering intensity decreased due to the reduction of the sample thickness during stretching. The positions of the reflection peaks did not change significantly with strain and no noticeable new reflection peak could be detected, confirming that the chosen copolymers possessed mainly α-phase crystals. However, at higher strains, such as 500% and 700%, the crystal peaks became very broad. In this case, the remaining polypropylene crystals possessed large defects (under high deformation) and could be in the mesomorphic phase. This mesomorphic phase was different from the amorphous phase, and it had notable orientation along the fiber direction. The evolution of crystallinity of PP-O-5, PP-O-8 and PP-O-10 under stretching was obtained by peak fitting of the integrated 1D WAXD profiles. The

results are illustrated in Figure 5.6. The crystallinity values of PP-O-5 and PP-O-8 decreased initially near the yield point, after which they increased subsequently. However, the PP-O-10 sample did not show this trend (or the yield point). This behavior may be explained as follows. The tensile force could impose two opposite effects on the change of crystal structure in semi-crystalline polymers. For one, the tensile force could elongate the polymer chains and induced new crystal formation. On the other hand, the tensile force could also destroy preexisting crystals. These opposite effects, depending on the molecule structure, temperature and type of force applied, could lead to different structural changes. For example, the PP-O-5 and PP-O-8 samples showed a decrease in crystallinity at strains below 50%, which indicated that the dominant effect of tensile force at this stage was crystal destruction. The subsequent crystallinity increase, especially for PP-O-5 indicated that the dominant effect was strain-induced crystallization. The PP-O-10 did not show the crystal destruction step, probably due to the small crystallinity and/or small crystal size in PP-O-10. This explanation was also consistent with the SAXS results, to be discussed later. At strain 700%, all copolymers showed decreased crystallinity, indicating that at high deformation, the crystal destruction again became the dominant effect.
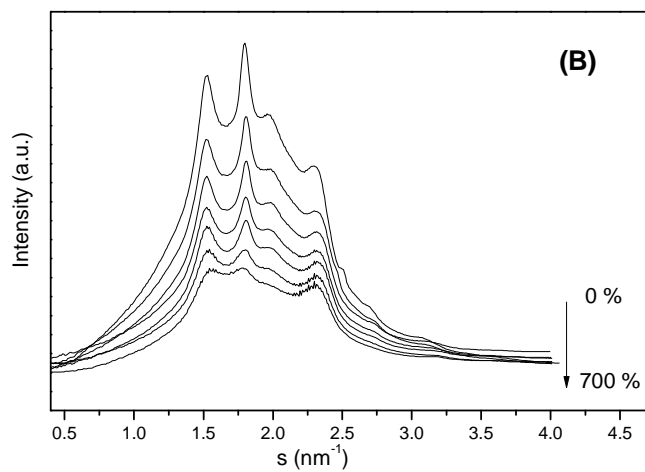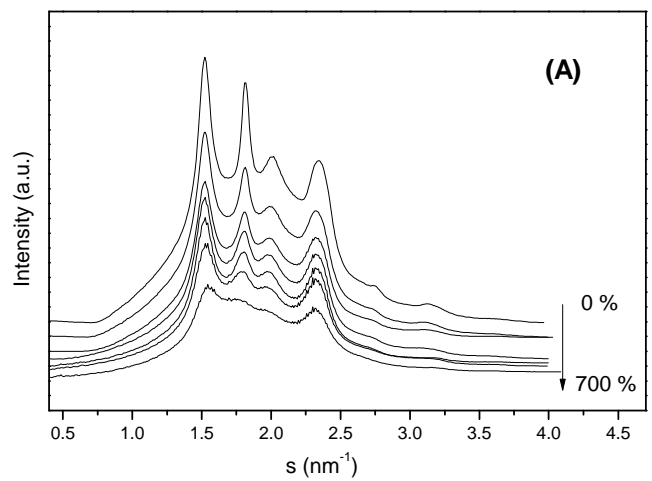
Figure 5.5 Integrated 1D WAXD profiles of PP-O-5 (A) and PP-O-10 (B) copolymers stretched at 60 ºC and strains of 0%, 50%, 100%, 200%, 300%, 500% and 700%.
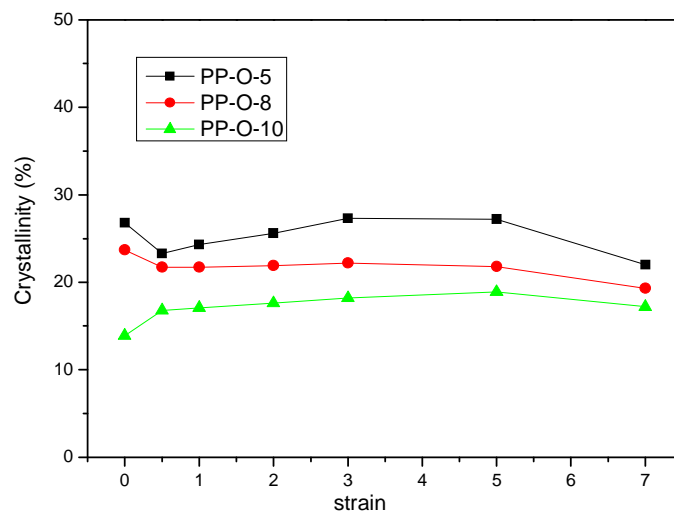
Figure 5.6 Crystallinity of PP-O-5, PP-O-8 and PP-O-10 stretched under 60 ℃ at strains of 0%, 50%, 100%, 200%, 300%, 500% and 700%.

SAXS patterns could provide useful information about the crystal structure in a larger length scale, complementary to the WAXD results, for semi-crystalline polymers. Selected 2D SAXS images of three copolymers stretched under 60 ℃ at different strains are shown in Figure 5.7. Generally, the orientation became higher upon stretching. The initial scattering pattern was isotropic, while the patterns at high strains always possessed two bar features along the meridian direction superimposed with an equatorial streak. It has been demonstrated that in some polyolefin samples stretched at certain conditions, a four-point scattering feature can appear in the off-axis direction, caused by the oblique crystal orientation [26]. However, this behavior was not seen here. In this study, the meridional scattering pattern was analyzed by using the following approach to elucidate the lamella crystal structure.
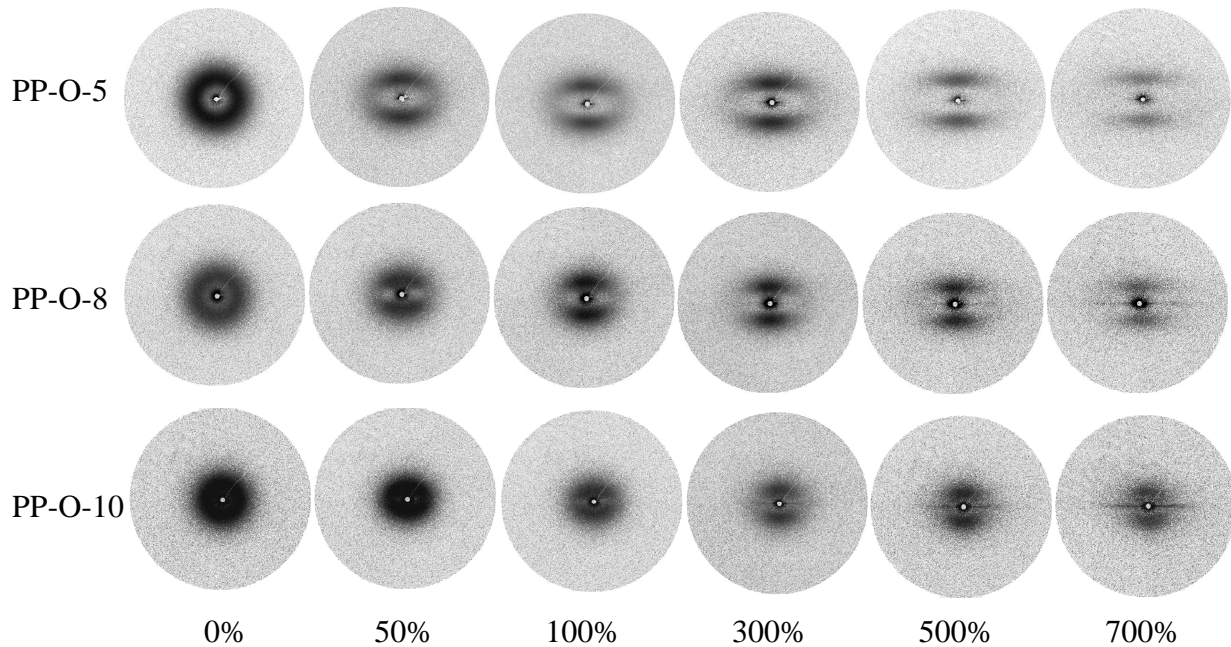
Figure 5.7 Selected 2D SAXS profiles of PP-O-5, PP-O-8 and PP-O-10 copolymer stretched at 60 ℃ and different strain.

With the assumption of fiber symmetry, the scattered intensity J (s, φ) could be calculated according to the expression in the data analysis part, in which F (φ, φ') was related to the Hermans' orientation parameter. The factorized $I_3(s_3)$ was related to lamellar thickness and distribution, and $I_{12}(s_{12})$ was related to the lateral size of lamellar disk. If the lateral dimension were infinitely large, $I_{12}(s_{12})$ became a δ function and could be ignored. In the chosen system, before stretching, the lamellar lateral size was assumed to be relatively large when compared with the lamellar thickness. Thus, the term $I_{12}(s_{12})$ could be ignored. However, with strain being increased, the lamellae were destroyed and the corresponding sizes became smaller. Thus, the lateral size effect should not be ignored.

To illustrate the effects of lamellar lateral size and lamellar orientation on the scattering patterns, several 2D SAXS patterns are shown in Figure 5.8. The simulation was made based on the variation of two parameters: lamellar lateral size b and lamellar orientation parameter p, as given earlier. Both $I_{12}(s_{12})$ and $I_3(s_3)$ intensities were calculated using a Gaussian distribution function. The scattering center was set at s = 0.1 nm^{-1}, corresponding to a length scale (i.e., long period) of 10 nm. The chosen b value of 50 nm in Figure 5.8(A) and 5.8(C) was significantly larger than the long period (10 nm). In these cases, the orientation effect dominated the scattering profile. In Figure 5.8(B) and 5.8(D), the b value of 5 nm was comparable to the long period (10 nm), where the effect of lamellar lateral size could not be ignored. The pattern 8(D) was quite different from 8(C) and resembled the PP-O-5 SAXS patterns at high strains, indicating that the PP-O-5 sample at high strain possessed high lamellar orientation but small lateral dimension.
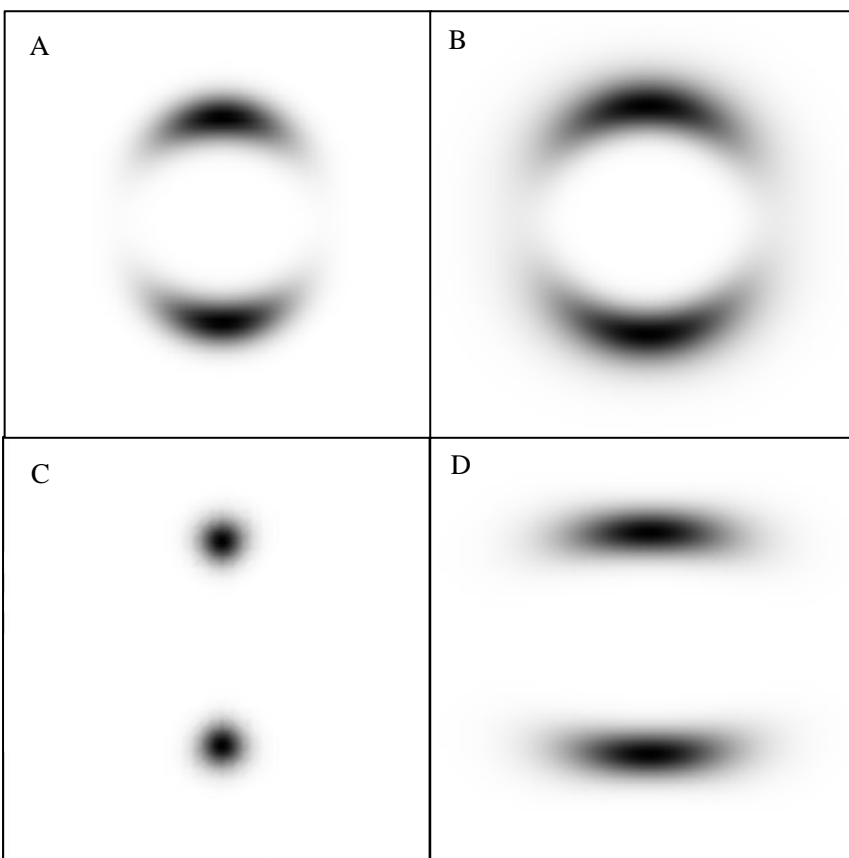
Figure 5.8 Calculated 2D SAXS patterns based on different lamellar orientation and lateral size. A ($p = 5$, $b = 50$ nm): B ($p = 5$, $b = 5$ nm): C ($p = 50$, $b = 50$ nm): D ($p = 50$, $b = 5$ nm).

From the SAXS patterns in Figure 5.7, one could conclude that at high strains, the effect of lamellar lateral size became pronounced, especially for copolymers with low octene content. However, it is not easy to separate the effects of lamellar orientation and lateral size from the scattering patterns, even though the system was assumed a lamellar two-phase model (i.e., crystal phase and amorphous phase) [38, 39], because the real system was normally polydispersed and the measured intensity profiles in the SAXS patterns were often broad and weak. In this study, a semi-quantitative method was used to deal with this problem. Profiles of the scattered intensity at three different s positions (in different polar angles) were measured from the scattering pattern. The obtained profiles were then fitted by the expression of scattered

intensity J (s, φ) shown in the data analysis part at fixed s values. The lamellar lateral size b and Hermans' orientation parameter P_2 were obtained by averaging the fitted values obtained from the three scattering profiles at different s values. Similar approach was also used in the propylene-1-butylene system recently [30]. Here it could help to quantitatively understand the lamella crystal deformation mechanism of propylene-1-octene copolymer under stretching. The typical fitting process for PP-O-8 at strain 100% is shown in Figure 5.9. The obtained lamellar lateral size $b = 9.4$ nm and the orientation parameter $p = 3.0$ corresponded to a P_2 value of 0.33.

Figure 5.10 and Figure 5.11 illustrate the fitting results of lamellar lateral size b and Hermans' orientation parameter P_2 for three propylene-octene copolymers at different strains. It should be mentioned that these results were obtained only at strains larger than 100% because the scattering patterns at lower strains did not have sufficient resolution to yield the information of lamellar lateral size. In addition, for PP-O-5 and PP-O-8 samples at strains 500% and 700%, the scattered intensities were quite weak and the profiles were narrow rectangular shaped (indicating very high lamellar orientation). In this case, the following procedures were taken. The scattering patterns were first integrated along the s_{12} direction. Assuming that Hermans' orientation parameters P_2 was 1 because of the very high orientation, the integrated profiles could be directly fitted by using a Gaussian equation to obtain the lamellar lateral size. In Figure 5.10 and 5.11, all three samples showed a general trend of decreasing in the lamellar lateral size and increasing in the P_2 value with strain, as expected. The WAXD results were also compared with the SAXS results to obtain a complete picture of the morphological and structural changes at different scales. It was interesting to find that PP-O-5 had the highest value of crystallinity (by

WAXD), which was consistent with the observation that the initial non-deformed PP-O-5 sample possessed the largest lamellar lateral size. Upon stretching, the lamellar lateral size of PP-O-5 was found to decrease rapidly, whereas the lateral size decreased gradually in PP-O-8 and PP-O-10 samples. In addition, the PP-O-5 sample exhibited the smallest crystal size at strain 700%, indicating that the behavior of strain-induced lamellar fragmentation was most pronounced in PP-O-5. However, from the WAXD results, PP-O-5 exhibited an initial drop in crystallinity around the yield point but a subsequent increase at higher strains. One possible explanation is that the stress was mainly concentrated on the crystal chains in the lamellar domain where intra-lamellar slip occurred at high strains. The continuous occurrence of lamellar fragmentation led to smaller lamellar lateral sizes. But the stretching process also induced secondary crystallization resulting in the generation of more small crystals having high orientation along the machine direction, being consistent with the orientation parameter results in Figure 5.11. With higher octene content, the lamellar orientation parameter became lower. This was also observed by the orientation evaluation of crystal reflection peak in WAXD measurements. These kinds of transformation were reported before in ethylene-1-octene copolymer system during deformation [40, 41], confirmed by using WAXD and SAXS, where similar processes were named as the transformation from lamellae crystals into the microfibrils structure.
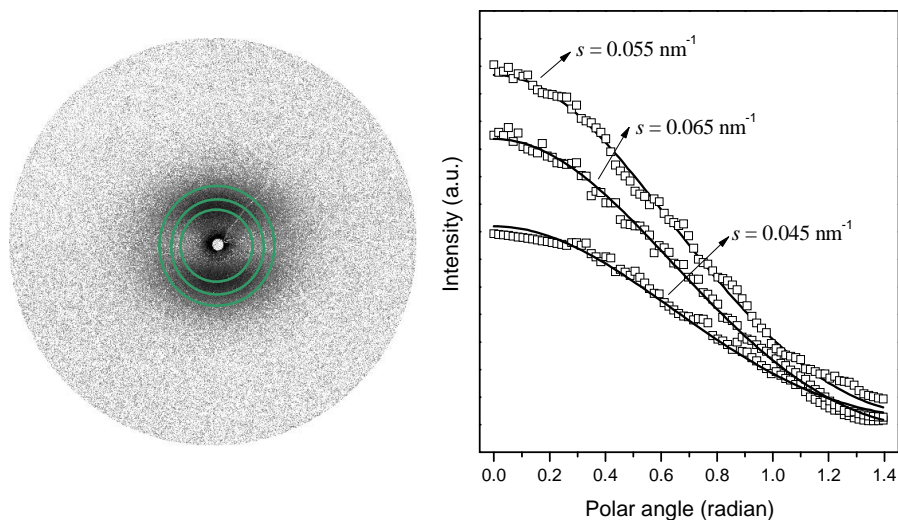
Figure 5.9 SAXS fitting of polar distributions of intensity at three different s positions for PP-O-8 at strain 100%.
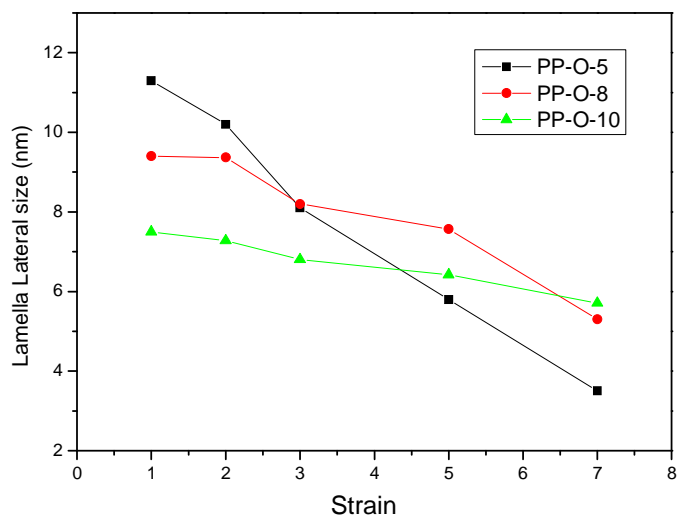
Figure 5.10 Change of lamellar lateral size as a function of strains during stretching in different propylene-octene copolymers, as estimated from SAXS patterns.
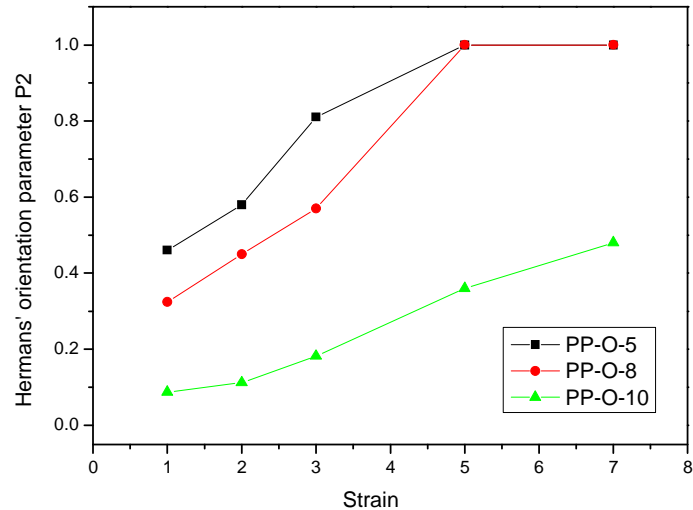
Figure 5.11 Hermans' orientation parameter of different propylene-octene copolymers at different strains during stretching as obtained from SAXS patterns.

The lamellar long period was estimated from the integrated SAXS profiles along the meridian direction and the results are shown in Figure 5.12. This long period was the sum of crystal layer thickness and amorphous layer thickness. It was interesting to note that the initial long period of PP-O-5 was around 11.5 nm, which was smaller than that of PP-O-10 (13.9 nm). However, the initial crystallinity of PP-O-5 was significantly larger than that of PP-O-10 in Figure 5.6. A reasonable explanation for this phenomenon could be that at low octene content, due to the low ordering of the crystal phase, the lamella crystals were loosely dispersed in the amorphous matrix. Thus, the amorphous layer thickness in PP-O-10 became larger when compared with PP-O-5. During stretching, the long period increased initially in all three samples with strain to the yield point. Typically, lamellar thickening or crystallization along the chain folding direction could lead to an increase in the long period. However, this could not be the case

120

here as the crystallinity of PP-O-5 and PP-O-8 all decreased, as shown in Figure 5.6. Thus, a

more likely explanation could be that the tensile force could extend the entangled chains in the

amorphous region, thus increasing the amorphous thickness and the long period. After the yield

point, the long period of both PP-O-8 and PP-O-10 samples gradually reached a plateau value,

while that of PP-O-5 decreased continuously. From the WAXD results, the crystallinity of

PP-O-5 was found to increase in this period. Based on the combined SAXS and WAXD results,

it could be that both the lamellar fragmentation (through intra-lamellar slipping) and the

strain-induced crystallization were dominant mechanisms during deformation of PP-O-5 at large

strains. In contrast, the lamellar fragmentation was not a dominant mechanism during

deformation of PP-O-8 and PP-O-10, where the long period did not change significantly at large

strains.
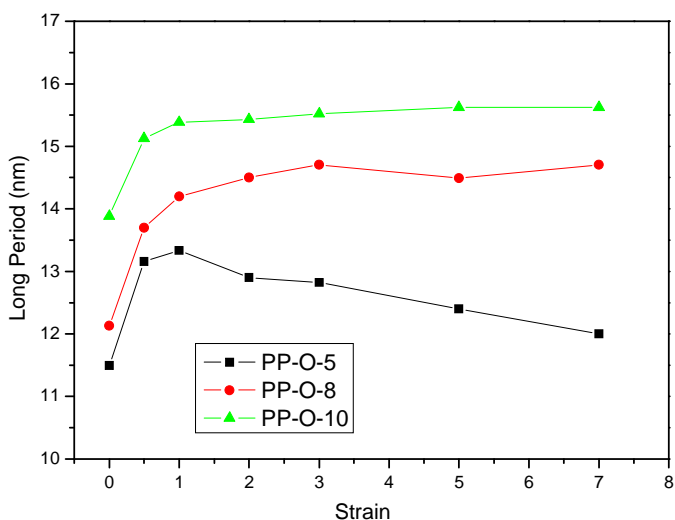
Figure 5.12 Long period distance of different propylene-octene copolymer at different strains during stretching as obtained from SAXS patterns.

In PP-O-10 and PP-O-8 samples, a notable equatorial scattering streak was observed after large strains (i.e., strain 500% for PP-O-8 and strain 300% for PP-O-10, as seen in Figure 5.7), but the appearance of the equatorial streak was not obvious in PP-O-5. The origin of these equatorial streaks in the SAXS patterns was still not entirely clear, but they clearly indicated the existence of rod-like structures along the stretching direction. One likely scenario for these rod-like structures could be that they consisted of bundles of extended-chain crystal segments (they are often termed microfibrils) superimposed with elongated microvoids [42]. The PP-O-10 sample seemed to have the highest tendency to form these structures.

It should be noted that from WAXD results, the crystal orientation parameters could be calculated by analyzing the distribution of certain reflection peaks, and the crystal size information could also be estimated through the width of the appropriate reflection peak using the Scherrer equation, which had been done quite routinely. However, the calculated crystal orientation parameter and crystal size from WAXD were quite different from the parameters (lamellar orientation parameter and lamellar lateral size) obtained from SAXS as illustrated above, partly because SAXS could detect the structure in a larger length scale (i.e., the lamellar level), whereas WAXD could detect the structure in a smaller scale (i.e., the crystal unit cell level). As the chosen semi-crystalline system could consist of crystalline lamellar structure based on mosaic small crystals [43], the SAXS results should allow us to obtain new insights into the change of lamellar structure during stretching of polyolefin copolymers. The demonstrated methodology to separate the effects of lateral lamellar size and lamellar orientation for the SAXS analysis will be particularly useful for the analysis of other similar systems.

To further evaluate the elasticity of these propylene-octene copolymers, step-cycle tensile tests were performed at strain 50%, 100%, 200% and 300% sequentially at 60 ℃. The corresponding stress-strain curves are shown in Figure 5.13. Similar to the results in Figure 5.2, the addition of octene comonomer to the propylene significantly decreased the yield stress. PP-O-5 showed a clear yield and neck region in the stretching curve for each cycle, while PP-O-8 and PP-O-10 did not and they behaved more like elastomers. To illustrate this point, the following analysis was made. The recovery ratio of different propylene-octene copolymers at different strains from the step cycle tensile testing is shown in Figure 5.14. It was seen that the propylene-octene copolymer with higher octene content showed a higher recovery ratio. PP-O-8 and PP-O-10 thus exhibited much higher elasticity compared with PP-O-5. It was interesting to note that the recovery ratio was almost above 80% for all the cycles for PP-O-10, behaving like a decent thermoplastic elastomer.
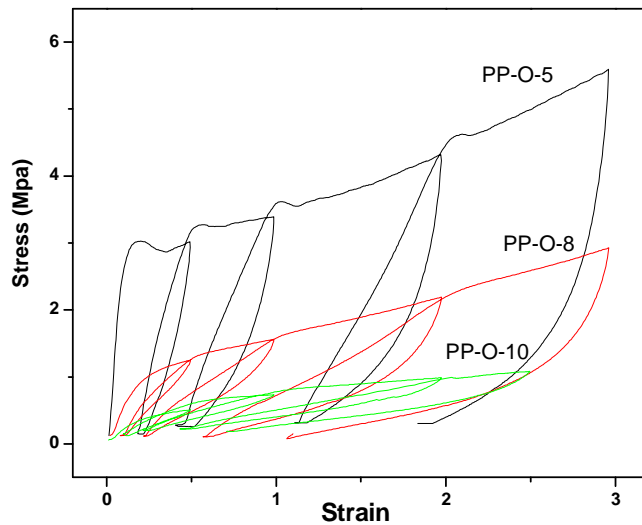
Figure 5.13 Stress-strain curves of propylene-octene copolymers during a step cycle tensile experiment at 60 ℃.
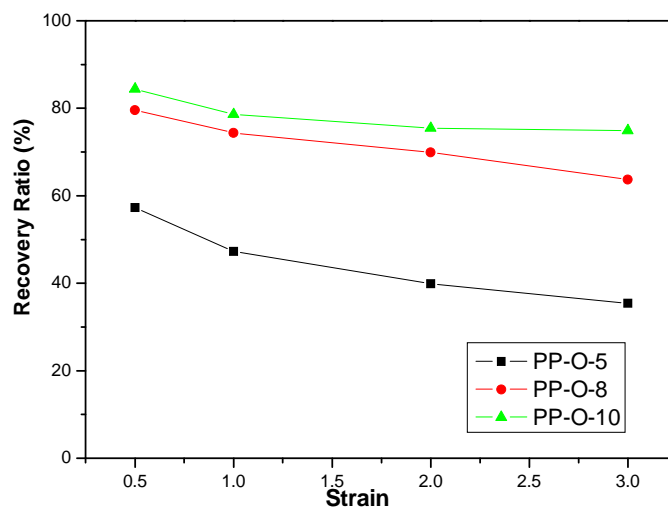
Figure 5.14 Recovery ratios of propylene-octene copolymers from step cycle tensile testing at strains 50%, 100%, 200% and 300%.

For semi-crystalline copolymers, such as polyethylene copolymer and polypropylene copolymer, previous studies showed that the addition of comonomer would have a significant influence on the change in elasticity in the system, where these materials could be classified into

different types according to their morphology, thermal behavior and crystal structure [13, 44]. In general, with the increase in comonomer content, their mechanical properties gradually changed from thermoplastic-like to elastomers-like. The results in this study are consistent with earlier findings. To be specific, the low octene content sample (PP-O-5) exhibited larger crystallinity and larger crystal size than the high octene content sample (PP-O-10). In the low octene content sample, the tensile force was probably concentrated on the lamellar crystal, resulting in a decrease in crystal size through intra-lamellar slipping or lamellar fragmentation. However, under further stretching, the strain-induced crystallization could occur, leading to an increase in crystallinity. The destruction (fragmentation) of the lamellar structure was an irreversible process as most thermoplastics, which often had higher mechanical strength but lower elasticity. For copolymer with higher octene content, the sample exhibited lower crystallinity and smaller crystal size. During the stretching process, the force was probably concentrated on the amorphous region where the lamellar structure did not change significantly. Under this condition, the amorphous chains were stretched with higher orientation that might even lead to micro-fibrillar and/or micro-void structures, while the orientation of lamellar crystal could remain lower than that in low octene content copolymer. In this system, the structure change could be reversible under certain conditions, which could be the reason why PP-O-10 had higher elasticity. Schematic illustration of lamellar fragmentation and deformation during tensile experiment is shown in Figure 5.15. In ethylene-octene or propylene-octene copolymers, if the comonomer content were high enough, the crystallizable sequence would decrease leading to smaller spherulites and thinner lamellae. It was reported that the corresponding crystal structure

could also consist of mesophase crystals or small micellar crystals [13, 45-47]. These small crystal domains could act as cross-linking points in the network structure connecting entangled polymer chains, similar to the vulcanized rubber system.
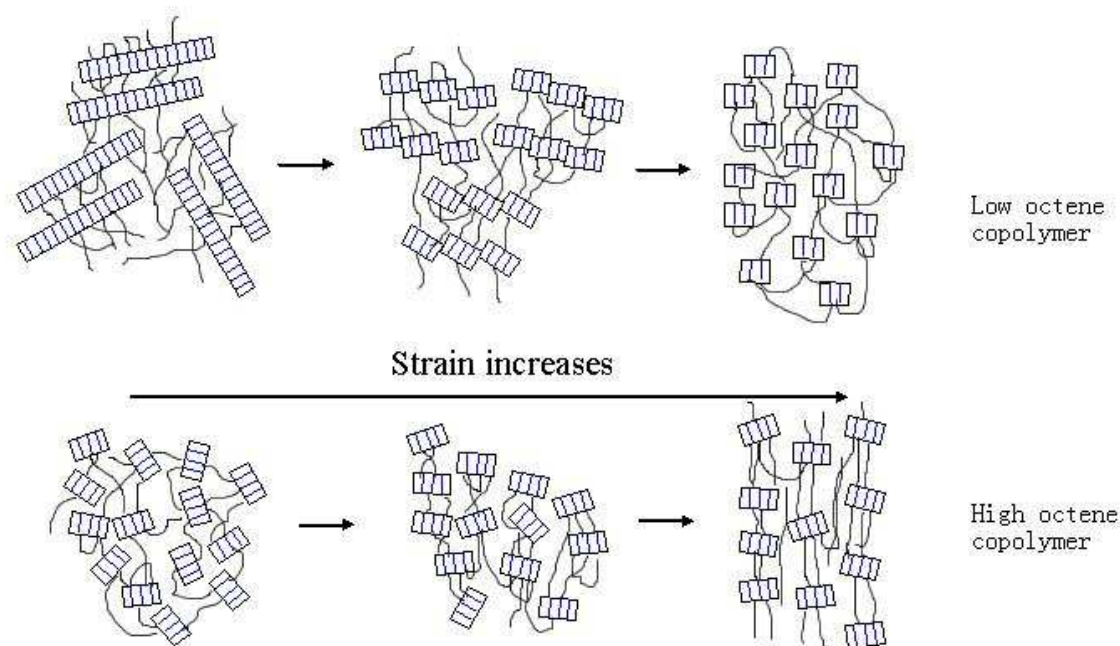
Figure 5.15 Schematic illustrations of lamellar fragmentation and deformation due to tensile deformation.

5.4 Conclusions

Propylene-octene random copolymers at different mole concentrations (i.e., 5%, 8% and 10%) were studied by *in-situ* WAXD and SAXS measurements to monitor the change of lamellar structure, orientation and crystallinity during uniaxial stretching. Copolymers with lower octene content exhibited higher crystallinity and larger crystal size. During stretching, lamellar fragmentation through intra-lamellar slipping could occur in these copolymers, leading to a

decrease in crystal sizes. The corresponding crystallinity generally decreased initially and increased subsequently at high strains due to strain-induced crystallization. The overall lamellar orientation of these materials along the stretching direction at large strains was also high. For copolymers at high octene contents, they behaved more like elastomers. Their initial crystal sizes were relatively small and they did not change substantially with strains. Upon stretching, the applied force was mainly concentrated on the amorphous regions leading to elongated microfibrillar or microvoid structures with high orientation but lower lamellar orientation. These materials also exhibited higher recovery ratio in the step-cycle tensile test.

References

1. Mighri F, Huneault MA, Ajji A, Ko GH, and Watanabe F. Journal of Applied Polymer Science 2001;82(9):2113-2127.

2. Yang D, Zhang B, Yang Y, Fang Z, Sun G, and Feng Z. Polymer Engineering & Science 1984;24(8):612-617.

3. Liang JZ and Li RKY. Journal of Applied Polymer Science 2000;77(2):409-417.

4. Öksüz M and Eroğlu M. Journal of Applied Polymer Science 2005;98(3):1445-1450.

5. Choudhary V, Varma HS, and Varma IK. Polymer 1991;32(14):2534-2540.

6. van der Wal A, Mulder JJ, Oderkerk J, and Gaymans RJ. Polymer 1998;39(26):6781-6787.

7. Lee H-y, Kim DH, and Son Y. Journal of Applied Polymer Science 2007;103(2):1133-1139.

8. Da Silva ALN, Rocha MCG, Coutinho FMB, Bretas R, and Scuracchio C. Journal of Applied Polymer Science 2000;75(5):692-704.

9. Fredrickson GH, Milner ST, and Leibler L. Macromolecules 1992;25(23):6341-6354.

10. Tang W, Tang J, Yuan H, and Jin R. Journal of Applied Polymer Science 2011;122(1):461-468.

11. Brintzinger HH, Fischer D, Mülhaupt R, Rieger B, and Waymouth RM. Angewandte Chemie International Edition in English 1995;34(11):1143-1170.

12. Busico V and Cipullo R. Progress in Polymer Science 2001;26(3):443-533.

13. Poon B, Rogunova M, Chum SP, Hiltner A, and Baer E. Journal of Polymer Science Part B: Polymer Physics 2004;42(23):4357-4370.

14. Poon B, Rogunova M, Hiltner A, Baer E, Chum SP, Galeski A, and Piorkowska E. Macromolecules 2005;38(4):1232-1243.

15. Stephens CH, Poon BC, Ansems P, Chum SP, Hiltner A, and Baer E. Journal of Applied Polymer Science 2006;100(2):1651-1658.

16. Hosier IL, Alamo RG, Esteso P, Isasi JR, and Mandelkern L. Macromolecules 2003;36(15):5623-5636.

17. Hosoda S, Hori H, Yada K-i, Nakahara S-y, and Tsuji M. Polymer 2002;43(26):7451-7460.

18. Hosier IL, Alamo RG, and Lin JS. Polymer 2004;45(10):3441-3455.

19. De Rosa C, Dello Iacono S, Auriemma F, Ciaccia E, and Resconi L. Macromolecules 2006;39(18):6098-6109.

20. De Rosa C, Auriemma F, de Ballesteros OR, Resconi L, and Camurati I. Macromolecules 2007;40(18):6600-6616.

21. De Rosa C, Auriemma F, Vollaro P, Resconi L, Guidotti S, and Camurati I. Macromolecules 2011;44(3):540-549.

22. Bartczak Z, Chiono V, and Pracella M. Polymer 2004;45(22):7549-7561.

23. An Y, Xing H, Wang Y, and Tang T. Journal of Applied Polymer Science 2012;125(4):2724-2731.

24. Semenov AN. Physical Review E 2006;73(4):041803.

25. Fraser RDB, Macrae TP, Miller A, and Rowlands RJ. Journal of Applied Crystallography 1976;9(2):81-94.

26. Burger C, Hsiao BS, and Chu B. Polymer Reviews 2010;50(1):91-111.

27. Mao Y, Burger C, Zuo F, Hsiao BS, Mehta A, Mitchell C, and Tsou AH. Macromolecules 2011;44(3):558-565.

28. Mao Y, Burger C, Li X, Hsiao BS, Mehta AK, and Tsou AH. Macromolecules 2012;45(2):951-961.

29. Burger C, Zhou H-w, Sicundefined I, Hsiao BS, Chu B, Graham L, and Glimcher MJ. Journal of Applied Crystallography 2008;41(2):252-261.

30. Mao Y, Li X, Burger C, Hsiao BS, Mehta AK, and Tsou AH. Macromolecules 2012;45(17):7061-7071.

31. Ruland W. Colloid & Polymer Science 1977;255(9):833-836.

32. Ruland W and Tompa H. Acta Crystallographica Section a-Crystal Physics Diffraction Theoretical and General Crystallography 1968:A 24, 93-99.

33. Turner-Jones A. Polymer 1971;12(8):487-508.

34. Meille SV, Bruckner S, and Porzio W. Macromolecules 1990;23(18):4114-4121.

35. Nedorezova P, Chapurina A, Koval'chuk A, Klyamkina A, Aladyshev A, Optov V, and Shklyaruk B. Polymer Science Series B 2010;52(1):15-25.

36. Lotz B and Wittmann JC. Journal of Polymer Science Part B: Polymer Physics 1986;24(7):1541-1558.

37. Lotz B, Wittmann JC, and Lovinger AJ. Polymer 1996;37(22):4979-4992.

38. Hermans JJ. Rec. Trav. Chim. Pays-Bas. 1944(63):211-218.

39. Ruland W and Smarsly B. Journal of Applied Crystallography 2004;37(4):575-584.

40. Androsch R, Stribeck N, Lüpke T, and Funari SS. Journal of Polymer Science Part B: Polymer Physics 2002;40(17):1919-1930.

41. Stribeck N, Androsch R, and Funari SS. Macromolecular Chemistry and Physics 2003;204(9):1202-1216.

42. Peterlin A. Journal of Materials Science 1971;6(6):490-508.

43. Hiss R, Hobeika S, Lynn C, and Strobl G. Macromolecules 1999;32(13):4390-4403.

44. Chen HY, Chum SP, Hiltner A, and Baer E. Journal of Polymer Science Part B: Polymer Physics 2001;39(14):1578-1593.

45. Minick J, Moet A, Hiltner A, Baer E, and Chum SP. Journal of Applied Polymer Science 1995;58(8):1371-1384.

46. Bensason S, Stepanov EV, Chum S, Hiltner A, and Baer E. Macromolecules 1997;30(8):2436-2444.

47. Vanden Eynde S, Mathot V, Koch MHJ, and Reynaers H. Polymer 2000;41(9):3437-3453.

Chapter 6. Conclusions

Polyolefin is one kind of important polymer products in industry. During manufacturing, the processing condition would greatly influence the crystal structure and the final properties. In this dissertation, different kinds of polyolefin based polymers, including single component materials and composite materials, were used to study the crystallization, morphology, structure, performance and the relationship among them during different processing conditions.

In Chapter 1, isothermal crystallization behaviors of high density polyethylene/silica (HDPE-SiO$_2$) nanocomposites with different SiO$_2$ loading of 2 % and 5 %, along with the neat HDPE sample were studied by using the time-resolved wide angle X-ray diffraction (WAXD) and small angle X-ray scattering (SAXS) techniques. For isothermal crystallization at 120 ℃, WAXD patterns showed that HDPE-Si2% had the highest ending crystallinity, while HDPE-Si5% had the lowest value. Avrami exponent of pure HDPE was about 3.7, while HDPE-Si2% had a value of 3.1 which indicated a typically heterogeneous nucleation behavior with the addition of silica in HDPE. SAXS patterns showed that the silica structure inside HDPE did not change significantly during the isothermal crystallization process. The structure of HDPE-SiO$_2$ during crystallization was sketched based on the obtained results.

In Chapter 2, these silica-HDPE nanocomposites along with the neat HPDE samples were

further characterized under the uniaxial stretching experiment as to investigate the influence of silica filler on the tensile performance. Silica filled HDPE samples showed better yielding strength. From SAXS patterns, the silica network structure in nanocomposite would show strong scattering intensity in low scattering angle region and the structure remained during stretching. Oscillatory shear measurement confirmed the interaction among the silica particles in the silica network and polymer matrix.

In Chapter 3, a specially designed cross-slot flow cell was used to generate extension-dominant flow. *In-situ* SAXS measurements were performed to investigate the extensional flow-induced crystallization of isotactic polypropylene (*i*PP) melt with weight averaged molecular weight (M_w) of 330,000 g/mol. Different strain rates (from 4.6 s^{-1} to 34.7 s^{-1}) and strains (from 116 to 580) were applied. It was found that the formed precursor structures, shish and kebab, were closely depended on the character of extension flow applied. There existed a critical strain rate on the formation of flow-induced precursor structures. Mechanism of the shish and kebab formation was discussed.

In Chapter 4, an ionic liquid (IL) 1-docosanyl-3-methylimidazolium bromide was incorporated into ultra-high molecular weight polyethylene (UHMWPE) and formed the IL/UHWMPE blend by solution mixing. The structural evolution of this blend during uniaxial stretching was followed by *in-situ* WAXD and SAXS techniques. During deformation at room temperature, the elongation-to-break ratio of the IL/UHMWPE blend increased by 2 - 3 times compared with pure UHMWPE, where the blend did not lose the tensile strength. Deformation-induced phase transformation from orthorhombic to monoclinic phase was

observed in both blend and neat UHMWPE. During deformation at high temperature (120 ℃), no phase transformation was observed in both samples. However, the blend showed better toughness, higher crystal orientation, and tilted lamellar structure at high strains.

In Chapter 5, the crystal structure evolutions of a serial of propylene-1-octene random copolymers with different octene comonomer concentrations during uniaxial stretching at 60 ℃ were characterized by *in-situ* WAXD and SAXS techniques. With higher octene content, copolymer had decreased elastic modulus and yield stress in stress-strain curve and behaved more like elastomer. Besides, less crystallinity and less orientation were found in high octene sample under deformation. Step-cycle tensile test showed that copolymer with higher octene content had higher recovery ratio. From the 2D SAXS pattern simulation, it was found that in low octene content sample, intra-lamella slip happened and lateral lamella crystal size decreased fast. Stress might concentrate on the lamella crystal during stretching. For high octene content sample, stress might concentrate on the amorphous matrix leading inter-lamella slip, and lateral lamella size only slightly decreased. The schematic structure change of propylene-1-octene copolymer under deformation was presumed to explain the different elasticity behavior in these copolymer samples.

Bibliography

1.1. Balazs AC, Emrick T, and Russell TP. Science 2006;314(5802):1107-1110.

1.2. Schaefer DW and Justice RS. Macromolecules 2007;40(24):8501-8517.

1.3. Vaia RA, Jandt KD, Kramer EJ, and Giannelis EP. Macromolecules 1995;28(24):8080-8085.

1.4. Vaia RA and Giannelis EP. MRS Bull. 2001(26):394-401.

1.5. Schadler LS. Nanocomposite Science and Technology; Wiley-VCH: Weinheim, Germany, 2003.

1.6. Thongruang W, Balik CM, and Spontak RJ. Journal of Polymer Science Part B: Polymer Physics 2002;40(10):1013-1025.

1.7. Liu ZH, Kwok KW, Li RKY, and Choy CL. Polymer 2002;43(8):2501-2506.

1.8. Wang KH, Chung IJ, Jang MC, Keum JK, and Song HH. Macromolecules 2002;35(14):5529-5535.

1.9. Zhang MQ, Rong MZ, Zhang HB, and Friedrich K. Polymer Engineering & Science 2003;43(2):490-500.

1.10. Makarov C, Khalfin RL, Makarov V, Cohen Y, Sertchook H, Elimelech H, and Avnir D. Polymers for Advanced Technologies 2007;18(9):712-719.

1.11. Zou H, Wu S, and Shen J. Chemical Reviews 2008;108(9):3893-3957.

1.12. Schaefer DW and Keefer KD. Physical Review Letters 1986;56(20):2199-2202.

1.13. Vacher R, Woignier T, Pelous J, and Courtens E. Physical Review B 1988;37(11):6500-6503.

1.14. Schaefer DW, Rieker T, Agamalian M, Lin JS, Fischer D, Sukumaran S, Chen C, Beaucage G, Herd C, and Ivie J. Journal of Applied Crystallography 2000;33(3 Part 1):587-591.

1.15. Donatti DA, Vollet DR, Ibanez Ruiz A, Mesquita A, and Silva TFP. Physical Review B 2005;71(1):014203.

1.16. Mélé P, Marceau S, Brown D, de Puydt Y, and Albérola ND. Polymer 2002;43(20):5577-5586.

1.17. Meier JG, Mani JW, and Klüppel M. Physical Review B 2007;75(5):054202.

1.18. Schneider GJ, Vollnhals V, Brandt K, Roth SV, and Goritz D. Journal of Chemical Physics 2010;133(9).

1.19. Matějka L, Pleštil J, and Dušek K. Journal of Non-Crystalline Solids 1998;226(1–2):114-121.

1.20. Jiasheng Q and Pingsheng H. Journal of Materials Science 2003;38(11):2299-2304.

1.21. Jain S, Goossens H, van Duin M, and Lemstra P. Polymer 2005;46(20):8805-8818.

1.22. Fraser RDB, Macrae TP, Miller A, and Rowlands RJ. Journal of Applied Crystallography 1976(9):81-94.

1.23. Wang ZG, Hsiao BS, Sirota EB, Agarwal P, and Srinivas S. Macromolecules 2000;33(3):978-989.

1.24. Avrami M. J. Chem. Phys. 1939(7):1103.

1.25. Mandelkern L. Crystallization of polymers McGraw-Hill, New York, 1963.

1.26. Gedde UW. Polymer Physics, Chapman & Hall, New York, 1995

1.27. Velisaris CN and Seferis JC. Polymer Engineering & Science 1986;26(22):1574-1581.

1.28. Hwang JC, Chen C-C, Chen H-L, and Yang W-CO. Polymer 1997;38(16):4097-4101.

1.29. Mandelkern L. Crystallization of Polymers: Kinetics and mechanisms, Cambridge University Press, 2004.

1.30. Gordon M and Hillier IH. Phil. Mag. 1965;11(109):31-41.

1.31. Wenig W. Journal of Materials Science 1994;29(18):4708-4712.

1.32. Jouault N, Vallat P, Dalmas F, Said Sr, Jestin J, and Boué Fo. Macromolecules 2009;42(6):2031-2040.

1.33. Glatter O and Kratky O. Small Angle X-Ray Scattering; Academic Press: New York, 1982.

2.1. Crosby AJ and Lee JY. Polymer Reviews 2007;47(2):217-229.

2.2. Balazs AC, Emrick T, and Russell TP. Science 2006;314(5802):1107-1110.

2.3. Cassagnau P. Polymer 2008;49(9):2183-2196.

2.4. Liu ZH, Kwok KW, Li RKY, and Choy CL. Polymer 2002;43(8):2501-2506.

2.5. Hussain F, Hojjati M, Okamoto M, and Gorga RE. Journal of Composite Materials 2006;40(17):1511-1575.

2.6. Osman MA and Atallah A. Polymer 2006;47(7):2357-2368.

2.7. Kontou E and Niaounakis M. Polymer 2006;47(4):1267-1280.

2.8. Zou H, Wu S, and Shen J. Chemical Reviews 2008;108(9):3893-3957.

2.9. Zhang MQ, Rong MZ, Zhang HB, and Friedrich K. Polymer Engineering & Science 2003;43(2):490-500.

2.10. Dorigato A and Pegoretti A. Engineering Fracture Mechanics 2012;79(0):213-224.

2.11. Lai S-M, Chen J-R, Han J-L, Yu Y-F, and Lai H-Y. Journal of Applied Polymer Science 2013;130(1):496-503.

2.12. Makarov C, Khalfin RL, Makarov V, Cohen Y, Sertchook H, Elimelech H, and Avnir D. Polymers for Advanced Technologies 2007;18(9):712-719.

2.13. Grubb DT and Prasad K. Macromolecules 1992;25(18):4575-4582.

2.14. Butler MF, Donald AM, Bras W, Mant GR, Derbyshire GE, and Ryan AJ. Macromolecules 1995;28(19):6383-6393.

2.15. Russell KE, Hunter BK, and Heyding RD. Polymer 1997;38(6):1409-1414.

2.16. Sepehr M, Utracki LA, Zheng X, and Wilkie CA. Polymer 2005;46(25):11569-11581.

2.17. Sinha Ray S and Okamoto M. Macromolecular Materials and Engineering 2003;288(12):936-944.

2.18. Sinha Ray S and Okamoto M. Progress in Polymer Science 2003;28(11):1539-1641.

2.19. Galgali G, Ramesh C, and Lele A. Macromolecules 2001;34(4):852-858.

2.20. Hoffmann B, Dietrich C, Thomann R, Friedrich C, and Mülhaupt R. Macromolecular Rapid Communications 2000;21(1):57-61.

2.21. Dorigato A, Pegoretti A, and Penati A. eXPRESS Polymer Letters 2009;4(2):115-129.

2.22. Suprakas SR. J. Ind. Eng. Chem. 2006;12:811-842.

3.1. Flory PJ. Journal of Chemical Physics 1947;15(6):397-408.

3.2. Ziabicki A. Fundamentals of Fiber Formation: The Science of Fibre Spinning and Drawing, Wiley: New York 1976.

3.3. Keller A and Kolnaar HWH. Mat. Sci. Tech. 1997;18:189.

3.4. Eder G and Janeschitz-Kriegl H. Mat. Sci. Tech. 1997;18:268.

3.5. Kumaraswamy G. J. Macromol. Sci. Polym. Rev. 2005;45:375.

3.6. Mitsuhashi S. Bull. Text. Res. Inst. 1963;66:1.

3.7. Pennings AJ and Kiel AM. Kolloid Z. Z. Polym 1965;205:160.

3.8. Binsbergen FL. Nature 1966;211:516.

3.9. Keller A and Machin MJ. J. Macromol. Sci. Phys. 1967;B1:41.

3.10. Hill MJ and Keller A. J. Macromol. Sci. Phys. 1969;B3:153.

3.11. de Gennes PG. J. Chem. Phys. 1974;60:5030.

3.12. Pope DP and Keller A. Colloid & Polymer Science 1978;256(8):751-756.

3.13. Miles MJ and Keller A. Polymer 1980;21(11):1295-1298.

3.14. Keller A and Odell JA. Colloid & Polymer Science 1985;263(3):181-201.

3.15. Keller A and Kolnaar JWH. Progress in Colloid & Polymer Science 1993;92:81-102.

3.16. Dukovski I and Muthukumar M. J. Chem. Phys. 2003;118:6648.

3.17. Seki M, Thurman DW, Oberhauser JP, and Kornfield JA. Macromolecules 2002;35(7):2583-2594.

3.18. Janeschitz-Kriegl H, Ratajski E, and Stadlbauer M. Rheologica Acta 2003;42(4):355-364.

3.19. Elmoumni A, Winter HH, Waddon AJ, and Fruitwala H. Macromolecules 2003;36(17):6453-6461.

3.20. Schrauwen BAG, Breemen LCAv, Spoelstra AB, Govaert LE, Peters GWM, and Meijer HEH. Macromolecules 2004;37(23):8618-8633.

3.21. Wang M, Hu W, Ma Y, and Ma Y-q. Macromolecules 2005;38(7):2806-2812.

3.22. Smith DE and Chu S. Science 1998;281:1335.

3.23. Smith DE, Babcock HP, and Chu S. Science 1999;283:1724.

3.24. van Meerveld J, Peters GWM, and Hütter M. Rheologica Acta 2004;44(2):119-134.

3.25. Yan T, Zhao B, Cong Y, Fang Y, Cheng S, Li L, Pan G, Wang Z, Li X, and Bian F. Macromolecules 2010;43(2):602-605.

3.26. Tian N, Zhou W, Cui K, Liu Y, Fang Y, Wang X, Liu L, and Li L. Macromolecules 2011;44(19):7704-7712.

3.27. Sentmanat ML. Rheologica Acta 2004;43(6):657-669.

3.28. Meissner J and Hostettler J. Rheologica Acta 1994;33(1):1-21.

3.29. Kwon YK, Ko YS, and Okamoto M. Polymer 2008;49(9):2334-2341.

3.30. Perkins TT, Smith DE, and Chu S. Science 1997;276:2016-2021.

3.31. Odell JA and Carrington SP. Journal of Non-Newtonian Fluid Mechanics 2006;137(1–3):110-120.

3.32. Keum JK. Ph. D. Thesis. 2007, Stony Brook University.

3.33. Somani RH, Yang L, Hsiao BS, Agarwal PK, Fruitwala HA, and Tsou AH. Macromolecules 2002;35(24):9096-9104.

3.34. Somani RH, Yang L, Zhu L, and Hsiao BS. Polymer 2005;46(20):8587-8623.

3.35. Perret R and Ruland W. Journal of Applied Crystallography 1969;2(5):209-218.

3.36. Perret R and Ruland W. Journal of Applied Crystallography 1970;3(6):525-532.

3.37. Keum JK, Somani RH, Zuo F, Burger C, Sics I, Hsiao BS, Chen H, Kolb R, and Lue C-T. Macromolecules 2005;38(12):5128-5136.

3.38. Wen H, Jiang S, Men Y, Zhang X, An L, Wu Z, and Okuda H. J. Chem. Phys. 2009;130:164909.

3.39. Keum JK, Burger C, Hsiao BS, Somani R, Yang L, Chu B, Kolb R, Chen HY, and Lue CT. Progr. Colloid. Polym. Sci. 2005;130:114.

3.40. Somani RH, Yang L, Hsiao BS, Sun T, Pogodina NV, and Lustiger A. Macromolecules 2005;38(4):1244-1255.

4.1. Welton T. Chem. Rev. 1999;99:2071-83.

4.2. Kubisa PJ. Polym. Sci., Part A 2005;43:4675-83.

4.3. Winterton NJ. Mater. Chem. 2006;16:4281-93.

4.4. Ueki T, Watanabe M. Macromolecules 2008;41:3739-49.

4.5. Wasserscheid P, Keim W. Angew. Chem., Int. Ed. 2000;39:3772-89.

4.6. Wilkes JS. Green Chem. 2002;4:73-80.

4.7. Harrisson S, Mackenzie SR, Haddleton DM. Macromolecules 2003;36:5072-5.

4.8. Strehmel V, Laschewsky A, Wetzel H, Görnitz E. Macromolecules 2006;39:923-30.

4.9. Biedroń T, Kubisa P. J Polym Sci Part A: Polym Chem 2004;42:3230-5.

4.10. Vygodskii YS, Lozinskaya EI, Shaplov AS, Lyssenko KA, Antipin MY, Urman YG. Polymer 2004;45:5031-45.

4.11. Kaar JL, Jesionowski AM, Berberich JA, Moulton V, Russell AJ. J. Am. Chem. Soc. 2003; 125:4125-31.

4.12. Carmichael AJ, Haddleton DM, Bona SAF, Seddon KR. Chem. Commun. 2000;1237-8.

4.13. Fujita K, MacFarlane DR, Forsyth M. Chem. Commun. 2005;4804-6.

4.14. Phillips DM, Drummy LF, Naik RR, De Long HC, Fox DM, Trulove PC, Mantz RAJ. Mater Chem. 2005;4206-14.

4.15. Xie HB, Li SH, Zhang SB. Green Chem. 2005;7:606-8.

4.16. Forsyth SA, MacFarlane DR, Thomson RJ, VonItzstein M. Chem. Commun., 2002;714-5.

4.17. Scott MP, Brazel CS, Benton MG, Mays JW, Holbrey JD, Rogers RD. Chem. Commun. 2002;1370-1.

4.18. Scott MP, Rahman M, Brazel CS. Eur. Polym. J. 2003;39:1947-53.

4.19. Lewandowski A, Swiderska A. Solid State Ionics, 2003;161:243-9.

4.20. Rahman M, Shoff HW, Brazel CS. ACS Symp. Ser., 2005;913:913.

4.21. Chu B, Hsiao BS, Ma HY, Taniguchi N. PCT patent. WO/2009/108236

4.22. Wunderlich B, Cormier CM. J. Polym. Sci., Polym. PartA-2 1967;5:987-91.

4.23. Fraser RDB, Macrae TP, Miller A, Rowlands RJ. J Appl Crystallogr 1976;9:81-94.

4.24. Ran S, Zong X, Fang D, Hsiao BS, Chu B, Ross R. J Appl Crystallogr 2000;33:1031-6.

4.25. Tanaka K, Seto T, Hara T. J. Phys. Soc. Japan 1962;17:873-4.

4.26. Seto T, Hara T, Tanaka K. Japan J. Appl. Phys. 1968;7:31

4.27. Butler MF, Donald AM, Bras W, Mant GR, Derbyshire GE, Ryan AJ. Macromolecules 1995;28:6383-93.

4.28. Russell KE, Hunter BK, Heyding RD. Polymer 1997;38:1409-14.

4.29. Grubb DT, Prasad K. Macromolelues. 1992;25:4575-82.

4.30. Butler MF, Donald AM, Ryan AJ. Polymer 1998;39:39-52.

4.31. Ruland, W. J. Polym. Sci., Part C 1969;28:143-51.

4.32. Perret R, Ruland W. J. Appl. Cryst. 1969;2:209-18.

4.33. Jang J, Lee DK. Polymer 2003;44:8139-46,

4.34. Wypych G. Handbook of Plasticizers. ChemTec Publishing, 2004.

4.35. Aggarwal SL, Tilley GP, Sweeting OJJ. Polym. Sci.1961;51:551-68.

4.36. Chen XM, Yoon KW, Burger C, Sics I, Fang DF, Hsiao BS, Chu B. Macromolecules 2005;38:3883-93.

4.37. Wilchinsky ZW. J Appl Phys 1960;31:1969-72.

4.38. Kaji K, Mochizuki T, Akiyama A, Hosemann R, J. Matls. Sci. 1978;13:972-84.

4.39. Song HH, Argon AS, Cohen RE Macromolecules 1990;23:870-6.

5.1. Mighri F, Huneault MA, Ajji A, Ko GH, and Watanabe F. Journal of Applied Polymer Science 2001;82(9):2113-2127.

5.2. Yang D, Zhang B, Yang Y, Fang Z, Sun G, and Feng Z. Polymer Engineering & Science 1984;24(8):612-617.

5.3. Liang JZ and Li RKY. Journal of Applied Polymer Science 2000;77(2):409-417.

5.4. Öksüz M and Eroğlu M. Journal of Applied Polymer Science 2005;98(3):1445-1450.

5.5. Choudhary V, Varma HS, and Varma IK. Polymer 1991;32(14):2534-2540.

5.6. van der Wal A, Mulder JJ, Oderkerk J, and Gaymans RJ. Polymer 1998;39(26):6781-6787.

5.7. Lee H-y, Kim DH, and Son Y. Journal of Applied Polymer Science 2007;103(2):1133-1139.

5.8. Da Silva ALN, Rocha MCG, Coutinho FMB, Bretas R, and Scuracchio C. Journal of Applied Polymer Science 2000;75(5):692-704.

5.9. Fredrickson GH, Milner ST, and Leibler L. Macromolecules 1992;25(23):6341-6354.

5.10. Tang W, Tang J, Yuan H, and Jin R. Journal of Applied Polymer Science 2011;122(1):461-468.

5.11. Brintzinger HH, Fischer D, Mülhaupt R, Rieger B, and Waymouth RM. Angewandte Chemie International Edition in English 1995;34(11):1143-1170.

5.12. Busico V and Cipullo R. Progress in Polymer Science 2001;26(3):443-533.

5.13. Poon B, Rogunova M, Chum SP, Hiltner A, and Baer E. Journal of Polymer Science Part B: Polymer Physics 2004;42(23):4357-4370.

5.14. Poon B, Rogunova M, Hiltner A, Baer E, Chum SP, Galeski A, and Piorkowska E. Macromolecules 2005;38(4):1232-1243.

5.15. Stephens CH, Poon BC, Ansems P, Chum SP, Hiltner A, and Baer E. Journal of Applied Polymer Science 2006;100(2):1651-1658.

5.16. Hosier IL, Alamo RG, Esteso P, Isasi JR, and Mandelkern L. Macromolecules 2003;36(15):5623-5636.

5.17. Hosoda S, Hori H, Yada K-i, Nakahara S-y, and Tsuji M. Polymer 2002;43(26):7451-7460.

5.18. Hosier IL, Alamo RG, and Lin JS. Polymer 2004;45(10):3441-3455.

5.19. De Rosa C, Dello Iacono S, Auriemma F, Ciaccia E, and Resconi L. Macromolecules 2006;39(18):6098-6109.

5.20. De Rosa C, Auriemma F, de Ballesteros OR, Resconi L, and Camurati I. Macromolecules 2007;40(18):6600-6616.

5.21. De Rosa C, Auriemma F, Vollaro P, Resconi L, Guidotti S, and Camurati I. Macromolecules 2011;44(3):540-549.

5.22. Bartczak Z, Chiono V, and Pracella M. Polymer 2004;45(22):7549-7561.

5.23. An Y, Xing H, Wang Y, and Tang T. Journal of Applied Polymer Science 2012;125(4):2724-2731.

5.24. Semenov AN. Physical Review E 2006;73(4):041803.

5.25. Fraser RDB, Macrae TP, Miller A, and Rowlands RJ. Journal of Applied Crystallography 1976;9(2):81-94.

5.26. Burger C, Hsiao BS, and Chu B. Polymer Reviews 2010;50(1):91-111.

5.27. Mao Y, Burger C, Zuo F, Hsiao BS, Mehta A, Mitchell C, and Tsou AH. Macromolecules 2011;44(3):558-565.

5.28. Mao Y, Burger C, Li X, Hsiao BS, Mehta AK, and Tsou AH. Macromolecules 2012;45(2):951-961.

5.29. Burger C, Zhou H-w, Sicundefined I, Hsiao BS, Chu B, Graham L, and Glimcher MJ. Journal of Applied Crystallography 2008;41(2):252-261.

5.30. Mao Y, Li X, Burger C, Hsiao BS, Mehta AK, and Tsou AH. Macromolecules 2012;45(17):7061-7071.

5.31. Ruland W. Colloid & Polymer Science 1977;255(9):833-836.

5.32. Ruland W and Tompa H. Acta Crystallographica Section a-Crystal Physics Diffraction Theoretical and General Crystallography 1968:A 24, 93-99.

5.33. Turner-Jones A. Polymer 1971;12(8):487-508.

5.34. Meille SV, Bruckner S, and Porzio W. Macromolecules 1990;23(18):4114-4121.

5.35. Nedorezova P, Chapurina A, Koval'chuk A, Klyamkina A, Aladyshev A, Optov V, and Shklyaruk B. Polymer Science Series B 2010;52(1):15-25.

5.36. Lotz B and Wittmann JC. Journal of Polymer Science Part B: Polymer Physics 1986;24(7):1541-1558.

5.37. Lotz B, Wittmann JC, and Lovinger AJ. Polymer 1996;37(22):4979-4992.

5.38. Hermans JJ. Rec. Trav. Chim. Pays-Bas. 1944(63):211-218.

5.39. Ruland W and Smarsly B. Journal of Applied Crystallography 2004;37(4):575-584.

5.40. Androsch R, Stribeck N, Lüpke T, and Funari SS. Journal of Polymer Science Part B: Polymer Physics 2002;40(17):1919-1930.

5.41. Stribeck N, Androsch R, and Funari SS. Macromolecular Chemistry and Physics 2003;204(9):1202-1216.

5.42. Peterlin A. Journal of Materials Science 1971;6(6):490-508.

5.43. Hiss R, Hobeika S, Lynn C, and Strobl G. Macromolecules 1999;32(13):4390-4403.

5.44. Chen HY, Chum SP, Hiltner A, and Baer E. Journal of Polymer Science Part B: Polymer Physics 2001;39(14):1578-1593.

5.45. Minick J, Moet A, Hiltner A, Baer E, and Chum SP. Journal of Applied Polymer Science 1995;58(8):1371-1384.

5.46. Bensason S, Stepanov EV, Chum S, Hiltner A, and Baer E. Macromolecules 1997;30(8):2436-2444.

5.47. Vanden Eynde S, Mathot V, Koch MHJ, and Reynaers H. Polymer 2000;41(9):3437-3453.